Crystal Plasticity Constitutive Modeling of Grain Size-Texture Coupling with Application to Mg-4Al

by

Aaditya Lakshmanan

A dissertation submitted in partial fulfillment
of the requirements for the degree of
Doctor of Philosophy
(Aerospace Engineering)
in the University of Michigan
2022

Doctoral Committee:

Professor Veera Sundararaghavan, Chair
Professor John E. Allison
Professor Daniel J. Inman
Professor Amit Misra

"The important thing in science is not so much to obtain new facts as to discover new ways of thinking about them." – William Lawrence Bragg

Aaditya Lakshmanan

aadityal@umich.edu

ORCID iD: 0000-0002-0484-5196

ACKNOWLEDGEMENTS

I would first like to express my sincere gratitude to Prof. Veera Sundararaghavan for giving me the opportunity and the freedom to pursue research in the area of crystal plasticity. He has been a source of inspiration to me and his constant guidance and positive attitude have been instrumental in shaping my research and thought process. I would like to thank Professors Daniel Inman, John Allison and Amit Misra for serving on my committee and taking the time to review my work. I have learnt a great deal working with a large code base and assisting in the training workshops as a member of the Center for PRedictive Integrated Structural Materials Science (PRISMS), under the leadership of Prof. Allison. I am thankful to Prof. Misra and his student, Dr. Mohsen Andani for sharing the experimental data and insights that form the backbone of this thesis. I would like to thank Dr. Mohammadreza Yaghoobi for his guidance in understanding and utilizing multiple features of the PRISMS-Plasticity code. Special thanks to Professors Anand Kanjarla, Phanikumar Gandham, Shyam Keralavarma and Sundararaman Mahadevan for sparking my interest in diverse topics of mechanics and materials science.

I have been very fortunate to pursue my passion for mathematics through courses taught by some amazing teachers. I would like to thank Prof. Jenny Wilson for her course on topology, Prof. Zaher Hani for his course on dynamical systems, Prof. Sijue Wu for her course on partial differential equations, and to the late Prof. Charles Doering for his course on mathematical fluid dynamics. My love for mechanics has only grown with time, thanks to Prof. John Shaw for his courses on solid mechanics and elastic stability, and Prof. James Barber for his course on elasticity.

The company of my friends has been a constant source of happiness for me throughout

my studies. I would like to thank Siddhartha for numerous interesting discussions involving mathematics, mechanics, stand-up comedy and anime that accompanied explorations of food and coffee around the campus. Thanks to Kunal for being an amazing friend and roommate, feeding me delicious Indian food, helping me with my taxes and for all those billiards games at Pierpont. I would like to thank Aniruddhe for being the gem of a person that he is, and for sharing his passion for cooking, numerical methods and turbulence, which have greatly enriched my outlook on many fronts. Thanks to Aditya, my friend and brother from another mother, for tolerating me as a roommate, for his cutting-edge humor, and for sharing my enthusiasm for badminton and table tennis. I would like to thank Gurmeet for introducing me to exercise routines, accompanying me to Yoon's bakery to savor the cream bread and for his preparations of delicious methi malai matar while appreciating Bill Burr's comedy. Thanks to Srihari for his insights on programming and high performance computing, his camaraderie, and for being the undesignated driver to many trips. I would like to thank Subramaniam for his company through math courses and sharing his passion for quizzing, interesting stories and light-hearted gossips.

Thanks to Agnit for all those long drives in his Mazda while timeless ghazals played in the background, to Akarsh for sharing my love for desserts and the dominos garlic parmesan pizza, to Srinivasan for all the delicious South Indian food he prepared amidst his singing, and to Vishwas for organizing great house parties and gatherings during the festive season. Thanks to Vishnu and Harsh for all the cricket sessions in the Willowtree tennis and basketball courts which disrupted the monotony during the lockdown. Many thanks to Manish, Karan and Anand, my first roommates in Ann Arbor, for setting a positive tone to my stay in the US through late night weekends involving drinks and punjabi songs. I would like to thank all past/present MSSL lab members for their help and advice when I most needed it : Arunabha, Sriram, Shardul, Adam, Pınar, Jiangyi, Iman and Siddharth. I would like to thank my office mates - Doreen, Gustavo, Avin, Hoang and Paul - for always maintaining a lively presence around the office. I would like to thank the following people whose company I have cherished over the years and who have made my journey a truly memorable one : Akshay, Ananthakrishnan, Asmita, Corey, Deepak, Devina, Divya, Doğa, Guodong,

Krystal, Mohit, Puneet, Rohit, Sagardeep, Shiyao, Sneha, Sravan, Srinivas Karthik, Vishal, Yifan and Yukiko. Thanks to Chal and the Novelis modeling team for the great experience and new learnings during my internship. My special thanks to graduate coordinators, Denise Phelps and Ruthie Freeman for their immense help throughout my graduate studies.

Finally, I would like to thank my parents, Vijayalakshmi and Lakshmanan, and my sister, Priyanka, for their unconditional love and support throughout my stay away from home. Words simply cannot describe my love for them. I would like to thank my Mama and Mami, Mani and Mayuri, for always taking care of me like their own child. Thanks to my sweet cousins, Shivani and Shriya, who constantly reminded me of the joys of being a kid. Many thanks to my cousin, Advik, for always keeping in touch with me through long drawn conversations about food and interesting stories about Lviv. I would like to thank my extended family who have continually been a positive influence during this time.

I acknowledge the U.S. Department of Energy, Office of Basic Energy Sciences, Division of Materials Sciences and Engineering under Award #DE-SC0008637, as part of the Center for PRedictive Integrated Structural Materials Science (PRISMS Center), for financial support.

TABLE OF CONTENTS

LIST OF FIGURES

Figure

LIST OF TABLES

Table

LIST OF APPENDICES

Appendix

ABSTRACT

Grain refinement is a common strategy to improve the yield strength of magnesium (Mg) alloys quantified via the empirical Hall-Petch equation. Due to the hexagonal close-packed (HCP) crystal structure of Mg alloys, the Hall-Petch effect, which characterizes the sensitivity of the yield stress to the grain size, has been observed to be strongly dependent on the underlying crystallographic texture, arising through the effect of grain boundaries (GBs) as evidenced by several experimental studies. Crystal plasticity (CP) simulations form a powerful modeling tool to model and simulate the elastoplastic mechanical behavior of crystalline materials. Classical CP models do not include the effect of grain size in the constitutive model and hence are unable to simulate the Hall-Petch effect. There are also very few studies targeted towards developing constitutive models which account for the effect of grain size on the yield stress of the material. More so, those few studies do not account for the underlying microstructural aspects due to which the coupling between texture and grain size is not explicitly considered.

This thesis presents efforts towards developing such a constitutive model accounting for this grain size-texture coupling by integrating high-resolution electron backscatter diffraction experiments with dislocation pile-up theory and CP simulations. A rate-

dependent CP constitutive model was first developed within the PRISMS-Plasticity framework, an open-source parallelized finite element code to simulate the elasto-viscoplastic behavior of materials. In the context of the Hall-Petch effect, a continuum dislocation pile-up model was used to fit pile-up stress measurements ahead of basal slip bands blocked by GBs in Mg-4Al, which along with some simplifying assumptions, yields the micro-Hall-Petch parameters for basal slip for nine GBs. The basal micro-Hall-Petch parameters varied from 54 MPa $\mu m^{1/2}$ to 184 MPa $\mu m^{1/2}$, which were then related to GB metrics using an empirical power-law equation to obtain the basal micro-Hall-Petch coefficients - the micro-Hall-Petch multiplier and exponent. The GB metrics were constructed from incoming and potential outgoing slip system information obtained from CP simulations of GB neighborhoods of the GBs considered. Extending a similar procedure to prismatic slip, the prismatic micro-Hall-Petch parameters varied from 138 MPa $\mu m^{1/2}$ to 685 MPa $\mu m^{1/2}$, which were again related to GB metrics to obtain the prismatic micro-Hall-Petch coefficients - the micro-Hall-Petch multiplier and exponent. The potential outgoing slip system information required to construct the GB metrics was obtained from CP simulations of GB neighborhoods. The experimental work does not as yet consider a micro-Hall-Petch equation for the pyramidal slip or extension twinning systems. The micro-Hall-Petch model was implemented into PRISMS-Plasticity and calibrated against experimental stress-strain curves obtained from samples of different textures and grain sizes. The model is used to study the modulation of the grain size effect due to additional parameters including texture, loading direction, and the grain aspect ratio. From the studies involving modulation of texture and loading direction,

we find that the relative competition between basal and prismatic slip activity with texture changes determines the variations in the Hall-Petch slope. From the aspect ratio study, we obtain an asymmetric variation in the yield stress with the aspect ratio, which is justified using theoretical arguments. This approach provides the foundation to quantitatively model and design microstructural features to enhance the engineering properties of Mg alloys.

CHAPTER I

Introduction

Understanding the microscopic mechanisms and physics governing strength, ductility and failure plays a key role in the development of metallic alloys that can be applied in different applications requiring structural integrity as a key requirement. Tailoring microstructures which are damage-tolerant is essential in many fields of engineering, such as vehicles in the automotive industry and aircrafts in the aerospace industry. For a long period of time, these developments were largely empirical. More recently, however, with developments in computational architectures and methodologies, computational methods have become a common approach to either substitute or complement existing empirical models. In this context, the development of more complex materials with novel architectures leading to superior properties has made it more challenging to analyze, understand and predict their behavior with ad-hoc techniques. This is especially challenging for metals where there is a huge drive towards enhanced performance,

With that perspective, Integrated Computational Material Engineering(ICME) [8]

has emerged as a discipline that aims to integrate computational materials science tools into a holistic system that can accelerate materials development, transform the engineering design optimization process, and unify design and manufacturing. The notion of ICME arose from the new simulation-based design paradigm that employs a hierarchical multiscale modeling methodology for optimizing load-bearing structures. The methodology integrates material models with structure-property relationships that are observed from experiments at different length scales. The primary focus of the ICME vision is establishing a knowledge base accessible to the community-at-large for solving a plethora of disparate issues in materials science, applied mechanics, and engineering. This knowledge base requires collection of experimental data describing phenomena at different scales (exploratory experiments, calibration of material models, and validation of models), performing simulations at different scales (atomic, molecular, dislocation, crystal-plasticity, macroscale FEA), and linking all this information together to determine structure-properties relationships, thereby leading to concepts and designs for new materials.

The goal of the PRedictive Integrated Structural Materials Science (PRISMS) center [1] at the University of Michigan, that funded this work, is to establish a unique scientific platform that will enable accelerated predictive materials science for structural metals(Fig. 1.1). The PRISMS-Plasticity code, of which the author has been a co-developer, is a parallel numerical framework for implementing continuum and crystal plasticity models, which form a critical part to the multiscale modeling of metallic materials.

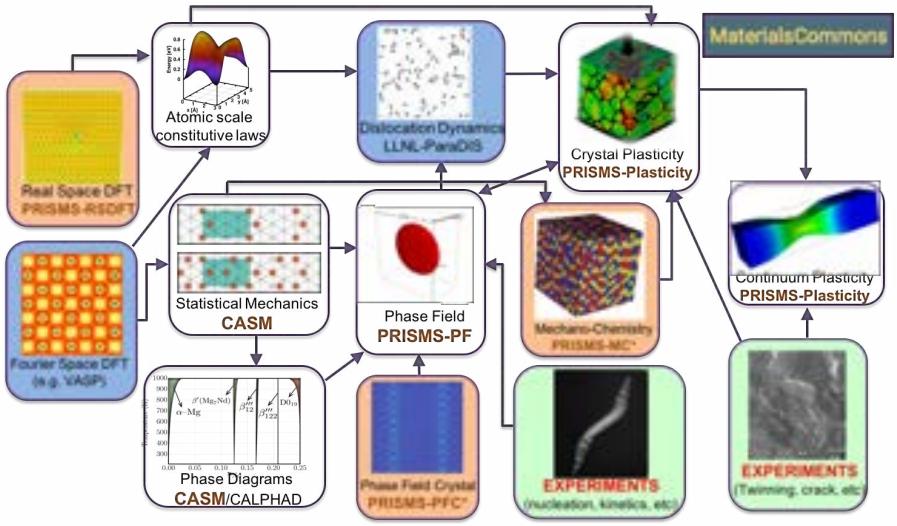

Figure 1.1: Integrated suite of multiscale/multiphysics computational codes developed by the various research groups affiliated with the PRISMS center [1].

1.1. Magnesium alloys

The low density of Mg alloys allows for significant weight reduction in product development, making them strong candidates for applications in the aerospace [9], automotive [10] and medical [11] sectors. Utilization of magnesium alloys in U.S. Military applications is presented in Mathaudu et al. [12] . Magnesium was profoundly used in many aircraft during World War II (1939 - 1945), a key example being the B-36 bomber which had 5555 kg of magnesium sheet, which covered 25% of the exterior, 700 kg of magnesium forgings and 300 kg of magnesium castings. Magnesium casting alloys have been used to an extent in aircraft and helicopter components such as gearbox housings, compressor and filter casings, canopy and brackets [13, 14]. One of the most prominent current applications is that of magnesium transmission and

gear housings in U.S. Army and Navy aircraft such as the Sikorsky Black Hawk [12].

1.2. Hall-Petch effect in Mg alloys

One of the major drawbacks in the widespread use of Mg alloys is their poor formability and ductility at room temperature that arises from the hexagonal close-packed (HCP) crystal structure (c/a = 1.624). Unlike Al alloys with a cubic crystal structure which possess twelve equivalent slip systems to accommodate plastic deformation(Fig. 1.2), Mg alloys depict significant plastic anisotropy where prismatic and pyramidal systems have significantly higher critical resolved shear stress (CRSS) or slip system resistance relative to the three basal slip systems. As a result, during the deformation the grains tend to reorient themselves such that the c-axis aligns perpendicular to the rolling axis [15, 16]. This strongly basal texture limits ductility by preventing easy activation of slip. When a specimen with a strongly basal texture is loaded in uniaxial tension along the rolling direction, the basal slip system is not favorably oriented in grains and therefore the non-basal systems with higher critical resolved shear stress would be activated, thus inhibiting its ductility. Due to this limitation, efforts have focused on tailoring the microstructure to enhance the ductility of Mg alloys. Strategies that attempt to achieve this include, but are not limited to, precipitation hardening [17, 18, 19, 20], solid-solution strengthening [21, 22, 23], texture control [24, 25] and grain refinement [26, 27]. The study of the effect of grain refinement on the yield strength dates back to the classical work by Hall [28] and Petch [29], where a linear relationship was drawn between the lower yield point of mild steel(σ_Y) and the inverse square-root of the average grain size(d), loosely

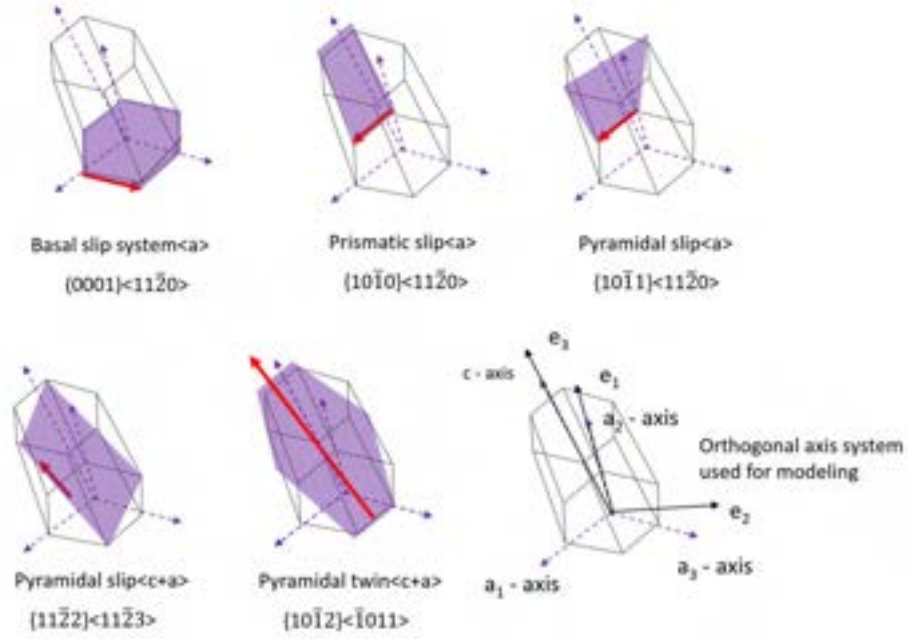

Figure 1.2: Slip and twin systems in Mg alloys.

based on the Eshelby-Frank-Nabarro solution [30] to a discrete dislocation pile-up model :

$$\sigma_Y = \sigma_0 + \frac{K_{HP}}{\sqrt{d}} \tag{1.1}$$

where σ_0 is the intercept(Hall-Petch intercept) of the linear relationship and denotes the grain size-independent component of the yield stress, and K_{HP} is the slope of the linear relation. K_{HP} is referred to as the "locking parameter" or Hall-Petch slope. This dependence on the average grain size arises indirectly through the dependence on the grain boundary(GB) itself. The grain size-induced strengthening of crystalline materials deforming through plastic slip is attributed to the blocking of slip bands(accomodating localized deformation) by GBs. The smaller the average grain

size, the larger the GB network, more effective is the blocking of slip bands which in turn implies higher stresses need to be applied to achieve the same level of macroscopic deformation. Similar empirical power-law relationships have also been found for other mechanical properties of polycrystalline materials in alloys other than mild steel [31], which has motivated a myriad of similar studies for various Mg alloys [26], [32, 33, 34, 35, 36, 37]. Cordero et al. [38] have presented an extensive review of the Hall-Petch effect while Yu et al. [5] have reviewed previous work on Hall-Petch relationship with specific focus to Mg alloys.

A characteristic of Mg alloys is the strong dependence of the Hall-Petch slope on the crystallographic texture, as evidenced by previous experimental studies [26, 33, 37, 27]. For example, Wang et al. [37] studied the tensile behavior of a commercial Mg AZ31B alloy exhibiting basal texture, relative to four average grain sizes and five different loading directions. They reported values of σ_0 in the range of 12 - 42 MPa and the Hall-Petch slope K_{HP} in the range 158 - 411 MPa $\mu m^{1/2}$. Wang et al. [33] studied the tensile deformation of friction stir processed and extruded specimens of Mg AZ31B alloy along the advancing direction, for a set of different grain sizes. They observed a strong texture dependence of the yield stress on the grain size for extruded samples recording $\sigma_0 \approx 80$ MPa and $K_{HP} \approx 303$MPa $\mu m^{1/2}$. This was in contrast to relatively weaker texture dependence for friction stir processed samples with $\sigma_0 \approx 10$ MPa and $K_{HP} \approx 160$MPa $\mu m^{1/2}$. Guan et al. [25] proposed a simple equation based on a dislocation pile-up model to compute K_{HP} for Mg AZ31B alloy for different textures depending on two effective parameters, which are based on the expected active slip systems. Table. 1.1 lists the Hall-Petch coefficients for Mg alloy

AZ31 [5], where it can be observed that the Hall-Petch slope is strongly linked to underlying texture, dictated by different processing conditions, loading paths and gran size ranges.

Sample	Processing	Loading path	$d(\mu m)$	K_{HP}(MPa $\mu m^{1/2}$)
AZ31 [37]	Rolling	Tension//TD	26-78	411
AZ31 [37]	Rolling	Tension//ND	26-78	228
AZ31 [27]	Rolling	Tension//RD	5-25	319
AZ31 [39]	Rolling	Compression//RD	13-43	472
AZ31 [40]	Extrusion	Tension//ED	3-11	303
AZ31 [41]	Extrusion	Compression//ED	3-23	291
AZ31 [34]	FSP	Tension//PD	1-25	119
AZ31 [34]	FSP	Tension//TD	1-25	236
AZ31 [41]	FSP	Tension//AD	2.6-6.1	161
AZ31 [42]	ECAP	Tension//FD	3-33	205
AZ31 [43]	ECAP	Tension//ED	5-35	170

Table 1.1: Literature review of the H-P slopes (K_{HP}) in Mg alloys for a variety of processing conditions and loading paths within a given range of average grain sizes (d). FSP, ECAP, AD and PD represent the friction stir processing, equal-channel angular processing, advancing direction and processing direction, respectively. RD, TD, and ND refer to the rolling, transverse and normal direction of a rolled plate, respectively. ED and FD are the extrusion direction and flow direction of a rod [5].

1.3. Crystal plasticity modeling of Mg alloys

Crystal plasticity(CP) is a very useful modeling framework at the continuum level to simulate the elasto-plastic response of crystalline materials [44, 45, 46, 47, 48]. Polycrystal plasticity models then link individual grain response to the overall mechanical response of a polycrystalline aggregate. These polycrystal models appear in various levels of sophistication and computational efficiency. The original application of crystal plasicity theory was performed with the Taylor assumption where all grains were considered to be subject to the same deformation [49, 6, 50, 51, 52, 53, 54, 55]. While this simplistic assumption satisfies compatibility it fails to account for equilibrium across GBs, which is a necessary condition to be satisfied. Alternative homogenization schemes have included the viscoplastic self-consistent(VPSC) schemes [56, 57, 58] which are based on describing each region as a viscoplastic inclusion embedded in the effective medium represented by the other grains. While these approaches are computationally efficient, they are not particularly well-suited for the study of polycrystalline materials where the grain morphologies and sizes need to be explicitly modeled and the variation of continuum mechanical fields throughout the microstructure are of interest. To model the heterogeneous variation of the continuum fields throughout the microstructure, discretized grain structures have been modeled [59, 60, 61, 62, 63, 64, 65, 66], where microstructural constituents are idealized grains with a fixed topology, or realistic polyhedral grains in two and three dimensions. Accordingly, a variety of CP models have been developed to study the mechanical behavior of HCP polycrystals incorporating crystallographic slip and

twinning with the governing equations solved numerically using the finite element method(FEM) [67, 68, 69, 70, 71, 72, 73]. Kalidindi [67] proposed a rate-dependent crystal plasticity framework, together with an efficient time-integration scheme, for incorporating the crystallography of deformation twinning in polycrystal plasticity models. Staroselsky et al. formulated a rate-independent constitutive model which accounts for both slip and twinning, a scheme to determine the active systems and the shear increments on both the active slip and twin systems. This constitutive model applied to the study of Mg alloy AZ31B [69]. Abdolvand et al. [70] developed a rate-dependent CPFE code incorporating a model accounting for twin nucleation and growth with application to Zircaloy-2. Fernandez et al. [71] proposed a crystal plasticity constitutive model for HCP metals involving slip and twin mechanisms with cross hardening, and applied it to the study of Mg alloy AZ31B. Their model cast light on role of pyramidal slip <c + a> versus compression twinning. Additionally, they also proposed a failure criterion based on the activity of basal slip. Zhang et al. developed a constitutive model based on [67] with experimentally motivated slip and twin evolution equations for the study of pure Mg. They investigated the role of pre-existing heterogeneities such as initial twin population and stiff, elastic inclusions on the single crystal macroscopic and microscopic responses. Liu at al. [73] employed 3D Voronoi grains based microstructure and the crystal plasticity constitutive model developed by Staroselsky et al. [69] to estimate the dependence of critical resolved shear stresses (CRSS) of different slip/twinning systems on temperature. In addition to FEM-based approaches, there have also been studies where CP models have been embedded in fast Fourier transform(FFT)-based

formulations [50, 51, 74, 58, 57, 75, 76] and more recent formulations based on the peridynamic theory of solid mechanics [77, 78, 79].

Due to the importance of twinning in the mechanical behavior of HCP materials, there have also been multiple studies dedicated to twinning behavior [80, 81, 82, 83, 84, 85, 86, 87, 88, 89]. Tome et al. developed a model for twinning applicable to zirconium alloys to model texture development under rolling, tension and compression models of deformation [80]. Beyerlein et al. [81] presented a basic probabilistic theory based on the Poisson process for the nucleation of deformation twins in HCP materials, where twin nucleation is assumed to rely on the dissociation of GB defects under stress into the required number of twinning partials to create a twin nucleus. Liu et al. [82] developed a model integration CP with a phase field framework where a stochastic model was used to nucleate twins with a Ginzburg-Landau relaxation governing their propagation and growth. Niezgoda et al. [83] developed a stochastic model of twin nucleation cast as a survival model parameterized by the local stress at the grain GB, and implemented it into a VPSC framework. Additionally, enhancements have also been made to CP models of twinning to incorporate detwinning [90, 91, 92, 93, 94], which is an important aspect when cyclic loading is an important consideration, e.g., in the fatigue behavior of Mg alloys [95, 96].

While classical crystal plasticity constitutive models have been extremely useful, by construction they are unable to capture the difference in mechanical behavior that arises from changes in the internal microstructural length scale, like the grain size. To address this issue one alternative has been the strain-gradient plasticity approach which has proven [97, 98, 99, 100] particularly useful in capturing the intrinsic size

effects arising in a number of plasticity-related phenomena based on the construct of geometrically necessary dislocations(GNDs). However, these models are relatively expensive to evaluate and also pose a challenge for parameter calibration since they involve a large number of internal variables. Additionally, the microscopic variables derived from the strain gradients are used to inform the hardening behavior while the effect of the microstructural length scale on the initial CRSS is set phenomenologically. Another approach is the use of cohesive elements to explicitly model grain boundaries within crystal plasticity where a traction–displacement relationship for grain boundaries is derived from either lower scale simulations such as molecular dynamics [101] or using dislocation theory [102, 103]. A simpler alternative has been to include a grain size-dependent contribution to the CRSS of individual slip systems by simply extending the Hall-Petch relationship to individual slip systems. Based on such a modification, there have been very few computational studies addressing the coupling between grain size and texture in Mg alloys. Jain et al. [104, 39] conducted studies using a grain size-dependent VPSC model on a rolled Mg alloy, which indicated the role of grain size associated with prismatic slip in the tensile behavior. Raesinia et al. [105] fit the affine VPSC model to the data in Jain et al. [39] through uniform scaling of the CRSS to establish a slip system-level Hall-Petch relationship, which involves the slip system-level Hall-Petch coefficient and the average grain size. Such VPSC models have also been used to explore the role of grain size on the twin growth [106], the density of twins [107], and also the correlation between the crystallographic orientation of the grain and corresponding twin variant selected [108]. Ravaji et al. [109] investigated the interacting effects between the grain size, loading direc-

tion and texture on the response of an Mg alloy. They investigated the role of grain size-texture coupling in reducing the net plastic anisotropy, the tension-compression asymmetry and the tempering of extension twinning with grain refinement across different textures and loading directions. Common in all these important studies is that a single average grain size is used to modify the CRSS for all the grains in the simulated microstructure. Moreover, this modification to the CRSS at the slip system level, which resembles the linear dependence on the inverse square-root of the average grain size, uses a constant Hall-Petch type parameter for a particular slip system for all the grains in the microstructure. In other words, the microstructural features are not captured directly in the parts of the constitutive model accounting for the grain size effect.

1.4. HR-EBSD measurements

In various applications, from structural engineering parts to semiconductor components, it is necessary to understand the state of stress fields in localized regions in the materials [110]. For example, strain accumulation in semiconductors could cause degradation of the device [111]; and stress concentration at twin/parent interface could result in crack initiation in polycrystalline materials [112]. For these reasons, experimental methods that can measure the local elastic stress/strain are desirable. The cross correlation-based EBSD strain characterization technique (HR-EBSD) is a novel measurement technique that provides the high spatial resolution that electron diffraction techniques can offer while not suffering so much from sample preparation [113]. This technique measures the elastic strain and lattice rotation

by cross-correlating electron backscatter patterns to capture a small shift of feature between two patterns [114, 115, 116, 117]. EBSD measurements can be used to image microstructural sections providing information regarding the morphology of grains and their orientations. The HR-EBSD technique can provide measurements of residual stresses and GND density distributions useful for obtaining insights on operating mechanisms from localized data.

1.5. Outline of thesis

This thesis attempts to address the problem of developing a quantitative model encoding the microstructural aspects in the grain size effect. This is performed by integrating experimental residual stress measurements ahead of blocked slip bands using HR-EBSD, theoretical dislocation pile-up models, some foundational hypotheses and crystal plasticity constitutive modeling, to construct parameters which encode the dependence of the slip resistance of individual slip systems on the grain size and the texture(via grain neighbours). We demonstrate this integration for a specific material system of Mg-4Al for which the relevant material parameters quantifying this effect are identified. Even though the procedure is demonstrated with Mg-4Al as a specific example, it is general enough to be extended to arbitrary crystalline materials where the grain size effect is of primary interest.

Chapter 2 describes the rate-dependent crystal plasticity constitutive model that forms the crystal plasticity formulation for our study. Details of the implementation in the PRISMS-Plasticity framework are presented along with the relevant prepro-

cessing and postprocessing tools, and concluding with some examples.

Chapter 3 details the integration of experimental pile-up stress measurements ahead of basal slip bands blocked by GBs, with theoretical pile-up stress expressions and some simplifying hypotheses to estimate the micro-Hall-Petch parameters for basal slip for different GBs. The micro-Hall-Petch parameters are then parametrized relative to some measures of compatibility for which the required information is obtained from crystal plasticity simulations of microstructural sections representing the neighborhoods of the GBs being investigated.

Chapter 4 details the integration of experimental pile-up stress measurements ahead of prismatic slip bands blocked by GBs, with theoretical pile-up stress expressions and some simplifying hypotheses to estimate the micro-Hall-Petch parameters for prismatic slip for different GBs. The micro-Hall-Petch parameters are then parametrized relative to some measures of compatibility for which the required information is obtained from crystal plasticity simulations of microstructural sections representing the neighborhoods of the GBs being investigated.

Chapter 5 covers the incorporation of the micro-Hall-Petch equation for basal and prismatic slip into the rate-dependent crystal plasticity constitutive model followed by the calibration of the constitutive model with experimental stress-strain curves, comparison with predictions from experimentally informed micro-Hall-Petch coefficients, and concluding with parametric studies to assess the model behavior.

Chapter 6 concludes with the contributions and proposes future directions for this thesis's work.

CHAPTER II

PRISMS-Plasticity Rate-Dependent Crystal Plasticity Model

In this chapter, the rate-dependent single crystal plasticity constitutive model is described. This includes the formulation and implementation into PRISMS-Plasticity crystal plasticity finite element framework(PRISMS-CPFE) [118, 119, 95] including both crystallographic slipping and twinning. This is followed by a brief overview of the PRISMS-CPFE workflow including the preprocessing and postprocessing tools and we conclude with a few numerical examples.

2.1. Rate-Dependent Single Crystal Constitutive Model

2.1.1. Crystal Plasticity Formulation

The primary kinematic ingredient of the constitutive model for an elastoplastic single crystal is the deformation gradient tensor $\boldsymbol{F}$, which is the tangent of a smooth deformation mapping that associates the positions of material points in the refer-

ence configuration to their corresponding positions in the deformed configuration. A multiplicative decomposition of the deformation gradient into elastic and plastic parts [120, 121] is assumed,

$$\boldsymbol{F} = \boldsymbol{F^e F^p} \tag{2.1}$$

$\boldsymbol{F^p}$ captures the homogenized distortion of the body as a consequence of crystallographic slip due to dislocation motion on specific slip systems and maps infinitesimal material fibers in the reference configuration to their counterparts in the intermediate configuration. $\boldsymbol{F^e}$ is the elastic part of the deformation gradient tensor which encodes elastic stretch and rotation of the lattice and maps the intermediate configuration to the deformed configuration. The plastic part of the velocity gradient in the intermediate configuration is related to the underlying crystallography through the plastic kinematic equation :

$$\boldsymbol{L^p} \coloneqq \boldsymbol{\dot{F}^p F^{p-1}} = \sum_{\alpha=1}^{n_s} \dot{\gamma}^\alpha \boldsymbol{S_0^\alpha} = \sum_{\alpha=1}^{n_s} \dot{\gamma}^\alpha \boldsymbol{m_0^\alpha} \otimes \boldsymbol{n_0^\alpha} \tag{2.2}$$

where $\boldsymbol{\dot{F}^p}$ denotes the material time derivative of $\boldsymbol{F^p}$, n_s is the total number of slip systems and $\dot{\gamma}^\alpha$ is the slip rate on slip system α ($\alpha \in \{1, 2, \ldots, n_s\}$). $\boldsymbol{m_0^\alpha}$ and $\boldsymbol{n_0^\alpha}$ are unit vectors associated with the slip direction and slip plane normal, respectively, for slip system α in the intermediate configuration. $\boldsymbol{S_0^\alpha}$ is the Schmid tensor corresponding to slip system α defined as the tensor product of $\boldsymbol{m_0^\alpha}$ and $\boldsymbol{n_0^\alpha}$. Eqn. 2.2 physically represents the shearing of the body from plastic flow on plane $\boldsymbol{n_0^\alpha}$ along direction $\boldsymbol{m_0^\alpha}$. The kinematics of single crystal slip is illustrated in Fig.

2.1. In the rate-dependent constitutive model a flow rule is prescribed where the

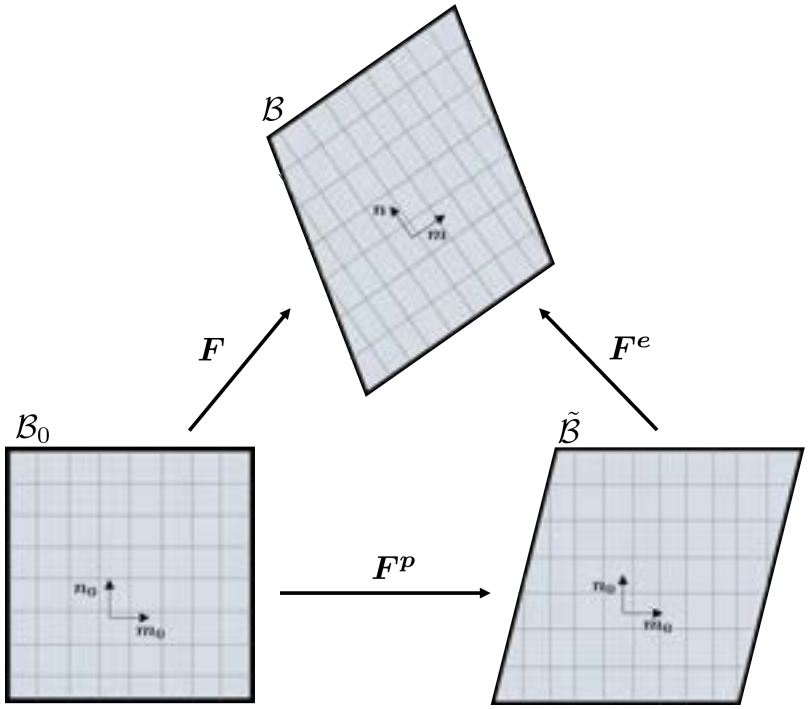

Figure 2.1: Different configurations assumed by the material - $\mathcal{B}_0$ denotes the reference configuration, $\mathcal{B}$ denotes the deformed configuration and $\tilde{\mathcal{B}}$ denotes the intermediate configuration obtained after relaxing the deformed configuration, preserving only the plastic deformation. The intermediate is isoclinic, i.e., $\det(\boldsymbol{F^p}) = 1$.

shearing rate on slip system α is explicitly related to the resolved shear stress, slip resistance and the backstress on that slip system. Following Asaro et. al. [122] and modifying it to include the backstress contribution, a phenomenological flow rule of the power-law type is prescribed,

$$\dot{\gamma}^\alpha = \dot{\gamma}^0 \left(\frac{\left| \tau^\alpha - w^\alpha \right|}{s^\alpha} \right)^m \operatorname{sign}(\tau^\alpha - w^\alpha) \tag{2.3}$$

where $\dot{\gamma}^0$ is the reference shearing rate and m is the strain-rate sensitivity exponent, both assumed to be identical for all slip systems. τ^α, w^α and s^α are the resolved shear stress, the backstress and the slip resistance, respectively, on slip system α. sign$(\cdot)$ denotes the signum function. Eqn. 2.3 is one possible regularization adopted to avert the under-determined system of equations arising in Eqn. 2.2 where there are 8 independent components of $\boldsymbol{L^p}$ while $n_s > 8$ for the crystal structures of interest. The slip system resistance accounts for isotropic hardening of the material while the backstress accounts for kinematic hardening important to capture tension-compression asymmetry of the material.

The Piola-Kirchoff-II stress in the intermediate configuration, $\boldsymbol{T}$ is related to the Piola-Kirchoff-I stress (defined in the reference configuration), and the Cauchy stress (defined in the deformed configuration) as follows :

$$\boldsymbol{T} = \boldsymbol{F^e}^{-1}\boldsymbol{P}\boldsymbol{F}^T\boldsymbol{F^e}^{-T} = \det(\boldsymbol{F^e})\boldsymbol{F^e}^{-1}\boldsymbol{\sigma}\boldsymbol{F^e}^{-T} \tag{2.4}$$

The elastic constitutive equation is motivated from a generalized version of standard Hooke's law where a linear relation relationship is prescribed between $\boldsymbol{T}$ and the Green-Lagrange elastic strain measure, $\boldsymbol{E^e}$ (elastic power conjugate to $\boldsymbol{T}$ as noted in Appendix A),

$$\boldsymbol{T} = \mathcal{L} \cdot \boldsymbol{E^e} = \frac{1}{2}\mathcal{L} \cdot (\boldsymbol{F^e}^T\boldsymbol{F^e} - \boldsymbol{I}) \tag{2.5}$$

where $\mathcal{L}$ denotes the fourth-order material stiffness tensor which is positive-definite and exhibits both major and minor symmetries typical of hyperelastic constitutive

laws . The '$\cdot$' denotes the product of a fourth-order and second-order tensor furnishing a second-order tensor, i.e., $\boldsymbol{A} = \mathcal{L} \cdot \boldsymbol{B} \implies A_{ij} = \mathcal{L}_{ijkl} B_{kl}$.
The resolved shear stress is expressed in terms of $\boldsymbol{T}$ as follows :

$$\tau^{\alpha} = \left(\boldsymbol{F}^{\boldsymbol{e}T} \boldsymbol{F}^{\boldsymbol{e}} \boldsymbol{T}\right) : \boldsymbol{S}_{\boldsymbol{0}}^{\boldsymbol{\alpha}} \tag{2.6}$$

where the ':' denotes the scalar product of second-order tensors, i.e., $\boldsymbol{A} : \boldsymbol{B} = A_{ij} B_{ij}$. Eqn. 2.6 is obtained by equating the continuum mechanical contribution of plastic power density to the power expended in crystallographic shearing on slip system α(Appendix A). The resolved shear stress is approximated by ignoring the effects of elastic stretching, which are not significant for the levels of deformation considered. This yields,

$$\tau^{\alpha} \approx \boldsymbol{T} : \boldsymbol{S}_{\boldsymbol{0}}^{\boldsymbol{\alpha}} \tag{2.7}$$

The evolution of slip resistance is prescribed following Kalidindi et al. [6],

$$\dot{s^{\alpha}} = \sum_{\alpha=1}^{n_s} q_{\alpha\beta} h_0 \left(1 - \frac{s^{\beta}}{s_s^{\beta}}\right)^{a} \left|\dot{\gamma}^{\beta}\right| \ ; \ s^{\alpha}(0) = s_0^{\alpha} \tag{2.8}$$

$$q_{\alpha\beta} = q + (1 - q)\tilde{\delta}_{\alpha\beta}$$

$$\tilde{\delta}_{\alpha\beta} = \begin{cases} 1 \ ; & \alpha, \beta \text{ are coplanar} \\ 0 \ ; & \text{otherwise} \end{cases} \tag{2.9}$$

where $q_{\alpha\beta}$ denotes the hardening multiplier contribution to slip system α arising

from slip on slip system β. h_0 is the hardening coefficient, q is the latent hardening ratio, s_s^β is the saturation value of the slip resistance on slip system β and a is the hardening exponent.

2.1.2. Backstress Formulation

With additional focus towards modeling fatigue behavior of polycrystals, a backstress formulation is implemented. This serves as the basic implementation and backbone for the open-source PRISMS-Fatigue framework [95], a platform that allows the material science and mechanics community to use and contribute to fatigue-related research and applications. As a part of this constitutive implementation, the backstress is modeled using a version of the Ohno-Wang backstress formulation [123] which was later modified by McDowell [124] to simulate ratcheting behavior in rail steels. On every slip system α two independent backstress components, i.e., w_1^α and w_2^α, are defined which evolve as follows

$$\begin{aligned} \dot{w_i^\alpha} &= h_i \dot{\gamma}^\alpha - r_i \left(\frac{|w_i^\alpha|}{b_i} \right)^{m_i} w_i^\alpha \left| \dot{\gamma}^\alpha \right| \ ; \quad (i = 1, 2) \\ w^\alpha &= \sum_{i=1}^{2} w_i^\alpha \end{aligned} \tag{2.10}$$

where h_i, r_i, b_i and m_i are constant model parameters with $b_i = h_i / r_i$ denoting the saturation value of the backstress.

2.1.3. Deformation Twinning

Twin systems are treated as slip systems with an underlying asymmetry in the shear direction, until they are reoriented. The crystallography of twins is depicted in Fig. 2.2 indicating the parent grain, twinned region and their corresponding orientations. The twinning formulation incorporated into PRISMS-CPFE closely follows

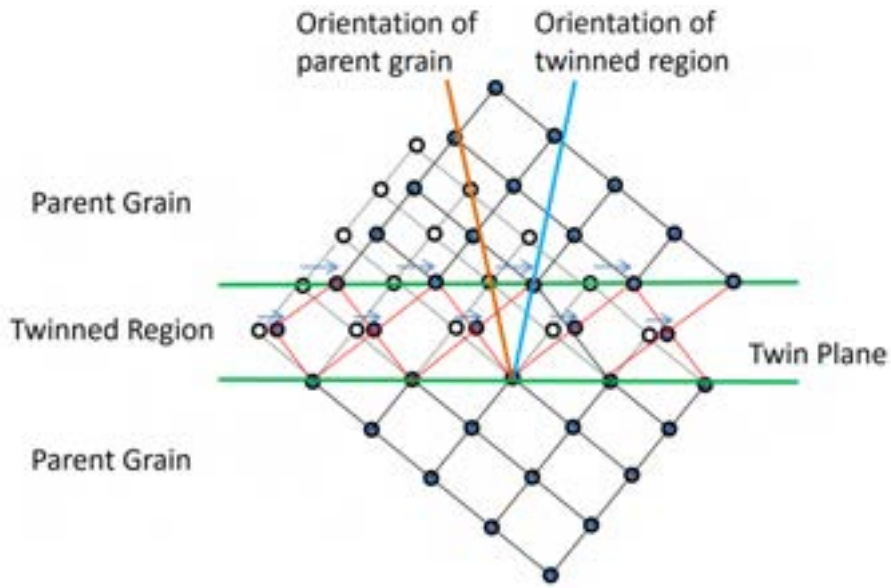

Figure 2.2: The orientation of the twinned region can be obtained by constructing the mirror image of the parent grain lattice with the twinning plane acting as the mirror plane.

the implementation by Staroselsky et al. [69] with two modifications - (i) Use of the predominant twin reorientation(PTR) scheme [80], and (ii) Reorienting quadrature points in place of entire grains. Under the PTR scheme, the fraction of the grain

associated with each twinning system is given by

$$g^{n,t_i} = \sum_{n_t} \Delta g^{n,t_i} \tag{2.11}$$

where $g^{n,t_i} = \frac{\Delta\gamma^{n,t_i}}{\gamma_S}$, n is the n^{th} quadrature point, n_t steps is the number of timesteps, t_i is the i^{th} twinning system and γ_S is the characteristic twin shear strain, which is calculated to be 0.129 for Magnesium [125]. The threshold fraction for twinning is calculated locally at each element making the method locally-sensitive

$$F_T = 0.25 \left(1 + \frac{f_N}{\sum_i g^{n,t_i}} \right) \tag{2.12}$$

where f_N is total reoriented volume fraction of the grain. If $g^{n,t_i} > F_T$, the quadrature point is reoriented to the appropriate orientation of the twin.

2.2. Incremental Constitutive Model

Here present the derivation of the incremental constitutive model important for numerical implementation. We start with Eqn. (2.2), whose implicit time discretization yields

$$\dot{\boldsymbol{F}}^{\boldsymbol{p}} = \left(\sum_{\alpha=1}^{n_s} \dot{\gamma}^{\alpha} \boldsymbol{S}_{\boldsymbol{0}}^{\boldsymbol{\alpha}} \right) \boldsymbol{F}^{\boldsymbol{p}} \implies \boldsymbol{F}^{\boldsymbol{p}} \approx \exp \left(\sum_{\alpha=1}^{n_s} \Delta\gamma^{\alpha} \boldsymbol{S}_{\boldsymbol{0}}^{\boldsymbol{\alpha}} \right) \boldsymbol{F}^{\boldsymbol{p}}(t) \tag{2.13}$$

where $\approx$ is used to denote a reasonable approximation, $\Delta\gamma^{\alpha} = \dot{\gamma}^{\alpha}\Delta t$ and $\exp(\cdot)$ denotes the matrix exponential defined using a power series(Appendix B). The elastic

constitutive law reads

$$\begin{aligned}\boldsymbol{T} &= \frac{1}{2}\mathcal{L}\cdot\left(\boldsymbol{F^{e}}^{T}\boldsymbol{F^{e}}-\boldsymbol{I}\right)=\frac{1}{2}\mathcal{L}\cdot\left(\boldsymbol{F^{p}}^{-T}\boldsymbol{F}^{T}\boldsymbol{F}\boldsymbol{F^{p}}^{-1}-\boldsymbol{I}\right)\\ &= \frac{1}{2}\mathcal{L}\cdot\left(\exp\left(\sum_{\alpha=1}^{n_s}-\Delta\gamma^{\alpha}\boldsymbol{S_0^{\alpha T}}\right)\boldsymbol{A}\exp\left(\sum_{\alpha=1}^{n_s}-\Delta\gamma^{\alpha}\boldsymbol{S_0^{\alpha}}\right)-\boldsymbol{I}\right)\end{aligned} \tag{2.14}$$

where $\boldsymbol{A} := \boldsymbol{F^{p}}^{-T}(t)\boldsymbol{F}^{T}\boldsymbol{F}\boldsymbol{F^{p}}^{-1}(t)$. Implicit time discretization of the isotropic hardening law reads

$$s^{\alpha} = s^{\alpha}(t)+\sum_{i=1}^{n_s}q_{\alpha\beta}h_0\left(1-\frac{s^{\beta}}{s_s^{\beta}}\right)^{a}\left|\Delta\gamma^{\beta}\right| \tag{2.15}$$

while implicit time discretization of the Ohno-Wang backstress equation takes the form,

$$w_i^{\alpha} = w_i^{\alpha}(t)+h_i\Delta\gamma^{\alpha}-r_i\left(\frac{|w_i^{\alpha}|}{b_i}\right)^{m_i}w_i^{\alpha}|\Delta\gamma^{\alpha}|\ ,\quad (i=1,2)\ ;\ w^{\alpha}=\sum_{i=1}^{2}w_i^{\alpha} \tag{2.16}$$

Combining Eqns. 2.14-2.16 yields the following system of equations

$$\begin{aligned}\boldsymbol{R_T} \coloneqq \boldsymbol{T}-\frac{1}{2}\mathcal{L}\cdot\Bigg(&\exp\left(\sum_{\alpha=1}^{n_s}-\Delta\gamma^{\alpha}(\boldsymbol{T},\boldsymbol{w},\boldsymbol{s})\boldsymbol{S_0^{\alpha T}}\right)\boldsymbol{A}\\ &\exp\left(\sum_{\alpha=1}^{n_s}-\Delta\gamma^{\alpha}(\boldsymbol{T},\boldsymbol{w},\boldsymbol{s})\boldsymbol{S_0^{\alpha}}\right)-\boldsymbol{I}\Bigg)=0\end{aligned} \tag{2.17}$$

$$\begin{aligned}\boldsymbol{R}_w^{\alpha,i} \coloneqq\ & w_i^{\alpha}-w_i^{\alpha}(t)-h_i\Delta\gamma^{\alpha}(\boldsymbol{T},\boldsymbol{w},\boldsymbol{s})+r_i\left(\frac{|w_i^{\alpha}|}{b_i}\right)^{m_i}\\ & w_i^{\alpha}|\Delta\gamma^{\alpha}(\boldsymbol{T},\boldsymbol{w},\boldsymbol{s})|=0\ ,\quad (i=1,2)\end{aligned} \tag{2.18}$$

$$\boldsymbol{R}_s^{\alpha} \coloneqq s^{\alpha} - s^{\alpha}(t) - \sum_{i=1}^{n_s} q_{\alpha\beta} h_0 \left(1 - \frac{s^{\beta}}{s_s^{\beta}}\right)^{a} \left|\Delta\gamma^{\beta}(\boldsymbol{T}, \boldsymbol{w}, \boldsymbol{s})\right| = 0 \tag{2.19}$$

where $\boldsymbol{w}$ denotes a vector comprising the $2n_s$ backstress components and $\boldsymbol{s}$ denotes a vector comprising the n_s slip resistances. Eqns. (2.17)-(2.19) form a total of $3n_s + 6$ equations in $3n_s + 6$ variables - $\boldsymbol{T}$, $\boldsymbol{w}$ and $\boldsymbol{s}$, whose solution we seek by employing a numerical root finding scheme outlined next.

2.3. Solution to Nonlinear System

To solve the nonlinear system, Newton iteration augmented with a cubic line search algorithm(Appendix C) is employed, which is more robust over the commonly used Newton-Raphson iteration. This choice is essential here since the typically large values of the strain rate sensitivity exponent m result in a stiff nonlinear system of equations which can render the Newton-Raphson iteration particularly helpless when initial guesses are not sufficiently close to the 'true' values of the state variables. The cubic line search algorithm adapts the choice of step length along the search direction based on certain conditions, improving the initial guess at the expense of minimal computational cost. More importantly, when the initial guess is sufficiently close to the 'true' values the Newton-Raphson step is adopted by the line search algorithm and quadratic convergence is achieved.

Instead of solving the nonlinear system of $3n_s + 6$ equations simultaneously, we first partition the system into two sets - (i) involving $\boldsymbol{T}$ and $\boldsymbol{w}$ which forms $2n_s + 6$ equations, and (ii) involving $\boldsymbol{s}$ which forms n_s equations. First the values of slip resistance on all n_s slip systems are specified for a given level of iteration, which we

refer to as the outer iteration. Let the vector of slip resistances corresponding to the j^{th} outer iteration be denoted by $\boldsymbol{s}^j$. Then Eqns. 2.17-2.18 are solved using the Newton's method augmented with a cubic line search algorithm, which constitutes the second level of iteration, referred to as the inner iteration . Let $[\boldsymbol{T}^{(j,k)}, \boldsymbol{w}^{(j,k)}]$ denote the estimate of the stress and backstress at the j^{th} outer and k^{th} inner iteration. The residual for the k^{th} inner iteration, $\boldsymbol{R}^{(j,k)}$, is then computed by evaluating Eqns. 2.17 - 2.18 at $[\boldsymbol{T}^{(j,k)}, \boldsymbol{w}^{(j,k)}]$. The Jacobian matrix, $\mathcal{J}^{(j,k)}$ comprises the partial derivative of the residual relative to $[\boldsymbol{T}, \boldsymbol{w}]$ evaluated at $[\boldsymbol{T}^{(j,k)}, \boldsymbol{w}^{(j,k)}]$, resulting in a $(2n_s + 6) \times (2n_s + 6)$ matrix,

$$\mathcal{J}^{(j,k)} = \begin{bmatrix} \frac{\partial \boldsymbol{R_T}}{\partial \boldsymbol{T}} & \frac{\partial \boldsymbol{R_T}}{\partial \boldsymbol{w}} \\ \frac{\partial \boldsymbol{R_w}}{\partial \boldsymbol{T}} & \frac{\partial \boldsymbol{R_w}}{\partial \boldsymbol{w}} \end{bmatrix}_{\boldsymbol{T}^{(j,k)}, \boldsymbol{w}^{(j,k)}}, \quad \boldsymbol{R}^{(j,k)} = \begin{bmatrix} \boldsymbol{R_T} \\ \boldsymbol{R_w} \end{bmatrix}_{\boldsymbol{T}^{(j,k)}, \boldsymbol{w}^{(j,k)}}$$

$$\left.\frac{\partial \boldsymbol{R_T}}{\partial \boldsymbol{T}}\right|_{\boldsymbol{T}^{(j,k)}, \boldsymbol{w}^{(j,k)}} = \mathcal{I}_s + \sum_{\alpha=1}^{n_s} (\mathcal{L} \cdot \boldsymbol{C}^{\alpha,(j,k)}) \otimes \left(\kappa^{\alpha}_{(j,k)} \boldsymbol{M}^{\alpha}\right) \tag{2.20}$$

$$\left.\frac{\partial \boldsymbol{R_T}}{\partial w_i^{\alpha}}\right|_{\boldsymbol{T}^{(j,k)}, \boldsymbol{w}^{(j,k)}} = -\kappa^{\alpha}_{(j,k)} \mathcal{L} \cdot \boldsymbol{C}^{\alpha,(j,k)} \tag{2.21}$$

$$\left.\frac{\partial \boldsymbol{R}_w^{\alpha,i}}{\partial \boldsymbol{T}}\right|_{\boldsymbol{T}^{(j,k)}, \boldsymbol{w}^{(j,k)}} = -\Bigg\{ h_i \kappa^{\alpha}_{(j,k)} - \left(\frac{\left| w_i^{\alpha,(j,k)} \right|}{b_i} \right)^{m_i} r_i w_i^{\alpha,(j,k)} \kappa^{\alpha}_{(j,k)} \operatorname{sign}(\boldsymbol{T}^{(j,k)} : \boldsymbol{S}_{\boldsymbol{0}}^{\boldsymbol{\alpha}} - w^{\alpha,(j,k)}) \Bigg\} \boldsymbol{M}^{\alpha} \tag{2.22}$$

$$\left.\frac{\partial \boldsymbol{R}_w^{\alpha,i}}{\partial w_j^{\beta}}\right|_{\boldsymbol{T}^{(j,k)}, \boldsymbol{w}^{(j,k)}} = \delta_{\alpha\beta}\delta_{ij} + h_i \delta_{\alpha\beta} \kappa^{\alpha}_{(j,k)} + \delta_{\alpha\beta}\delta_{ij}(m_i + 1) r_i \left(\frac{\left| w_i^{\alpha,(j,k)} \right|}{b_i} \right)^{m_i}$$

$$|\Delta\gamma^{\alpha}(\boldsymbol{T}^{(j,k)},\boldsymbol{w}^{(j,k)})| - \delta_{\alpha\beta} r_i \left(\frac{\left|w_i^{\alpha,(j,k)}\right|}{b_i}\right)^{m_i} w_i^{\alpha,(j,k)} \kappa^{\alpha}_{(j,k)} \text{sign}(\boldsymbol{T}^{(j,k)} : \boldsymbol{S_0^{\alpha}} - w^{\alpha,(j,k)}) \tag{2.23}$$

$$\boldsymbol{M}^{\alpha} \coloneqq \boldsymbol{S_0^{\alpha}} + \boldsymbol{S_0^{\alpha T}} - \text{diag}(\boldsymbol{S_0^{\alpha}}) \ , \ \kappa^{\alpha}_{(j,k)} \coloneqq \frac{\Delta\gamma^0 m}{s^{\alpha,j}} \left(\frac{\left|\boldsymbol{T}^{(j,k)} : \boldsymbol{S_0^{\alpha}} - w^{\alpha,(j,k)}\right|}{s^{\alpha,j}}\right)^{m-1}$$

$$\boldsymbol{C}^{\alpha,(j,k)} \coloneqq \frac{\partial(\exp \boldsymbol{M})}{\partial \boldsymbol{M}}\Big|_{-\boldsymbol{L^p}^T_{(j,k)}\Delta t} : \boldsymbol{S_0^{\alpha T}}, \ \boldsymbol{L^p}_{(j,k)} = \sum_{\alpha=1}^{n_s} \dot{\gamma}^{\alpha}(\boldsymbol{T}^{(j,k)}, \boldsymbol{w}^{(j,k)}, \boldsymbol{s}^j) \boldsymbol{S_0^{\alpha}}$$

where $\mathcal{I}_s$ represents the symmetric fourth-order identity tensor. $\text{diag}(\boldsymbol{M})$ denotes a diagonal matrix with the main diagonal coinciding with that of $\boldsymbol{M}$ and remaining entries zero and $\Delta\gamma^0 \coloneqq \dot{\gamma}^0 \Delta t$. Computation of $\boldsymbol{C}^{\alpha,(j,k)}$ involves evaluating the Gâteaux derivative of the matrix exponential whose theoretical and numerical implementation is outlined in Appendix B. Once convergence of the stress and backstress is achieved within set tolerances, denoted by $[\boldsymbol{T}^j, \boldsymbol{w}^j]$, the slip increment for the outer iteration, $\Delta\gamma^{\alpha,j}$, is computed. This slip increment is then used to update the slip resistance for the $(j+1)^{\text{th}}$ outer iteration using Eqn. 2.15 with the following update

$$s^{\alpha,j+1} = s^{\alpha}(t) + \sum_{i=1}^{n_s} q_{\alpha\beta} h_0 \left(1 - \frac{s^{\beta,j}}{s_s^{\beta}}\right)^a \left|\Delta\gamma^{\beta,j}\right| \tag{2.24}$$

The line search algorithm requires the following quantities as inputs

$$f^{(j,k)} = 0.5 \boldsymbol{R}^{(j,k)} \cdot \boldsymbol{R}^{(j,k)} \ , \ \boldsymbol{v}^{(j,k)} = \begin{bmatrix} \boldsymbol{T}^{(j,k)} \\ \boldsymbol{w}^{(j,k)} \end{bmatrix}$$

$$\boldsymbol{d}^{(j,k)} = -\left(\mathcal{J}^{(j,k)}\right)^{-1} \boldsymbol{R}^{(j,k)}$$

$$\boldsymbol{g}^{(j,k)} = 0.5\left(\mathcal{J}^{(j,k)} + \left(\mathcal{J}^{(j,k)}\right)^T\right)\boldsymbol{R}^{(j,k)} \tag{2.25}$$

where $f^{(j,k)}$ denotes the objective function to be extremized, $\boldsymbol{v}^{(j,k)}$ the state vector from the inner iteration comprising of the stress and backstress vectors, $\boldsymbol{d}^{(j,k)}$ the search direction and $\boldsymbol{g}^{(j,k)}$ the gradient of $f^{(j,k)}$ relative to the state vector $\boldsymbol{v}^{(j,k)}$. The outer and inner iterations continue to be evaluated until convergence is simultaneously achieved in the stress and the backstress from the inner iteration, and the slip resistances from the outer iteration. Tolerances are set for both levels of iteration, and to prevent indefinite looping a maximum number of iterations is enforced. The converged values of the stress, backstress components, and slip resistances at the end of the previous deformation step are chosen as initial guesses for the iterative solver.

2.4. Deformation Solver

The kinematic problem can be expressed in Lagrangian framework as

$$\nabla_0 \cdot \boldsymbol{P} + \boldsymbol{f} = 0 \tag{2.26}$$

where $\nabla_0 \cdot (\ )$ is the divergence of the argument in the initial reference configuration and $\boldsymbol{f}$ is the reference body force. The principle of incremental virtual work states that $\mathcal{B}_0$ is in equilibrium if and only if the Piola-Kirchoff-I stress field, $\boldsymbol{P}$, satisfies the virtual work functional for any kinematically admissible test function $\delta\tilde{\boldsymbol{u}}$,

$$\mathcal{G}(\delta\boldsymbol{u}, \delta\tilde{\boldsymbol{u}}) \equiv \int_{\mathcal{B}_0} \left(\boldsymbol{P} \cdot \nabla_0 \left(\delta\tilde{\boldsymbol{u}}\right) - \boldsymbol{f} \cdot \delta\tilde{\boldsymbol{u}}\right) dV - \int_{\partial\mathcal{B}_0} \boldsymbol{\lambda} \cdot \delta\tilde{\boldsymbol{u}}\ dA = 0\ ;\ \forall\ \delta\tilde{\boldsymbol{u}} \in \mathcal{V} \tag{2.27}$$

where $\delta\boldsymbol{u}$ is the incremental displacement field, $\mathcal{V}$ is the vector space of all admissible test functions in the material domain, $\boldsymbol{f}$ denotes the reference body force density and $\boldsymbol{\lambda}$ denotes the traction field. The dependence of $\mathcal{G}$ on the unknown function $\delta\boldsymbol{u}$ follows from the constitutive dependence of the stress tensor on the strain tensor which, in turn depends on the displacement field $\boldsymbol{u}$. In other words, $\boldsymbol{P}$ depends on $\boldsymbol{F}$ via the constitutive response of the material, which is turns is derivable from the displacement field via $\boldsymbol{F} = \boldsymbol{I} + \nabla_0\boldsymbol{u}$.

Under the finite element approximation, the displacement field $\boldsymbol{u}$ and the test function $\delta\tilde{\boldsymbol{u}}$ are approximated using a finite number of interpolation functions, rendering it now an element of $\tilde{\mathcal{V}}$, which is a finite-dimensional vector space of all admissible interpolated test functions. Using identical interpolation functions to approximate the displacement field $\boldsymbol{u}$ completes the Bubnov-Galerkin finite element approximation to obtain a nonlinear system of equations with a finite number of degrees of freedom, amenable to numerical treatment. The Newton-Raphson scheme augmented with line search is employed to solve the nonlinear system. Assembly of the global stiffness matrix for the deformation solver requires computation of the material tangent modulus, denoted by $\mathcal{T}$ and defined via the differential relation $\delta\boldsymbol{P} = \mathcal{T} \cdot \delta\boldsymbol{F}$.

2.5. Material Tangent Modulus

We start with the relation between $\boldsymbol{\sigma}$, $\boldsymbol{T}$ and $\boldsymbol{P}$ which are

$$\boldsymbol{P} = \det(\boldsymbol{F})\boldsymbol{\sigma}\boldsymbol{F}^{-T} \tag{2.28}$$

$$\boldsymbol{T} = \det(\boldsymbol{F}^{\boldsymbol{e}})\boldsymbol{F}^{\boldsymbol{e}-1}\boldsymbol{\sigma}\boldsymbol{F}^{\boldsymbol{e}-T} \tag{2.29}$$

The additional restriction that plastic deformation is isochoric implies $\det(\boldsymbol{F^p}) = 1 \implies \det(\boldsymbol{F}) = \det(\boldsymbol{F^e})$. Then

$$\boldsymbol{P} = \boldsymbol{F^e T F^{eT} F^{-T}} \tag{2.30}$$

Computing the variation of the LHS and RHS of Eqn. 2.30 results in

$$\begin{aligned}\delta\boldsymbol{P} &= \delta(\boldsymbol{F^e T F^{eT} F^{-T}}) \\ &= \delta\boldsymbol{F^e T F^{eT} F^{-T}} + \boldsymbol{F^e}\delta\boldsymbol{T F^{eT} F^{-T}} + \boldsymbol{F^e T}\delta\boldsymbol{F^{eT} F^{-T}} + \boldsymbol{F^e T F^{eT}}\delta(\boldsymbol{F^{-T}})\end{aligned} \tag{2.31}$$

From the elastic constitutive relation we have

$$\begin{aligned}\boldsymbol{T} = \mathcal{L}\cdot\boldsymbol{E^e} &= \frac{1}{2}\mathcal{L}\cdot\left(\boldsymbol{F^{eT}F^e} - \boldsymbol{I}\right) \\ \implies \delta\boldsymbol{T} &= \frac{1}{2}\mathcal{L}\cdot\left(\delta\boldsymbol{F^{eT}F^e} + \boldsymbol{F^{eT}}\delta\boldsymbol{F^e}\right) = \mathcal{L}\cdot\left(\boldsymbol{F^{eT}}\delta\boldsymbol{F^e}\right)\end{aligned} \tag{2.32}$$

where the last equality follows due to the minor symmetries of $\mathcal{L}$. Additionally, $\delta(\boldsymbol{F^{-T}})$ can be obtained as follows

$$\begin{aligned}\boldsymbol{F}\boldsymbol{F}^{-1} = \boldsymbol{I} &\implies \delta\boldsymbol{F}\boldsymbol{F}^{-1} + \boldsymbol{F}\delta(\boldsymbol{F}^{-1}) = \boldsymbol{0} \\ \implies \delta\boldsymbol{F}^{-1} = -\boldsymbol{F}^{-1}\delta\boldsymbol{F}\boldsymbol{F}^{-1} &\implies \delta\boldsymbol{F}^{-T} = -\boldsymbol{F}^{-T}\delta\boldsymbol{F}^{T}\boldsymbol{F}^{-T}\end{aligned} \tag{2.33}$$

Substituting Eqns. (2.32)-(2.33) in Eqn. (2.31) results in

$$\delta\boldsymbol{P} = \delta\boldsymbol{F^e T F^{eT} F^{-T}} + \boldsymbol{F^e}\mathcal{L}\cdot\left(\boldsymbol{F^{eT}}\delta\boldsymbol{F^e}\right)\boldsymbol{F^{eT}F^{-T}}$$

$$+ \boldsymbol{F^e T} \delta \boldsymbol{F^{e}}^T \boldsymbol{F}^{-T} - \boldsymbol{F^e T F^{e}}^T \boldsymbol{F}^{-T} \delta \boldsymbol{F}^T \boldsymbol{F}^{-T} \tag{2.34}$$

Then the computation of $\mathcal{T}$ depends completely on the computation of $\mathcal{F}$ defined by the differential relation $\delta \boldsymbol{F^e} = \mathcal{F} \cdot \delta \boldsymbol{F}$. To accomplish this we invoke the following relationships

$$\boldsymbol{F} = \boldsymbol{F^e F^p} \implies \delta \boldsymbol{F} = \delta \boldsymbol{F^e F^p} + \boldsymbol{F^e} \delta \boldsymbol{F^p} \tag{2.35}$$

Additionally

$$\begin{aligned} \dot{\boldsymbol{F}}^{\boldsymbol{p}} = \boldsymbol{L^p F^p} &\implies \boldsymbol{F^p} \approx \exp\left(\boldsymbol{L^p} \Delta t\right) \boldsymbol{F^p}(t) \\ &= \exp\left(\sum_{\alpha=1}^{n_s} \dot{\gamma}^\alpha \Delta t \boldsymbol{S_0^\alpha}\right) \boldsymbol{F^p}(t) = \exp\left(\sum_{\alpha=1}^{n_s} \Delta\gamma^\alpha \boldsymbol{S_0^\alpha}\right) \boldsymbol{F^p}(t) \end{aligned} \tag{2.36}$$

where $\Delta\gamma^\alpha := \dot{\gamma}^\alpha \Delta t$ Define the quantity $\mathcal{P}$ by $\delta \boldsymbol{F^p} = \mathcal{P} \cdot \delta \boldsymbol{F^e}$. Then Eqn. (2.35) takes the form

$$\delta \boldsymbol{F} = \delta \boldsymbol{F^e F^p} + \boldsymbol{F^e} \left(\mathcal{P} \delta \boldsymbol{F^e}\right) \tag{2.37}$$

Taking a variation of the LHS and RHS of Eqn. (2.36) results in

$$\begin{aligned} \delta \boldsymbol{F^p} &= \delta\left(\exp\left(\sum_{n=1}^{n_s} \Delta\gamma^\alpha \boldsymbol{S_0^\alpha}\right)\right) \boldsymbol{F^p}(t) = \frac{\partial(\exp \boldsymbol{M})}{\partial \boldsymbol{M}}\Big|_{\boldsymbol{L^p} \Delta t} : \left(\sum_{\alpha=1}^{n_s} \delta\Delta\gamma^\alpha \boldsymbol{S_0^\alpha}\right) \boldsymbol{F^p}(t) \\ &= \left(\sum_{\alpha=1}^{n_s} \frac{\partial(\exp \boldsymbol{M})}{\partial \boldsymbol{M}}\Big|_{\boldsymbol{L^p} \Delta t} : \boldsymbol{S_0^\alpha} \delta\Delta\gamma^\alpha\right) \boldsymbol{F^p}(t) \end{aligned}$$

$$= \sum_{\alpha=1}^{n_s} \left(\frac{\partial(\exp \boldsymbol{M})}{\partial \boldsymbol{M}}\Big|_{\boldsymbol{L^p}\Delta t} : \boldsymbol{S_0^\alpha} \right) \boldsymbol{F^p}(t). \left(\frac{\partial \Delta\gamma^\alpha}{\partial \boldsymbol{F^e}} : \delta \boldsymbol{F^e} \right) \tag{2.38}$$

In the rate-dependent constitutive model, slip increments are expressed phenomenologically as follows

$$\Delta\gamma^\alpha = \Delta\gamma^0 \left(\frac{\left| \boldsymbol{T} : \boldsymbol{S_0^\alpha} - w^\alpha \right|}{s^\alpha} \right)^m \text{sign}\left(\boldsymbol{T} : \boldsymbol{S_0^\alpha} - w^\alpha \right) \tag{2.39}$$

Assuming sign $(\boldsymbol{T} : \boldsymbol{S_0^\alpha} - w^\alpha)$ remains unchanged upon computing the variation, we have

$$\begin{aligned}
\delta(\Delta\gamma^\alpha) &= \Delta\gamma^0 \delta \left[\left(\frac{\left| \boldsymbol{T} : \boldsymbol{S_0^\alpha} - w^\alpha \right|}{s^\alpha} \right)^m \right] \text{sign}(\boldsymbol{T} : \boldsymbol{S_0^\alpha} - w^\alpha) \\
&= \Delta\gamma^0 m \left(\frac{\left| \boldsymbol{T} : \boldsymbol{S_0^\alpha} - w^\alpha \right|}{s^\alpha} \right)^{m-1} \cdot \delta \left(\frac{\boldsymbol{T} : \boldsymbol{S_0^\alpha} - w^\alpha}{s^\alpha} \right) \\
&= \Delta\gamma^0 m \left(\frac{\left| \boldsymbol{T} : \boldsymbol{S_0^\alpha} - w^\alpha \right|}{s^\alpha} \right)^{m-1} \left(\frac{\delta \boldsymbol{T} : \boldsymbol{S_0^\alpha} - \delta w^\alpha}{s^\alpha} - \left(\frac{\boldsymbol{T} : \boldsymbol{S_0^\alpha} - w^\alpha}{s^\alpha . s^\alpha} \right) \delta s^\alpha \right) \\
&= \kappa^\alpha \left(\delta \boldsymbol{T} : \boldsymbol{S_0^\alpha} - \delta w^\alpha - \left(\frac{\boldsymbol{T} : \boldsymbol{S_0^\alpha} - w^\alpha}{s^\alpha} \right) \delta s^\alpha \right) \\
&\implies \delta(\Delta\gamma^\alpha) + \kappa^\alpha \delta w^\alpha + \frac{m \Delta\gamma^\alpha}{s^\alpha} \delta s^\alpha = \kappa^\alpha \delta \boldsymbol{T} : \boldsymbol{S_0^\alpha}
\end{aligned} \tag{2.40}$$

Invoking the evolutionary equations prescribed for s^α and w^α to compute δs^α and δw^α respectively, we have

$$\dot{s^\alpha} = \sum_{\beta=1}^{n_s} h_{\alpha\beta} \left| \dot{\gamma}^\beta \right| = \sum_{\beta=1}^{n_s} q_{\alpha\beta} h_\beta \left| \dot{\gamma}^\beta \right| = \sum_{\beta=1}^{n_s} q_{\alpha\beta} h_0 \left(1 - \frac{s^\beta}{s_s^\beta} \right)^a \left| \dot{\gamma}^\beta \right|$$

$$
\begin{aligned}
&\implies s^{\alpha} = s^{\alpha}(t) + \sum_{\beta=1}^{n_s} q_{\alpha\beta} h_0 \left(1 - \frac{s^{\beta}}{s_s^{\beta}}\right)^{a} \left|\Delta\gamma^{\beta}\right| \\
&\implies \delta s^{\alpha} = \sum_{\beta=1}^{n_s} q_{\alpha\beta} h_0 \left(1 - \frac{s^{\beta}}{s_s^{\beta}}\right)^{a} \delta(\Delta\gamma^{\beta}).\mathrm{sign}(\Delta\gamma^{\beta}) \\
&\qquad\qquad - \sum_{\beta=1}^{n_s} \frac{q_{\alpha\beta} h_0 a}{s_s} \left(1 - \frac{s^{\beta}}{s_s^{\beta}}\right)^{a-1} \left|\Delta\gamma^{\beta}\right| \delta s^{\beta} \\
&\implies \sum_{\beta=1}^{n_s} \left(\delta_{\alpha\beta} + \frac{q_{\alpha\beta} h_0 a}{s_s^{\beta}} \left(1 - \frac{s^{\beta}}{s_s^{\beta}}\right)^{a-1} \left|\Delta\gamma^{\beta}\right|\right) \delta s^{\beta} = \\
&\qquad\qquad \sum_{\beta=1}^{n_s} q_{\alpha\beta} h_0 \left(1 - \frac{s^{\beta}}{s_s^{\beta}}\right)^{a} \delta(\Delta\gamma^{\beta}).\mathrm{sign}(\Delta\gamma^{\beta}) \\
&\implies [\delta s] = \boldsymbol{P}^{-1}.\boldsymbol{Q}[\delta(\Delta\gamma)]
\end{aligned}
\tag{2.41}
$$

where $[\delta s]$ and $[\delta(\Delta\gamma)]$ denote vectors comprising the variations of the slip resistance and slip increments, respectively.

$$
\begin{aligned}
&\dot{w_i^{\alpha}} = h_i \dot{\gamma}^{\alpha} - r_i \left(\frac{|w_i^{\alpha}|}{b_i}\right)^{m_i} w_i^{\alpha} \left|\dot{\gamma}^{\alpha}\right| \qquad (i = 1, 2) \\
&\implies w_i^{\alpha} = w_i^{\alpha}(t) + h_i \Delta\gamma^{\alpha} - r_i \left(\frac{|w_i^{\alpha}|}{b_i}\right)^{m_i} w_i^{\alpha} |\Delta\gamma^{\alpha}| \\
&\implies \delta w_i^{\alpha} = h_i \delta(\Delta\gamma^{\alpha}) - r_i \left(\frac{|w_i^{\alpha}|}{b_i}\right)^{m_i} w_i^{\alpha} \mathrm{sign}(\Delta\gamma^{\alpha}) \delta(\Delta\gamma^{\alpha}) \\
&\qquad\qquad - r_i (m_i + 1) \left(\frac{|w_i^{\alpha}|}{b_i}\right)^{m_i} |\Delta\gamma^{\alpha}| \delta w_i^{\alpha} \\
&\implies \delta w_i^{\alpha} = \frac{h_i - r_i \left(\frac{|w_i^{\alpha}|}{b_i}\right)^{m_i} w_i^{\alpha} \mathrm{sign}(\Delta\gamma^{\alpha})}{1 + r_i (m_i + 1) \left(\frac{|w_i^{\alpha}|}{b_i}\right)^{m_i} |\Delta\gamma^{\alpha}|} \delta(\Delta\gamma^{\alpha})
\end{aligned}
$$

$$\implies \delta w^{\alpha} = \sum_{i=1}^{2} \frac{h_i - r_i \left(\frac{|w_i^{\alpha}|}{b_i}\right)^{m_i} w_i^{\alpha} \text{sign}(\Delta\gamma^{\alpha})}{1 + r_i(m_i+1)\left(\frac{|w_i^{\alpha}|}{b_i}\right)^{m_i} |\Delta\gamma^{\alpha}|} \delta(\Delta\gamma^{\alpha}) \tag{2.42}$$

Substituting Eqns. (2.41)-(2.42) in the LHS and Eqn. (2.32) in the RHS of Eqn. (2.40) results in a matrix-vector equation that relates $\delta(\boldsymbol{\Delta\gamma})$ to $[\delta \boldsymbol{F^e}]$, resulting in an equation of the form

$$\boldsymbol{M}.\delta(\boldsymbol{\Delta\gamma}) = \boldsymbol{N}.[\delta \boldsymbol{F^e}] \tag{2.43}$$

where $\boldsymbol{M}$ is a square matrix. If $\boldsymbol{M}$ is invertible then

$$\delta(\boldsymbol{\Delta\gamma}) = \boldsymbol{M}^{-1}\boldsymbol{N}.[\delta \boldsymbol{F^e}] \tag{2.44}$$

which can be substituted in Eqn. (2.38) to obtain $\mathcal{P}$. Substituting $\mathcal{P}$ in Eqn. (2.35) results in construction of $\mathcal{F}$, which on substituting in Eqn. (2.34) completes the computation of $\mathcal{T}$.

2.6. PRISMS-CPFE Workflow

The first important feature of the PRISMS-CPFE software is the integration with experimental characterization schemes, such as electron backscatter diffraction (EBSD) and synchrotron X-ray diffraction. The data obtained from characterization techniques is then fed into softwares used for generating synthetic microstructures using two packages in particular - DREAM.3D [126] and Neper [127]. The material properties and algorithm details are included in an input file, which also contains informa-

tion about the files containing the microstructure mesh. The PRISMS- CPFE [119] code is then used to execute a simulation given the input file and other associated files. The postprocessing step is accomplished through integration with two packages - MTEX [128, 129] for texture analysis and Paraview for visualization of mechanical fields. The final step involves integration with Materials Commons [130] - a virtual collaboration space and repository for curating, archiving and disseminating information from experiments and computations. This workflow is illustrated in Fig. 2.3.

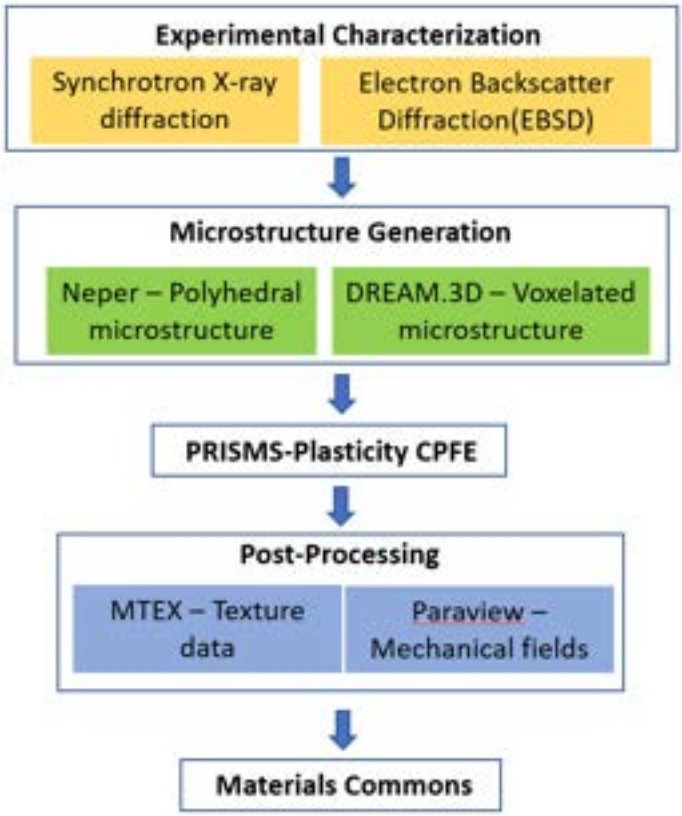

Figure 2.3: PRISMS-CPFE Workflow.

2.7. Examples

We present three numerical examples with the rate-dependent formulation implemented into PRISMS-CPFE : (i) Simple compression of oxygen free high conductivity(OFHC)-copper including purely isotropic hardening [2], (ii) Simple tension of β-Ti alloy Timetal 21S including purely isotropic hardening [3], and (ii) Cyclic deformation of Al 7075-T6 including purely kinematic hardening.

2.7.1. Example I : Simple Compression of OFHC-Cu polycrystal

We consider simple compression of FCC polycrystal with properties of OFHC copper [6] where their polycrystal was composed of 343 orientations sampled from a random distribution representative of random texture. We setup a simulation with a 200 grain polycrystal composed of 28,992 elements [119, 131] used for a similar comparison . The constitutive model for this exercise includes only the power-law isotropic hardening described earlier. The volxelated microstructure and pole figures are visualized in Fig. 2.4. The elastic constants of $C_{11} = 170$ GPa, $C_{12} = 124$ GPa, and $C_{44} = 75$ GPa were used. The crystal plasticity constitutive model parameters of OFHC-Cu alloy used for this study are presented in Table 2.1.

m	$\dot{\gamma}^0(\mathrm{s}^{-1})$	s_0^α(MPa)	h_0 (MPa)	s_s^α(MPa)	a	q
70	0.001	16	180	148	2.25	1.4

Table 2.1: Crystal plasticity constitutive model parameters for OFHC-Cu [6].

The polycrystal cubes were subject to 15% compressive engineering strain along the

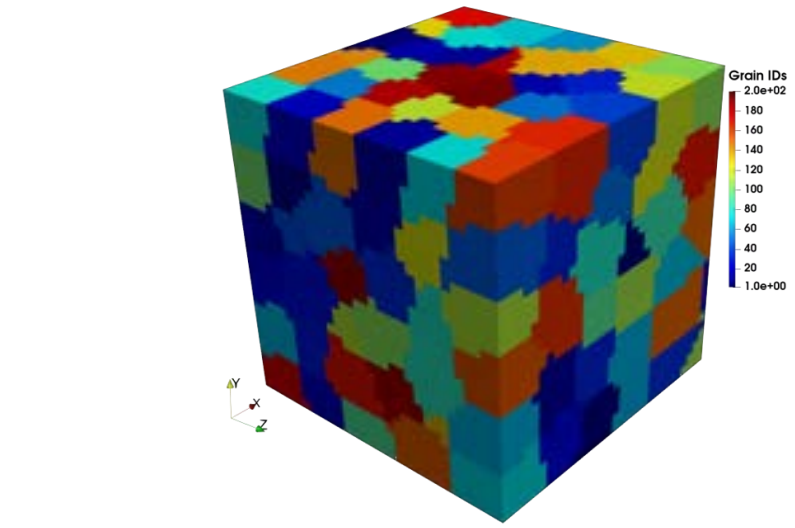

(a)

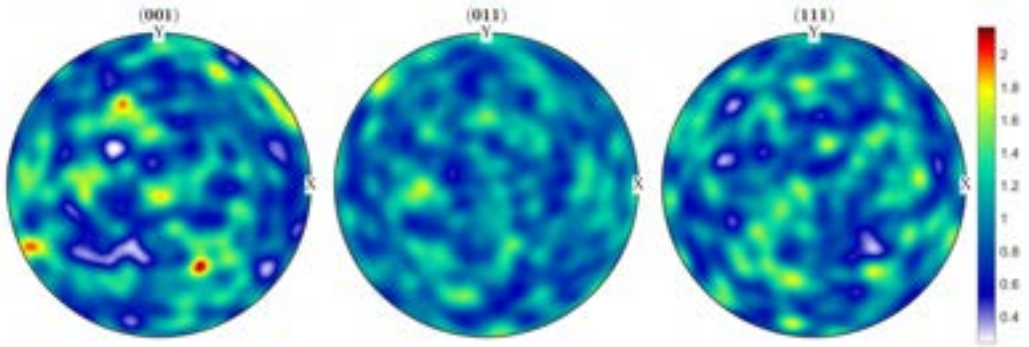

(b)

Figure 2.4: (a) Visualization of synthetic microstructure (b) Pole figures.

x-direction with simple compression boundary conditions, setup within PRISMS-CPFE. Fig. 2.5 depicts the variation of the equivalent stress and strain fields, and comparison of stress-strain curves. The underestimate in the stress arises because the crystal plasticity model employed by Anand et al. was a rate-independent model on a polycrystal where each element of the mesh was a distinct orientation while the current rate-dependent model is a regularization of the otherwise stiff rate-independent model.

2.7.2. Example II : Simple tension of Timetal 21S

In BCC materials, slip can occur on 48 distinct slip systems represented by three families of planes: 12 systems are in the <1 1 1> {1 1 0} family, 12 in the <1 1 1> {1 1 2} family, and 24 in the <1 1 1>{1 2 3} family. The material behavior can also be approximated by considering a subset of the total number of slip systems. Accordingly, 12 slip systems of <1 1 1>{1 1 0} family are considered in this example. DREAM.3D is used to generate the initial voxelated microstructure consisting of a total of 92 grains. Fig. 2.6 present the initial microstructure and pole figures. A structured linear hexahedral mesh is superposed on this voxelated texture output of DREAM.3D such that each element of the finite element mesh corresponds to a voxel of the RVE. The total number of elements is $200,192$. Simple tension boundary conditions are enforced with a tensile strain of 2.5% in the y-direction. The elastic constants of $C_{11} = 97.7$ GPa, $C_{12} = 82.7$ GPa, and $C_{44} = 37.5$ GPa were used. The crystal plasticity constitutive parameters for Timetal 21S are presented in Table. 2.2.

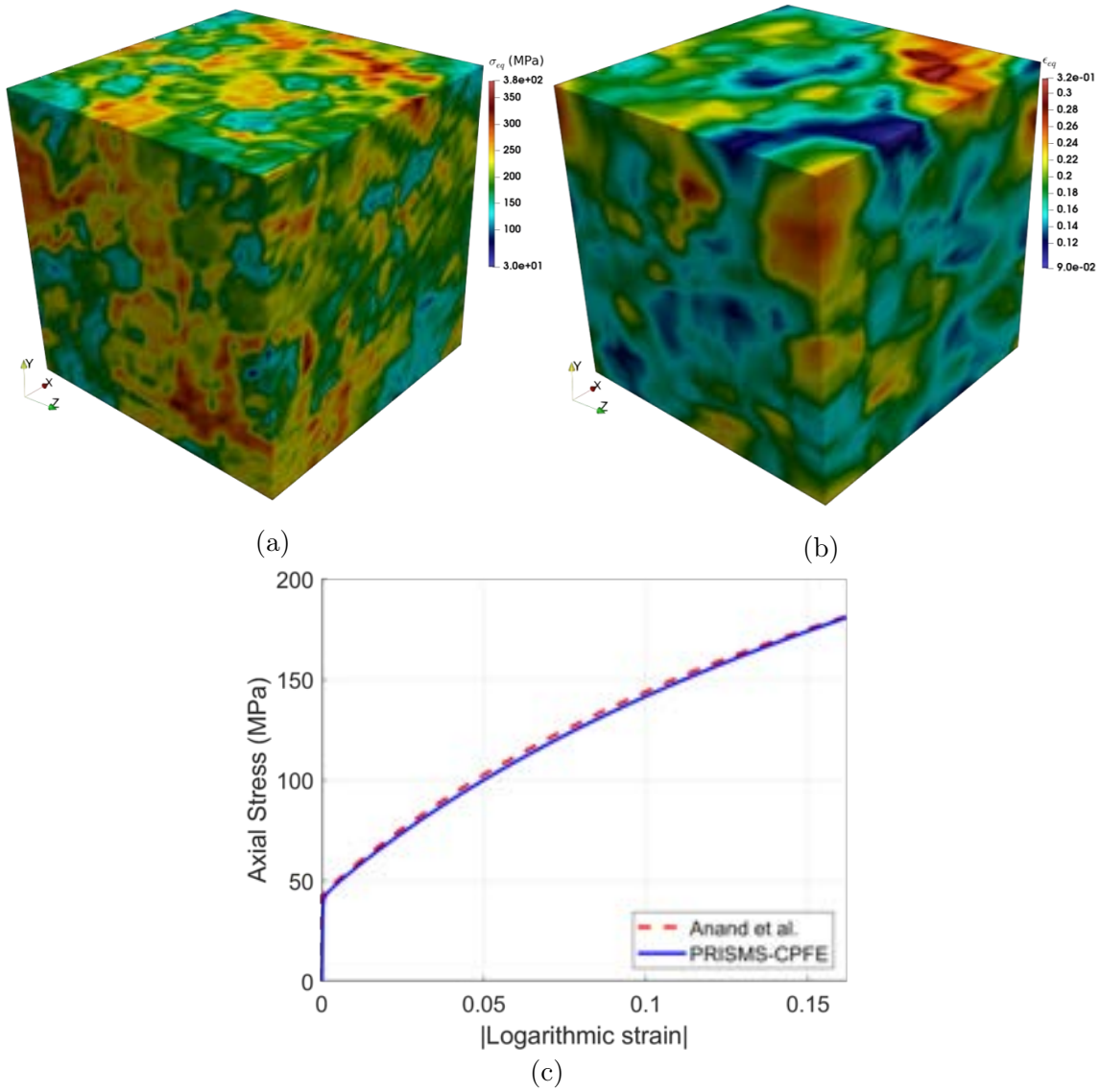

Figure 2.5: (a) Variation in von Mises equivalent stress field throughout the microstructure, and (b) Variation in von Mises equivalent strain field throughout the microstructure, and (c) Stress-strain curve comparison between rate-dependent model implemented in PRISMS-CPFE and the rate-independent model of Anand et al. [2].

m	$\dot{\gamma}^0(\mathrm{s}^{-1})$	s_0^α(MPa)	h_0 (MPa)	s_s^α(MPa)	a	q
50	0.0023	200	1500	500	0.1	1.4

Table 2.2: Crystal plasticity constitutive model parameters for Timetal 21S [3]

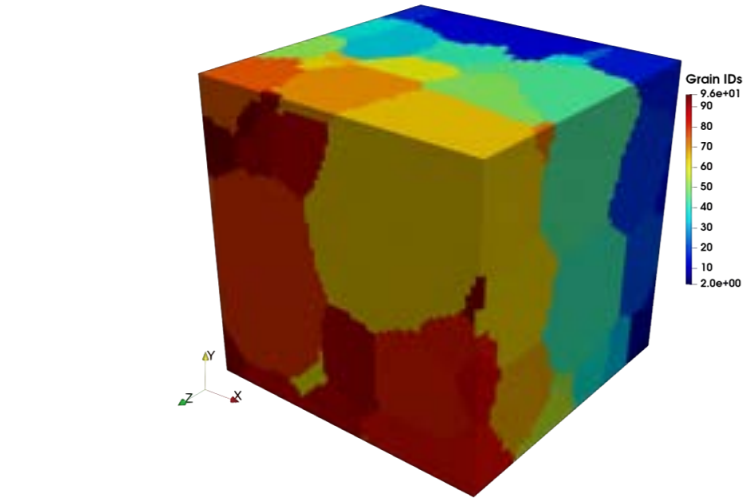

(a)

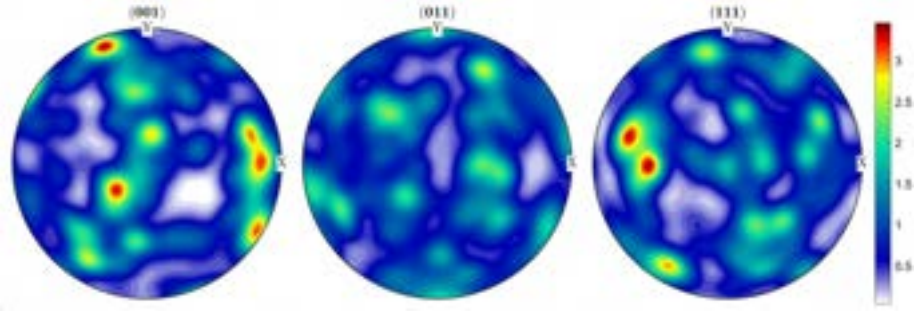

(b)

Figure 2.6: (a) Visualization of synthetic microstructure generated using DREAM.3D (b) Pole figures.

Fig. 2.7 depicts the comparison of the stress-strain curves between PRISMS-CPFE

and the result from Qidwai et al. [3]. PRISMS-CPFE model is able to capture the stress-strain curve of the Ti alloy polycrystal. Fig. 2.8(a) and Fig. 2.8(b) depict the variation of the equivalent stress and strain fields, respectively, using Paraview.

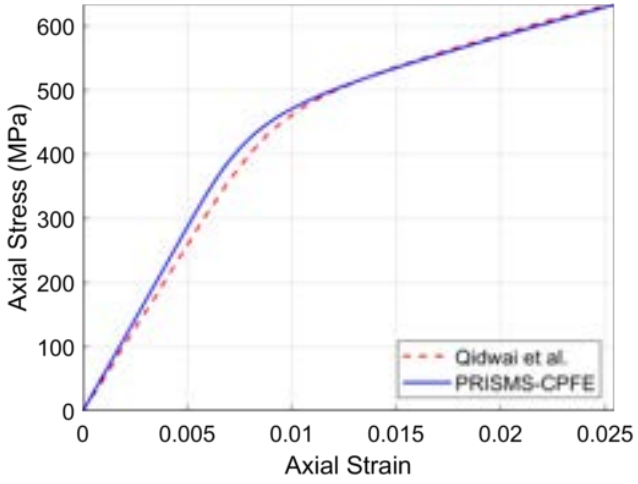

Figure 2.7: Stress-strain curve comparison between PRISMS-CPFE and Qidwai et al. [3].

2.7.3. Example III : Cyclic deformation of Al 7075-T6 polycrystal

We consider cyclic deformation of a 90 x 90 x 90 Al 7075-T6 polycrystal cube microstructure instantiated using DREAM.3D containing approximately 7500 grains with orientations sampled from random crystallographic texture. The polycrystal cube was subject to three fully reversed uniaxial straining cycles with strain amplitude of 0.7% under periodic constraints. The constitutive material model for this exercise includes the Ohno-Wang backstress model to capture kinematic hardening, without any isotropic hardening. The cubic crystal elastic constants of $C_{11} = 107.3$ GPa, $C_{12} = 60.9$ GPa, and $C_{44} = 28.3$ GPa were used. A reference shearing rate

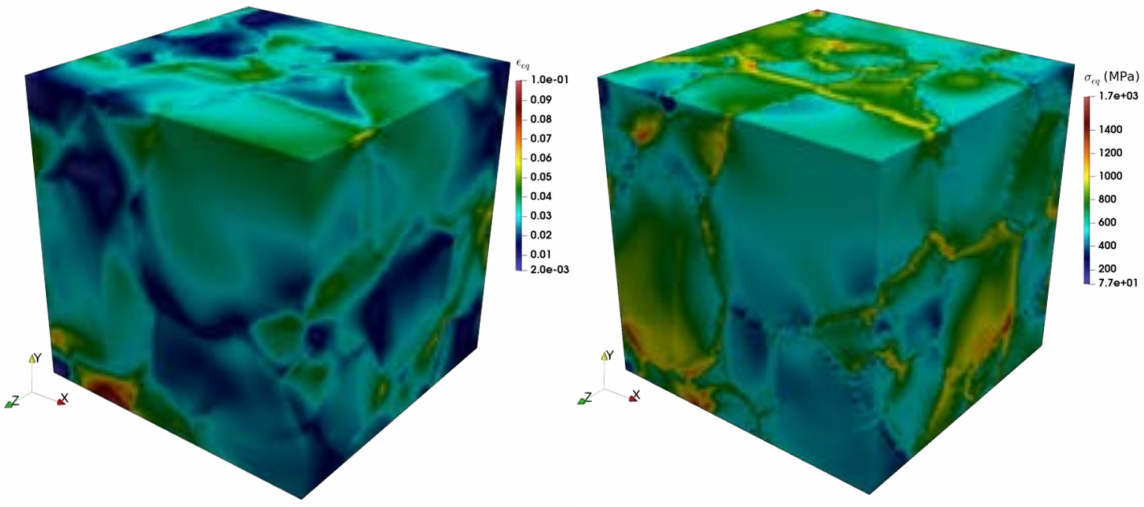

(a) (b)

Figure 2.8: (a) von Mises equivalent stress field in deformed microstructure, (b) von Mises equivalent strain field in deformed microstructure.

of 0.001 s^{-1} and strain-rate sensitivity exponent of $m = 75$ are used for the simulations. The crystal plasticity constitutive parameters of Al 7075-T6 alloy are presented in Table 2.3. The results obtained from PRISMS-CPFE are compared against an identical simulation setup(microstructure, boundary conditions, etc.) using the rate-dependent constitutive model implemented in ABAQUS [7]. There is excellent match between the PRISMS-CPFE and ABAQUS implementations for the cyclic deformation of the Al 7075-T6 microstructure.

m	s_0^α (MPa)	h_1 (MPa)	r_1	h_2 (MPa)	r_2	m_1, m_2
75	35	2 x 10^6	2 x 10^4	1.35 x 10^5	142	70

Table 2.3: Crystal plasticity constitutive model parameters for Al 7075-T6 [7]

Fig. 2.9a depicts the synthetic microstructure used for simulations and Fig. 2.9b

visualizes the pole figures for the sample. Fig. 2.10 depicts the stress-strain curve comparison between ABAQUS and PRISMS-CPFE.

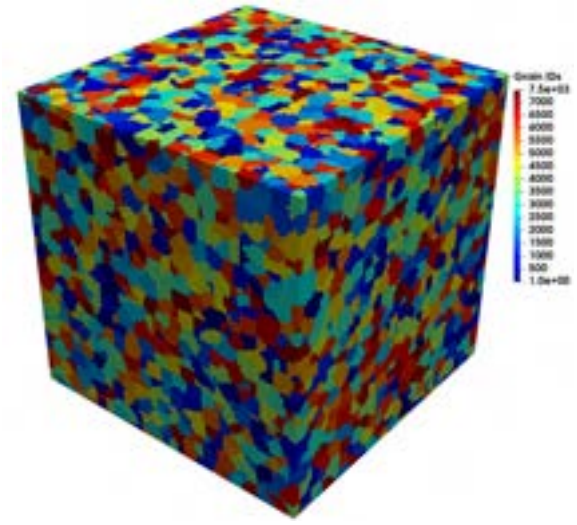

(a)

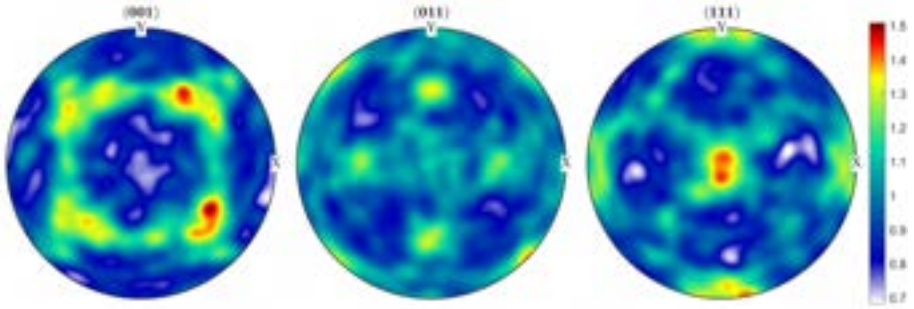

(b)

Figure 2.9: (a) Visualization of synthetic microstructure generated using DREAM.3D (b) Pole figures corresponding to the microstructural cube.

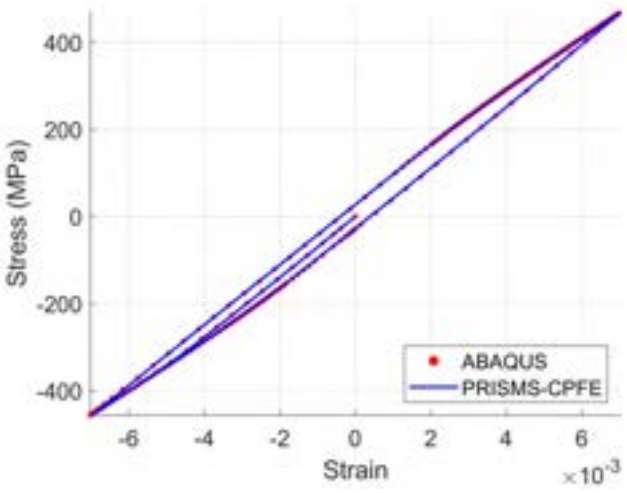

Figure 2.10: Cyclic stress-strain curve comparison between ABAQUS and PRISMS-CPFE.

CHAPTER III

Micro-Hall-Petch Parameters for Basal Slip

In this chapter, we detail the integration of theory and computation with experiments to obtain estimates of the micro-Hall-Petch parameters corresponding to basal slip for different GBs for Mg-4Al alloy system. Subsequently, considering a dependence of the micro-Hall-Petch parameters on two GB metrics via an empirical power law, we compute the micro-Hall-Petch multiplier and exponent for basal slip. These coefficients characterize the dependence of the size-dependent contribution of the slip resistance on the GB, and are the important material properties. We start by describing the continuum dislocation pile-up theory in 1D to model the slip band blocked by a GB, as a continuous distribution of dislocations, which furnishes a closed-form expression for the stress ahead of the pile-up. This expression is fit to HR-EBSD measurements of the pile-up from which the micro-Hall-Petch parameters for basal slip are estimated for different GBs. We then outline the calibration procedure to obtain constitutive model parameters which are then used to simulate neighborhoods of GBs of interest to obtain the incoming slip system(corresponding

to the slip band) and he potential outgoing slip system in the adjacent grain blocking the slip band. The micro-Hall-Petch parameters are then related to two GB metrics motivated from slip transmission studies in order to identify the micro-Hall-Petch coefficients - the micro-Hall-Petch multiplier and the micro-Hall-Petch exponent for basal slip[132, 133].

3.1. Continuum Dislocation Pile-up Model

The following method to construct a model for a slip band based on the theory of continuous distribution of dislocations is adapted from Hirth and Lothe[134]. Here the slip band is treated as a distribution of dislocations in a one-dimensional domain with the ends of the domain representing GBs. The slip band is idealized to the interval $[-L/2, L/2]$, where the boundaries of the domain represent GBs acting as obstacles to dislocation slip transmission (Fig. 3.1). For any $x \in [-L/2, L/2]$ a dislocation density field $\rho(x)$ is prescribed, so that the total number of dislocations in a differential element δx is $\delta n\,(x) = \rho(x)\delta x$. A continuous density field in one-dimension is a continuum representation of straight, infinite dislocations of positive or negative type, for a given Burgers vector. The sign of the density field refers to the group of dislocations of the corresponding sign. An applied stress field exerts a configurational force on the dislocation of the Peach-Koehler type. Additionally, there is a long-range stress field due to dislocations in the medium (by virtue of their presence), which imposes a configurational force on a dislocation present anywhere else in the medium. Any net force acting on the dislocations drives the system to an equilibrium state which is characterized by zero net configurational force. Because

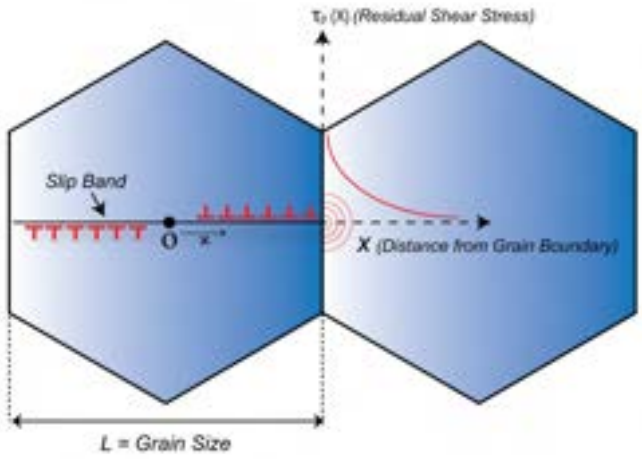

Figure 3.1: Continuum model of dislocation pile-up at a GB. Dislocations are smeared out to a continuous density field and the red curve in the adjacent grain denotes the pile-up stress due to a pile-up of dislocations at the boundary.

the expressions for the stress fields of dislocations are derived based on linear elasticity, the net configurational force is simply a sum of individual force terms. The equilibrium condition is then expressed mathematically as:

$$\tau(x)b + \frac{\mu b^2}{2\pi\kappa} \int_{-L/2}^{L/2} \frac{\rho(x')}{x - x'} dx' = 0 \tag{3.1}$$

where $\tau(x)$ denotes the applied shear stress resolved along the slip system, L is the grain size, μ the shear modulus for an isotropic elastic material, b the Burgers vector strength, and $\kappa = 1$ (for screw dislocations) or $\kappa = 1 - \upsilon$ (for edge dislocations). It is noted that Mg-4Al is close-to elastically isotropic so that the Eqn. 3.1 is a reasonable approximation. For polynomial forms of $\tau(x)$ the equilibrium dislocation

density distribution and pile-up stress can be analytically found. The special case of a spatially constant resolved shear stress $\tau(x) = \tau$ is considered in this study, for which the equilibrium dislocation distribution takes the form

$$\rho(x) = \frac{2\kappa\tau}{\mu b}\frac{x}{\sqrt{\left(\frac{L}{2}\right)^2 - x^2}} + \frac{CL}{2\sqrt{\left(\frac{L}{2}\right)^2 - x^2}} \tag{3.2}$$

Where C is a constant appearing due to the homogeneous solution of the integral equation. This constant can be related to the net Burgers vector considering all the dislocations appearing in the slip band, which for simplicity is assumed to be zero. In other words, there is an equal number of dislocations of both positive and negative type. Accordingly, the stress ahead of the pile-up (pileup-stress) due to the dislocation distribution alone takes the form

$$\begin{aligned}\tau_p(x) &= \frac{\mu b^2}{2\pi\kappa}\int_{-L/2}^{L/2}\frac{\rho(x')}{x - x'}dx' \;;\; x > L/2 \\ &= \tau\left[\frac{X + \frac{L}{2}}{\sqrt{\left(X + \frac{L}{2}\right)^2 - \left(\frac{L}{2}\right)^2}} - 1\right]\end{aligned} \tag{3.3}$$

In comparison with experiments, it is noted that the theoretical prediction for the pileup-stress must not include the effect of the resolved stress, because the experiment measures the residual stress in the adjacent grain. This residual stress is considered to arise primarily from the development of a dislocation distribution in the slip band reminiscent of a dislocation pile-up. The sole purpose of the resolved shear stress is to generate this dislocation distribution which develops irreversibly, and hence,

retains the functional form even after removal of the resolved shear stress. In other words, the generated dislocation distribution is assumed to change negligibly so that the form of the pileup stress is not affected significantly. These simplifications are debatable but in the interest of obtaining a simple analytical form, are suggested to be an appropriate starting point. To purport a particular form of the resolved shear stress, two assumptions are made :

1. The resolved shear stress on the slip system equals the initial slip system resistance, which arises by neglecting the phenomenon of work hardening on that slip system. In other words, the applied shear stress required to equilibrate a dislocation distribution is identical to the initial slip system resistance which must be overcome to produce the slip band and accommodate majority of the applied deformation.

2. It is assumed that classical Hall-Petch relationship may be extended to the slip system level, formerly termed as "micro-Hall-Petch" relation[135, 136]. It is one way of quantifying the contribution of the grain size to the initial slip resistance . Additionally, because the pile-up model doesn't take into account the GB character, the GB effect is subsumed in the estimates of the micro-Hall-Petch coefficients. Accordingly, the slip system resistance is expressed in the following form:

$$\tau^{\alpha} = \tau_0^{\alpha} + \frac{k_{\mu}^{\alpha}}{\sqrt{d^{\alpha}}} \tag{3.4}$$

where τ_0^{α} is the size-independent component of the slip system resistance, k_{μ}^{α}

is the micro-Hall-Petch parameter associated with the slip system α signifying the strength of the size effect, and d^α is the slip system-level grain size, which in this case represents the length of the slip band across an entire grain, L or L^α to be more precise. The term $k_\mu^\alpha/\sqrt{d^\alpha}$ is the size-dependent contribution to the slip system resistance.

In the context of the current experiment, L^α corresponds to the length of the slip trace measured along the direction perpendicular to the dislocation(infinite edge or screw) line and slip plane normal of the slip system from one GB to the opposite. Substituting Eqn. 3.4 in Eqn. 3.3 yields:

$$\tau_p^\alpha(x) = \left(\tau_0^\alpha + \frac{k_\mu^\alpha}{\sqrt{L^\alpha}}\right)\left[\frac{X + \frac{L^\alpha}{2}}{\sqrt{\left(X + \frac{L^\alpha}{2}\right)^2 - \left(\frac{L^\alpha}{2}\right)^2}} - 1\right] \tag{3.5}$$

The micro-Hall-Petch coefficients were computed for nine different GB types by performing a linear least-squares fit of the pile-up stress expression in Eqn. 3.5, to the experimentally measured stress field ahead of the pile-up (Fig. 3.2). The value of the size-independent component of the slip resistance τ_0^α used for the fitting was computed by incorporating the effect of solid solution strengthening due to 4 wt. % Al [137] resulting in $\tau_0^\alpha = 4.34$ MPa. It must be noted that using a one-dimensional continuum dislocation pile-up model is an oversimplification of the actual physics, which is much more complicated. However, in the interest of drawing a simple analogy to a blocked slip band and obtaining first-order analytical expressions, we have resorted to the aforementioned model. Table. 3.1 reports the micro-Hall-Petch parameters corresponding to basal slip estimated for the nine GBs studied, where these

GBs block slip bands associated with the basal slip system.

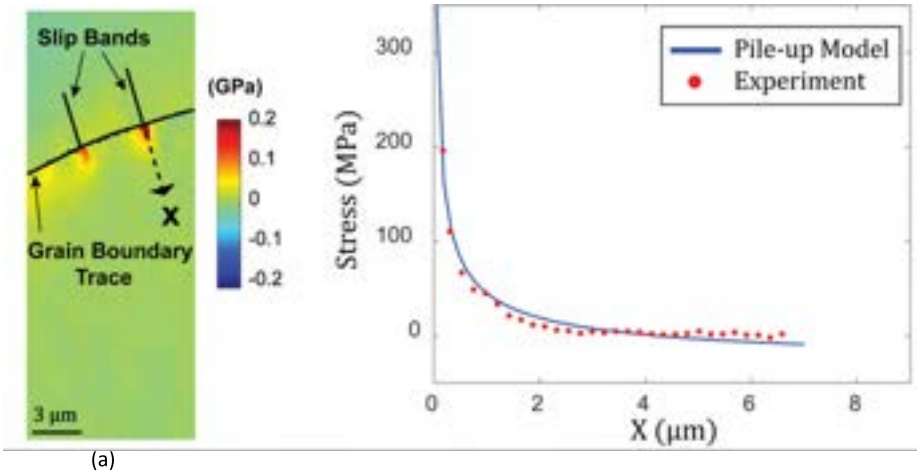

Figure 3.2: (a) HR-EBSD map of resolved shear stress onto the active slip system in the upper grain. The stress concentration ahead of pile up at GB can be observed. The solid lines represent the position of the slip bands, and the dashed line with an arrowhead indicates the direction along which the pile-up stress profile was extracted, (b) The resolved shear stress profile ahead of a slip band blocked by a GB with comparison to the pile-up stress expression from the continuum dislocation pile-up model to calculate the micro-Hall-Petch parameters of each GB.

GB ID	Slip system-level grain size (μm)	k_{μ}^{basal} $\left(\text{MPa } \mu m^{1/2}\right)$
1	48.0	164.0 ± 20.0
2	55.0	91.0 ± 10.0
3	27.0	149.0 ± 20.0
4	8.0	172.0 ± 20.0
5	65.0	54.0 ± 10.0
6	21.0	108.0 ± 10.0
7	50.0	70.0 ± 10.0
8	60.0	143.0 ± 10.0
9	48.0	184.0 ± 20.0

Table 3.1: micro-Hall-Petch parameters for basal slip for different GBs.

The next step involves parametrizing the computed the micro-Hall-Petch parameters with metrics computed from information about the GBs and slip systems in the grains sharing the GB.

3.2. Crystal Plasticity Simulations

To parametrize the micro-Hall-Petch parameter values for different GBs, relevant information about the slip systems in the grains sharing the boundary is necessary. The information of the incoming slip system in the grain containing the slip band is available by analyzing the trace of the slip band. Since we do not know apriori which slip system will be chosen as the one to transmit slip in the neighboring grain, we setup crystal plasticity simulations of the GB neighborhoods to obtain

this information. We now cover details regarding calibration of the crystal plasticity constitutive model and simulations of GB neighborhoods.

3.2.1. Constitutive Model Calibration

For the calibration step, the polycrystal idealized as an 8 x 8 x 8 voxelated RVE was constructed, where each voxel was assigned a distinct orientation. Orientations were sampled from an EBSD map of a microstructure(Fig. 3.3a) corresponding to as-extruded texture(Fig. 3.3b). Fig. 3.5a depicts the pole figures associated with the 512 distinct orientations sampled from the underlying texture. This microstructure was subject to simple tension along the y-direction(coinciding with the extrusion direction or 'ED') up to 3.5% strain(Fig. 3.4). Fig. 3.5b depicts the comparison of stress-strain response from the simulation to the experiment at the end of calibration. The list of constitutive model parameters post-calibration is included in Table. 3.2. In the hardening law, the latent hardening coefficient was set to $q = 1.0$, while the flow rule parameters were set as $\dot{\gamma}_0 = 0.001\text{s}^{-1}$ and $m = 34$.

Deformation mode	s_0^α(MPa)	h_0^α(MPa)	s_s^α(MPa)	a^α
Basal	6.0	76.0	120.0	1.0
Prismatic	78.0	163.0	150.0	1.0
Pyramidal	140.0	187.0	150.0	1.0
Twin	13.0	116.0	100.0	1.0

Table 3.2: Calibrated crystal plasticity constitutive model parameters.

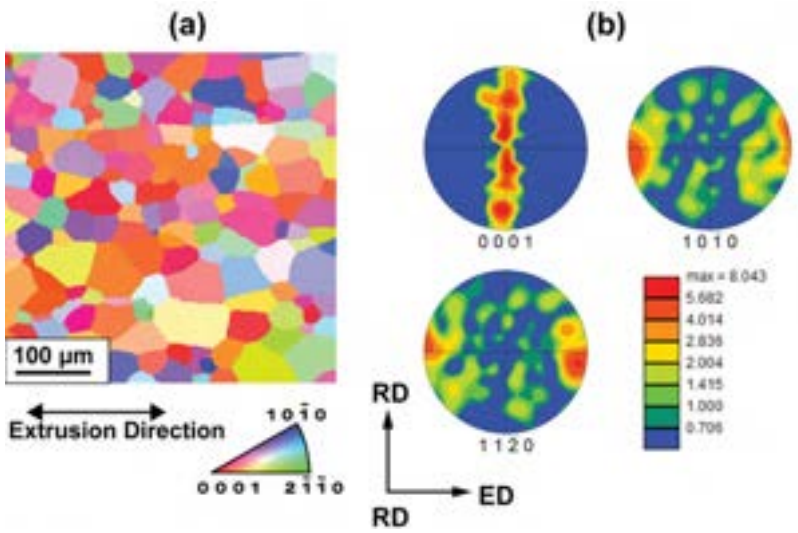

Figure 3.3: (a) Microstructure section used to inform input texture for simulations, and (b) experimental pole figures of extruded Mg-4Al (wt.%) used in this study. The microstructure contains equiaxed grains with an average grain diameter of 50 μm. RD: Radial Direction; ED: Extrusion Direction.

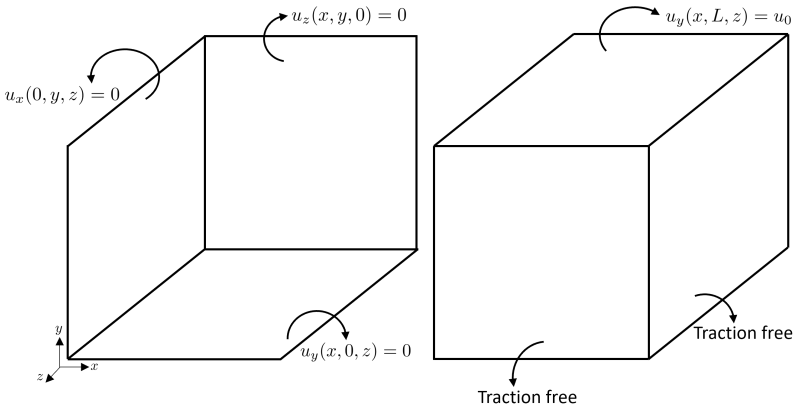

Figure 3.4: Simple tension boundary conditions that the microstructures are subject to. u_0 denotes the displacement enforced corresponding to 3.5 % strain, i.e., $u_0 = 0.035L$.

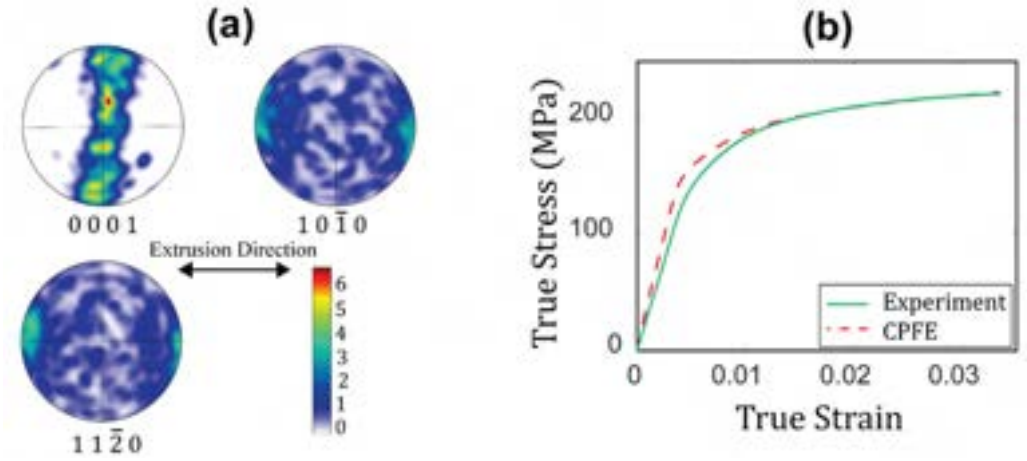

Figure 3.5: (a) Pole figures of the polycrystalline RVE represented as an 8 x 8 x 8 voxelated grid with a distinct orientation for every voxel, and (b) Comparison of simulated stress-strain response with experiment resulting in the calibrated parameters in Table. 3.2.

3.2.2. Grain Boundary Neighborhood Simulations

To construct GB descriptors through which a relationship can be drawn to the micro-Hall-Petch parameter, some information about the slip activity in the grains is necessary. By virtue of capturing the resolved stress ahead of the blocked slip band, the slip system in the adjacent grain which could potentially accommodate slip transmission, is not known. Additionally, even in the grain containing the slip band, all we know is that the band corresponds to a basal slip system. Since the three basal systems share the same slip plane and the slip band is simply the trace of the slip plane, the slip direction associated with the slip band is not know. We refer to the slip system associated with the slip band as the incoming slip system. For this purpose, crystal plasticity simulations are employed.

CPFE simulations were performed on the nine different microstructural neighbor-

hoods of each GB of interest, consisting of the grains sharing that boundary and a few other surrounding grains. The aim is to find the active slip system associated with the observed slip band and predict the outgoing slip system of the least resistance. Since EBSD maps were available for just one section (sample surface), three-dimensionality of the problem was preserved by extruding the 2D section to obtain a one element slice of unit thickness($1\mu m$) resulting in a uniform grid of hexahedral elements. Additionally, to overcome the lack of knowledge of the state of stress or displacements at the boundary of those neighborhoods, boundary conditions(Fig. 3.7) were enforced as follows:

1. The x and y components of displacements were enforced on the lateral boundaries based on a constant velocity gradient reminiscent of uniaxial tension along direction y.

$$\boldsymbol{L} = \dot{\boldsymbol{F}}\boldsymbol{F}^{-1} = \begin{bmatrix} -0.5 & 0 & 0 \\ 0 & 1 & 0 \\ 0 & 0 & -0.5 \end{bmatrix} \; ; \; \boldsymbol{F}(0) = \boldsymbol{I}$$

$$u_x = F_{11}x + F_{12}y + F_{13}z \; , \; u_y = F_{21}x + F_{22}y + F_{23}z \tag{3.6}$$

   where $\boldsymbol{L}$ is the velocity gradient, $\boldsymbol{F}$ is the deformation gradient, t is the time, and u_x and u_y are the x and y components of the displacement, respectively.

2. The $x-y$ face at $z=0$ is constrained from displacing along the z-direction while the opposite face is treated as a traction-free surface.

Slices of the simulated microstructure were deformed to a strain of approximately

2% where the grains of interest show some slip activity in order to identify the most active system, which is computed as follows. This was performed for GB neighborhoods associated with the nine GBs considered for the micro-Hall-Petch parameter computation. Fig. 3.6a depicts an experimental SEM image of a sample microstructural section while Fig. 3.6b depicts the corresponding microstructural section used for simulations. Fig. 3.6c visualizes the grains sharing the GB and the trace of the slip band in one grain blocked by the adjacent grain. For each element of the FE mesh, the accumulated slip for each slip system was computed based on the information available at the integration points. Fig. 3.8 depicts the accumulated slip associated with the three basal slip systems. We are particularly interested in the incoming slip system(corresponding to the slip band trace) and potential outgoing slip system to be able to construct different metrics to parametrize the micro-Hall-Petch parameter. For the grain containing the slip band, slip traces only convey information about the slip plane, but no information is known about the slip direction. That is where the CPFE simulation results dictate the choice of the most active basal slip system since all three basal slip systems share the same slip plane but possess different slip directions. For the grain blocking the slip band (the adjacent grain) the most active slip system (potentially outgoing slip system) is interpreted as the one offering the least resistance to the slip band so that when slip transmission ensues, it occurs with the highest probability on this most active slip system. For this purpose, the region at the GB containing the slip band in the real microstructure was identified by its corresponding element in the uniform grid. Then based on the most active slip system ID of the elements in the neighborhood

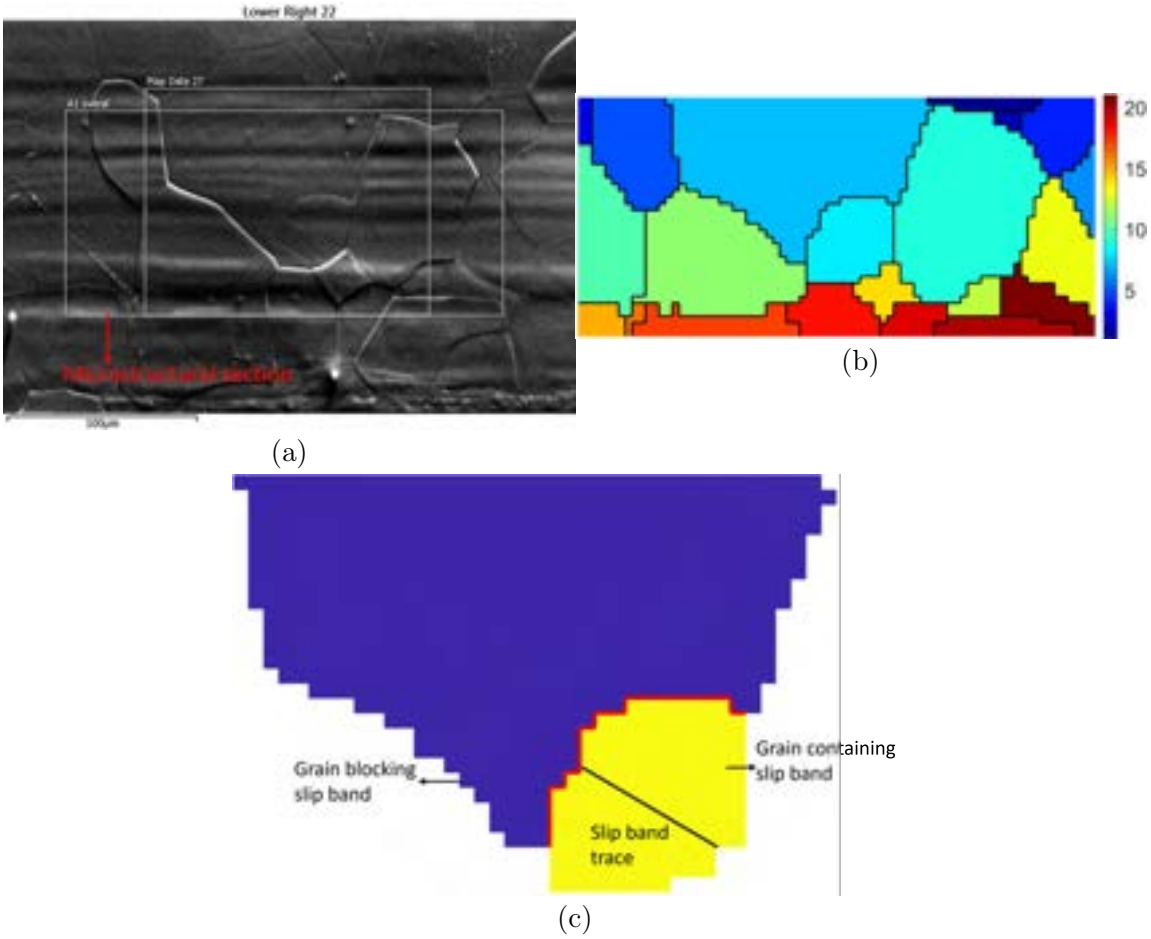

Figure 3.6: (a) Microstructure section from experimental SEM image, (b) Microstructural section used for simulation with grain IDs of individual grains, and (c)Illustration of the grains sharing the GB (GB 1 in Table. 3.4) of interest along with the trace of the slip band in one grain blocked by the adjacent grain.

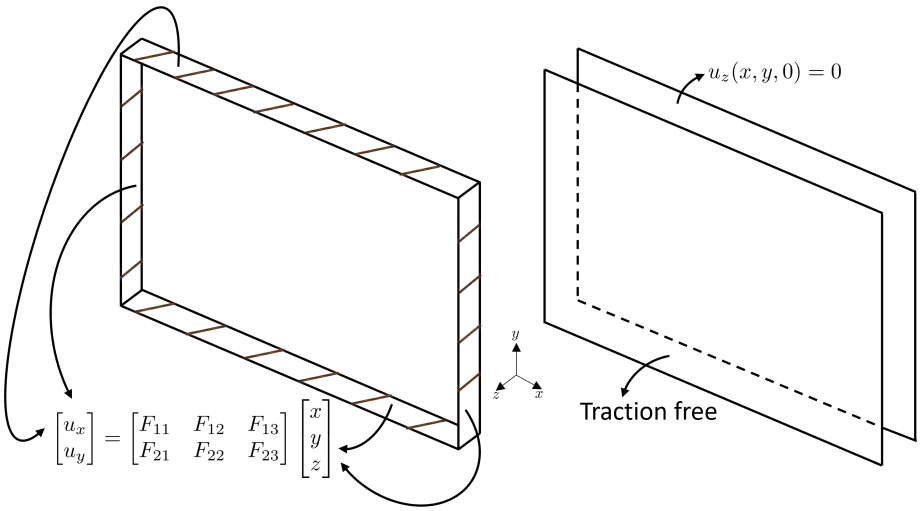

Figure 3.7: Boundary conditions applied to the microstructure section corresponding to the GB neighborhood for the GB of interest.

of this GB element the potential outgoing slip system is identified. This slip system is interpreted as the one offering the least resistance to the blocked slip band.

Figs. 3.8a-3.8c depicts the accumulated slip on the three basal slip systems. The accumulated slip on just basal systems is depicted since their activity is significant compared to the activity of prismatic slip systems. Fig. 3.8d visualizes a map of the most active slip system ID throughout the entire microstructural section while Fig. 3.8e depicts it for the grains sharing the GB of interest. Table. 3.3 includes information about which slip system associated with a particular slip system ID. It is evident that basal slip dominates as the most active slip system throughout the entire microstructural section. Then for this particular GB case, the most active slip system in the grain containing the slip band has ID 3, i.e., $(0001)[1\bar{2}10]$ while the most active slip system in the adjacent grain has ID 1, i.e., $(0001)[11\bar{2}0]$.

Slip system ID	Slip plane	Slip direction
1	(0001)	$[11\bar{2}0]$
2	(0001)	$[\bar{2}110]$
3	(0001)	$[1\bar{2}10]$
4	$(10\bar{1}0)$	$[1\bar{2}10]$
5	$(01\bar{1}0)$	$[\bar{2}110]$
6	$(\bar{1}100)$	$[11\bar{2}0]$

Table 3.3: Calibrated crystal plasticity constitutive model parameters

Performing the same procedure for the eight remaining GB cases yields the incoming slip system in the grain containing the slip band, and the potential outgoing slip system in the adjacent grain blocking the slip band. Figs. 3.9-3.16 depict the microstructural sections for the remaining GBs, each depicting the microstructural section used in simulations, the grains sharing the GB, the accumulated slip on the three basal slip systems and the most active slip system ID in the grains sharing the GB. Table. 3.4 lists the incoming and potential outgoing slip system for each case.

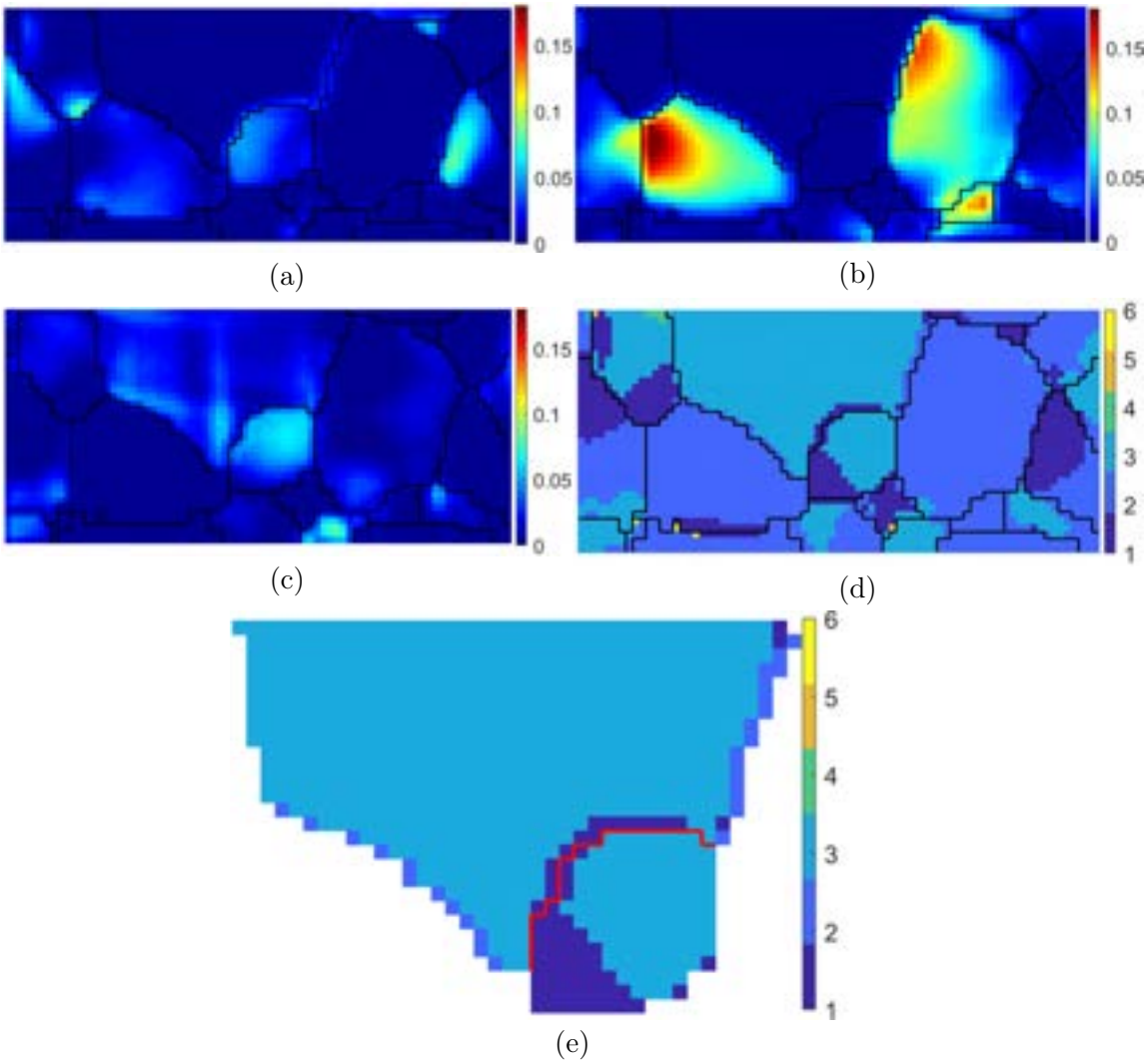

Figure 3.8: (a)Accumulated slip for basal slip system 1, (b)Accumulated slip for basal slip system 2, (c)Accumulated slip for basal slip system 3, (d) Most active slip system ID map for microstructural section, and (e) Most active slip system ID map for grains sharing GB of interest.

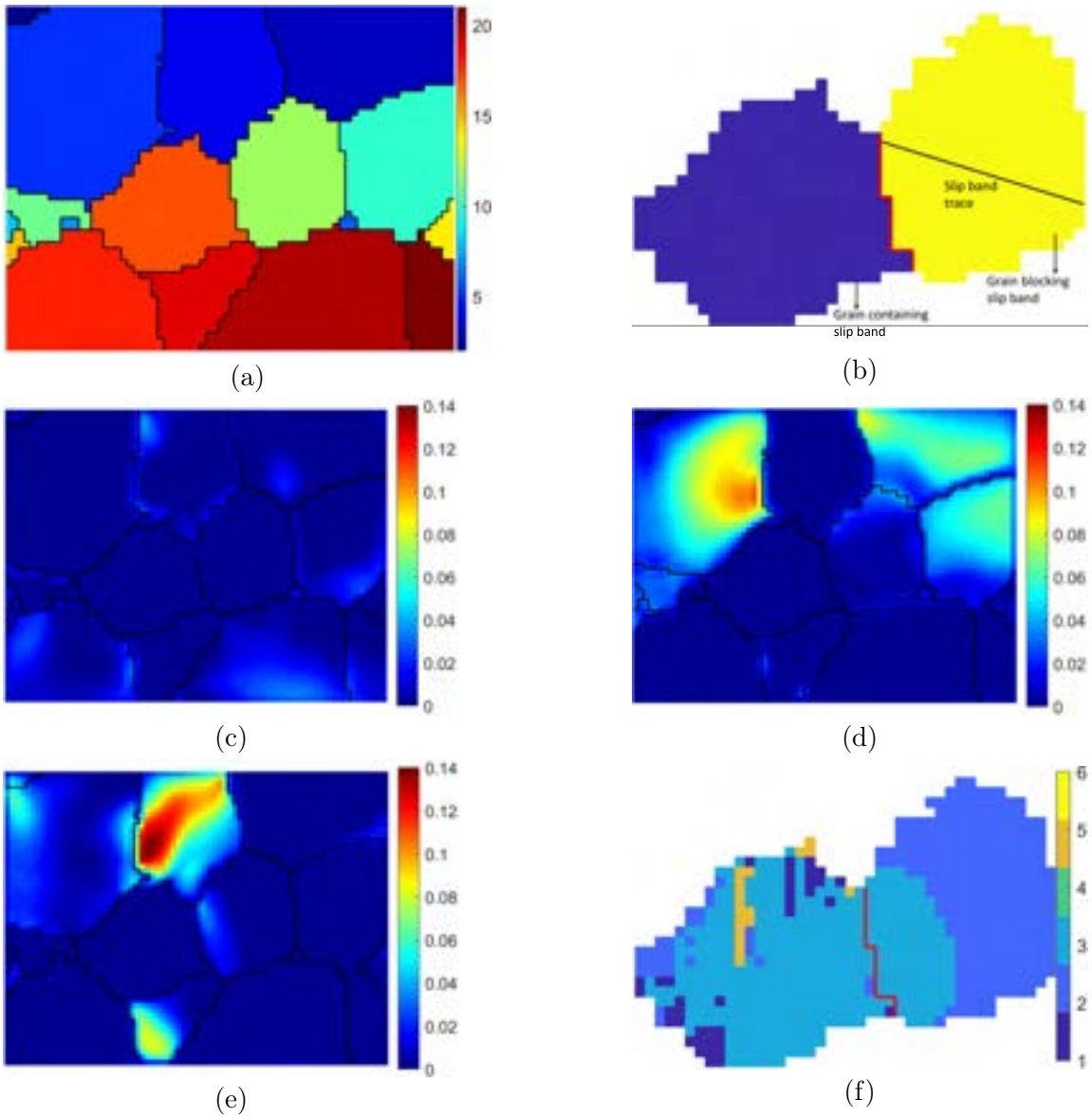

Figure 3.9: (a) Microstructure section corresponding to the GB neighborhood for GB 2 with grain IDs, (b) Illustration of the grains sharing the GB of interest along with the trace of the slip band in one grain blocked by the adjacent grain, (c) Accumulated slip for basal slip system 1, (d)Accumulated slip for basal slip system 2, (e) Accumulated slip for basal slip system 3, and (e) Most active slip system ID map for grains sharing GB of interest.

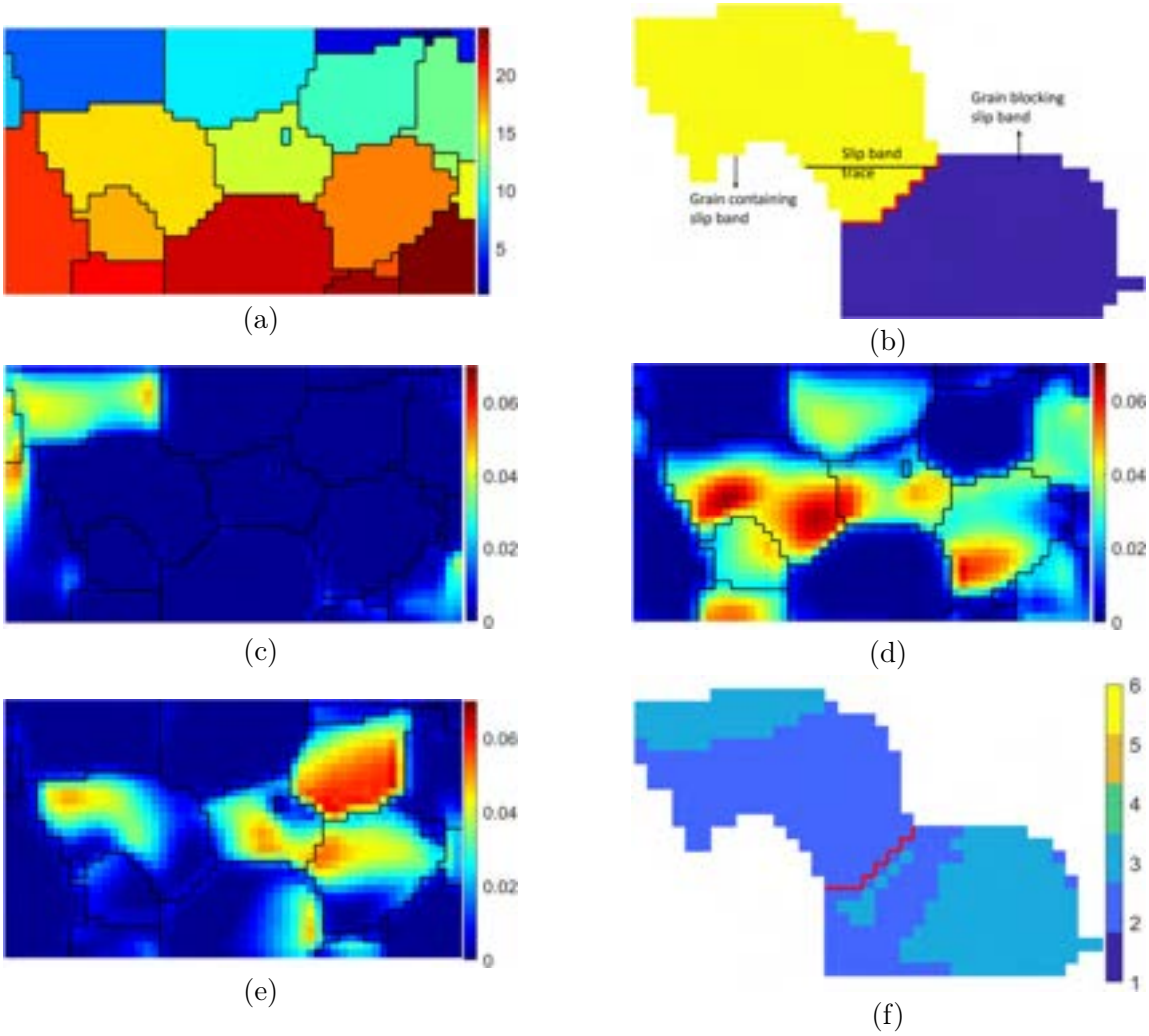

Figure 3.10: (a) Microstructure section corresponding to the GB neighborhood for GB 3 with grain IDs, (b) Illustration of the grains sharing the GB of interest along with the trace of the slip band in one grain blocked by the adjacent grain, (c) Accumulated slip for basal slip system 1, (d)Accumulated slip for basal slip system 2, (e) Accumulated slip for basal slip system 3, and (e) Most active slip system ID map for grains sharing GB of interest.

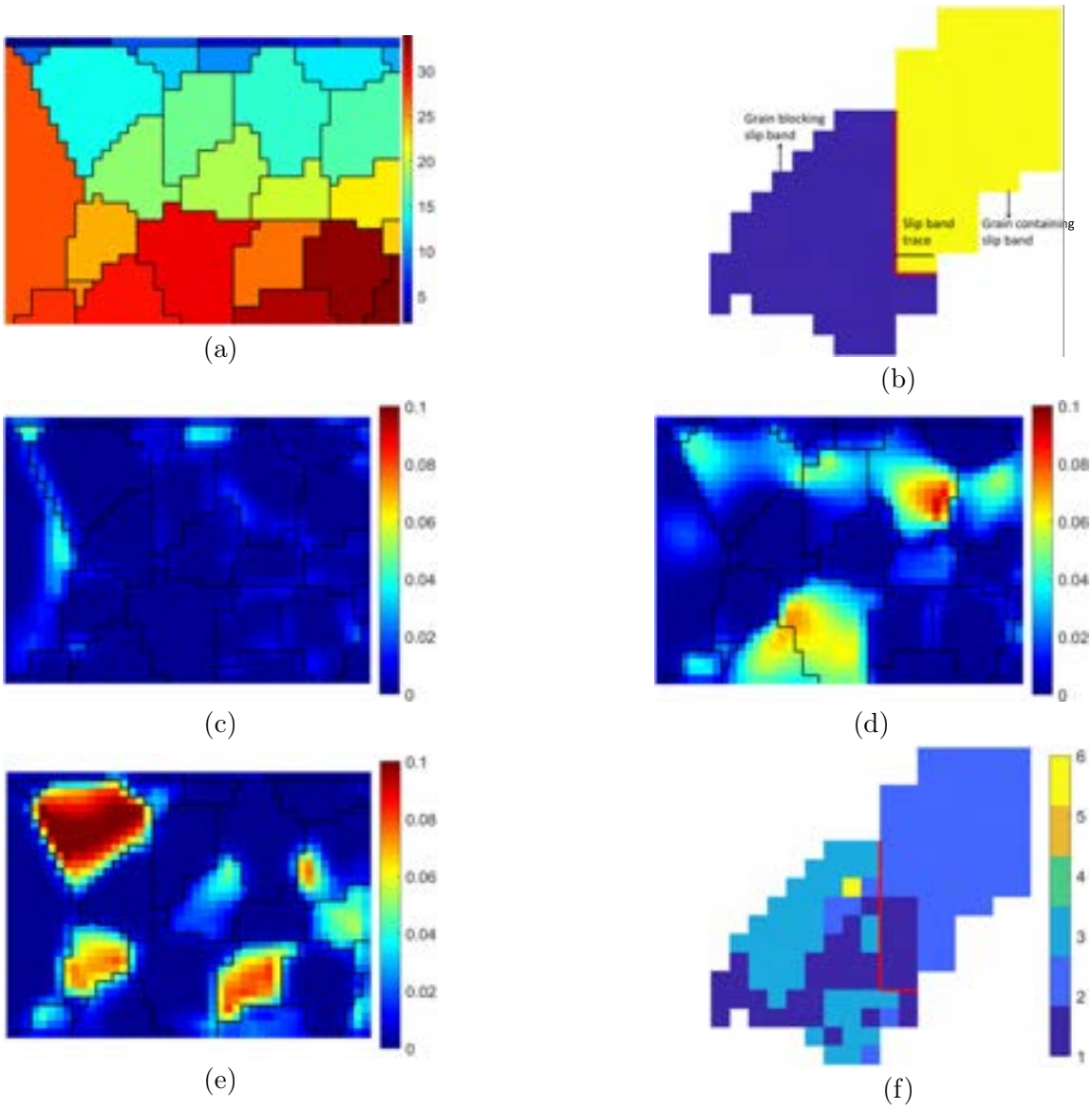

Figure 3.11: (a) Microstructure section corresponding to the GB neighborhood for GB 4 with grain IDs, (b) Illustration of the grains sharing the GB of interest along with the trace of the slip band in one grain blocked by the adjacent grain, (c) Accumulated slip for basal slip system 1, (d)Accumulated slip for basal slip system 2, (e) Accumulated slip for basal slip system 3, and (e) Most active slip system ID map for grains sharing GB of interest.

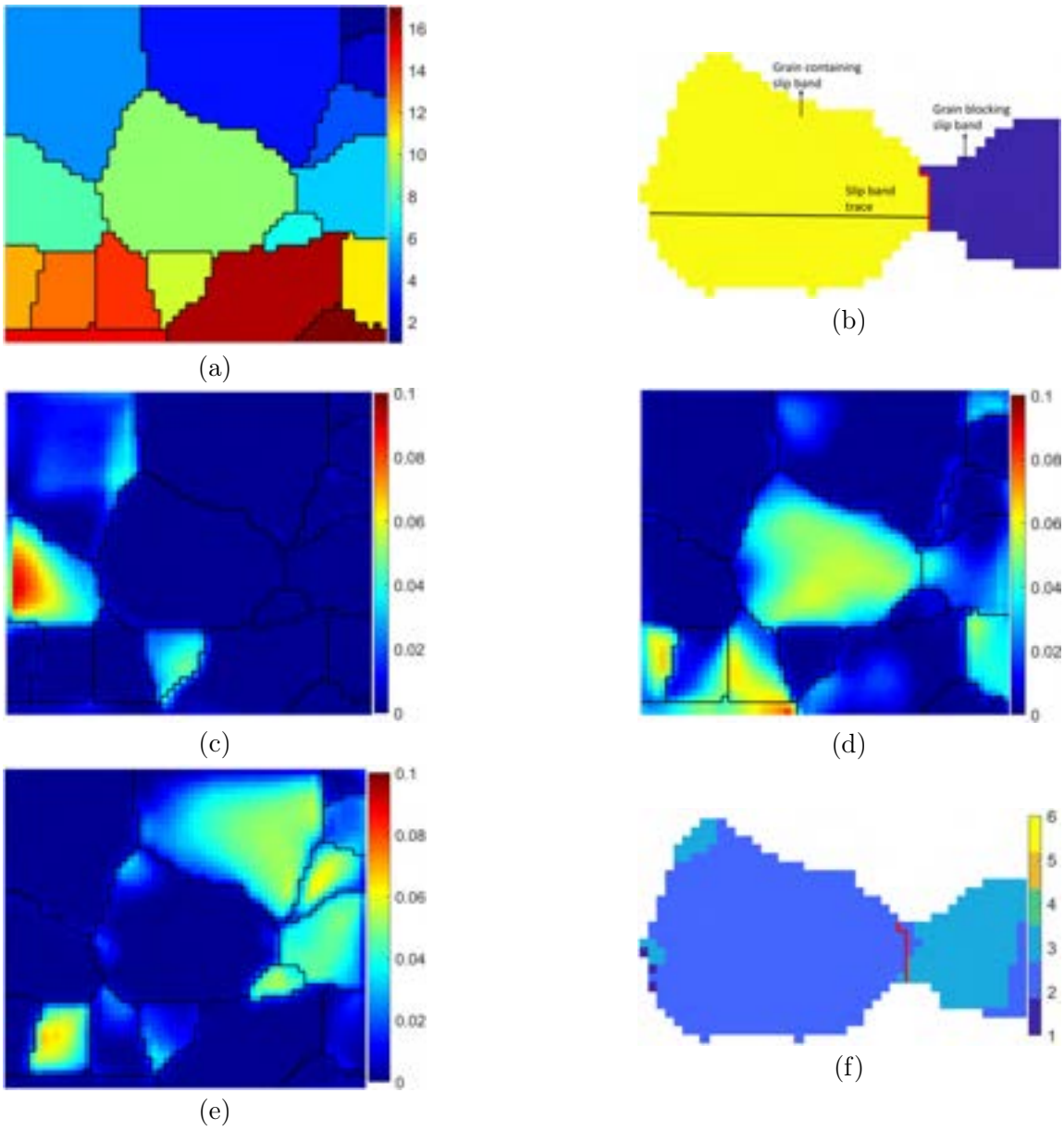

Figure 3.12: (a) Microstructure section corresponding to the GB neighborhood for GB 5 with grain IDs, (b) Illustration of the grains sharing the GB of interest along with the trace of the slip band in one grain blocked by the adjacent grain, (c) Accumulated slip for basal slip system 1, (d)Accumulated slip for basal slip system 2, (e) Accumulated slip for basal slip system 3, and (e) Most active slip system ID map for grains sharing GB of interest.

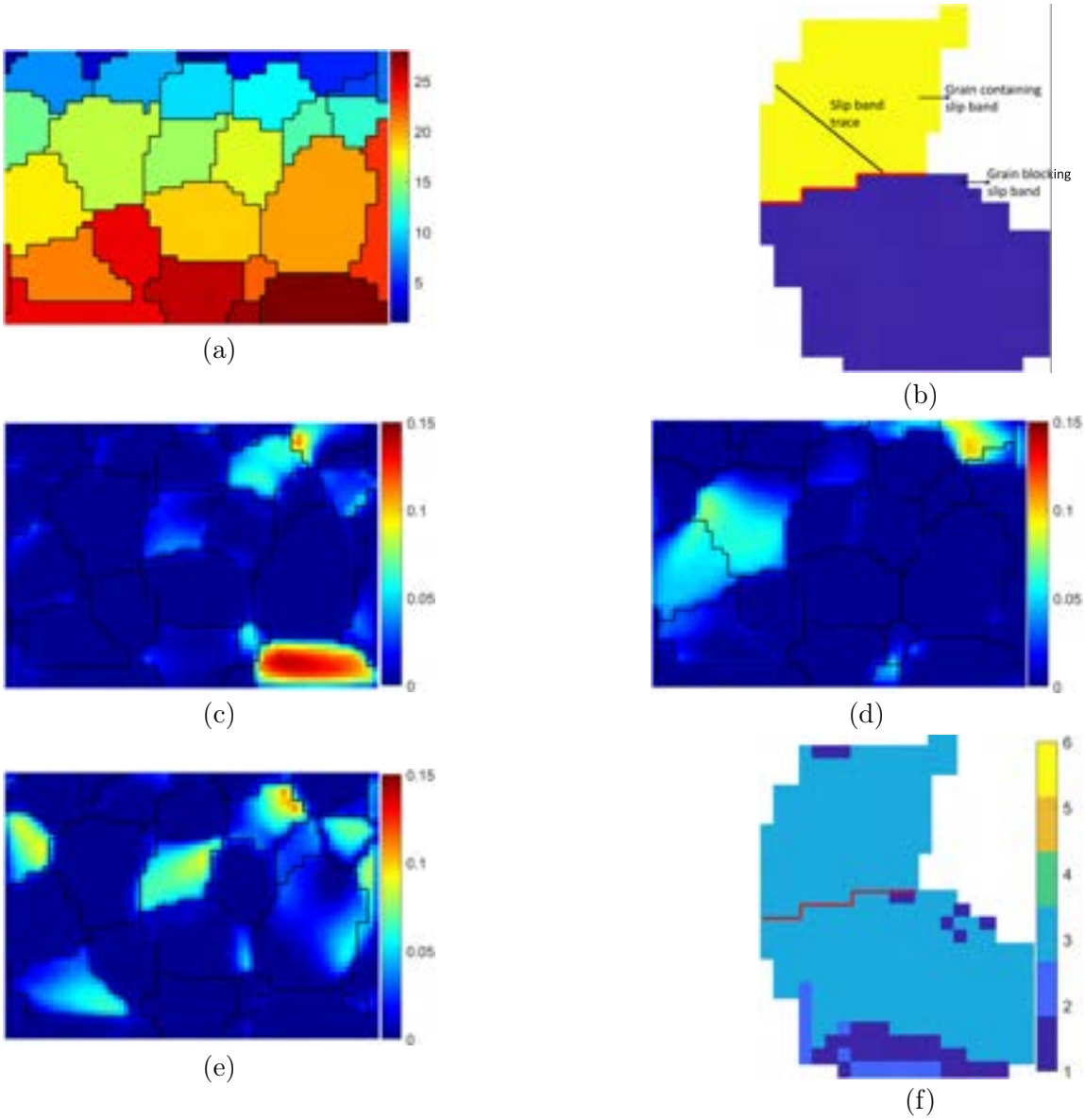

(a) (b) (c) (d) (e) (f)

Figure 3.13: (a) Microstructure section corresponding to the GB neighborhood for GB 6 with grain IDs, (b) Illustration of the grains sharing the GB of interest along with the trace of the slip band in one grain blocked by the adjacent grain, (c) Accumulated slip for basal slip system 1, (d)Accumulated slip for basal slip system 2, (e) Accumulated slip for basal slip system 3, and (e) Most active slip system ID map for grains sharing GB of interest.

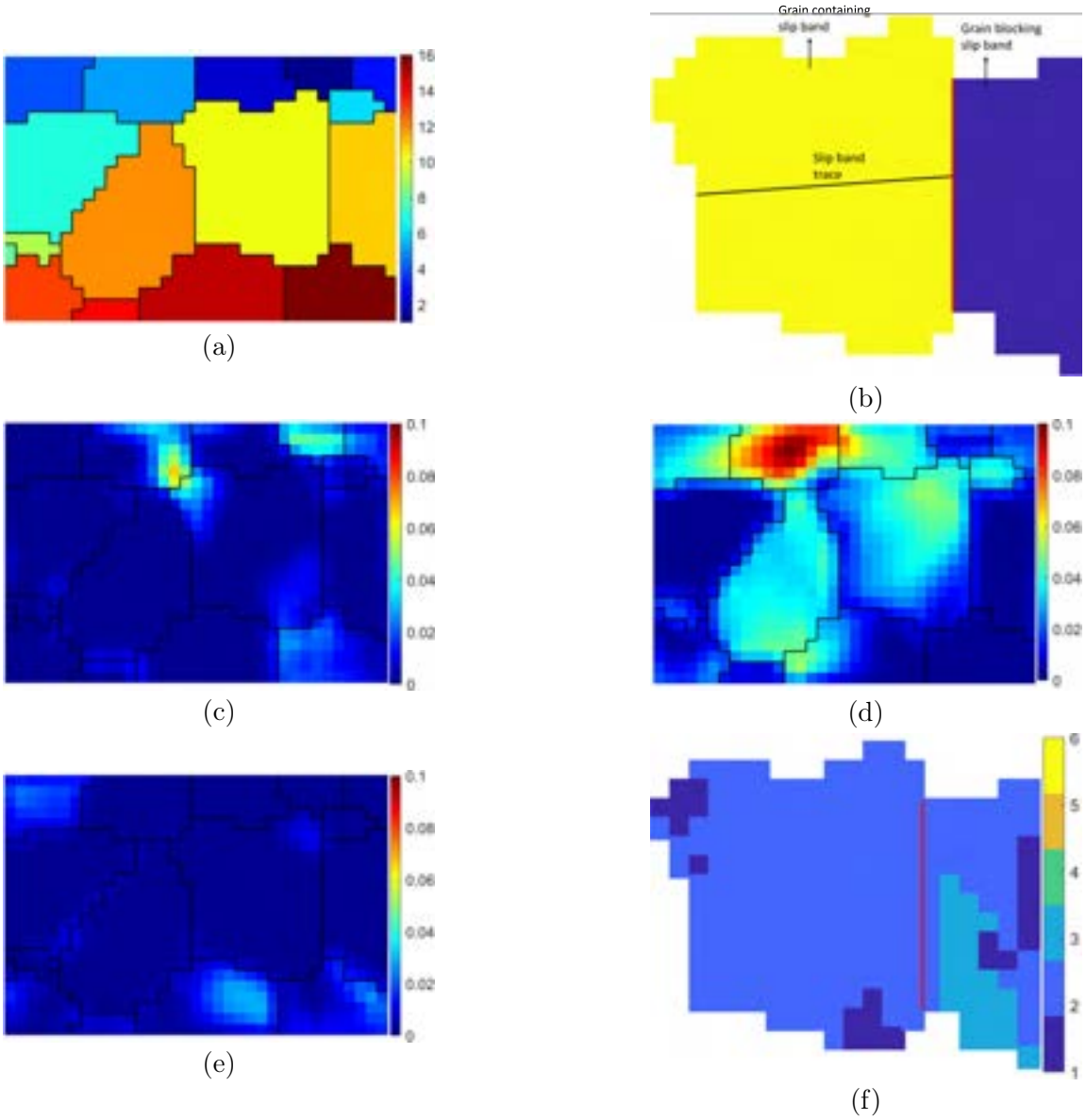

Figure 3.14: (a) Microstructure section corresponding to the GB neighborhood for GB 7 with grain IDs, (b) Illustration of the grains sharing the GB of interest along with the trace of the slip band in one grain blocked by the adjacent grain, (c) Accumulated slip for basal slip system 1, (d)Accumulated slip for basal slip system 2, (e) Accumulated slip for basal slip system 3, and (e) Most active slip system ID map for grains sharing GB of interest.

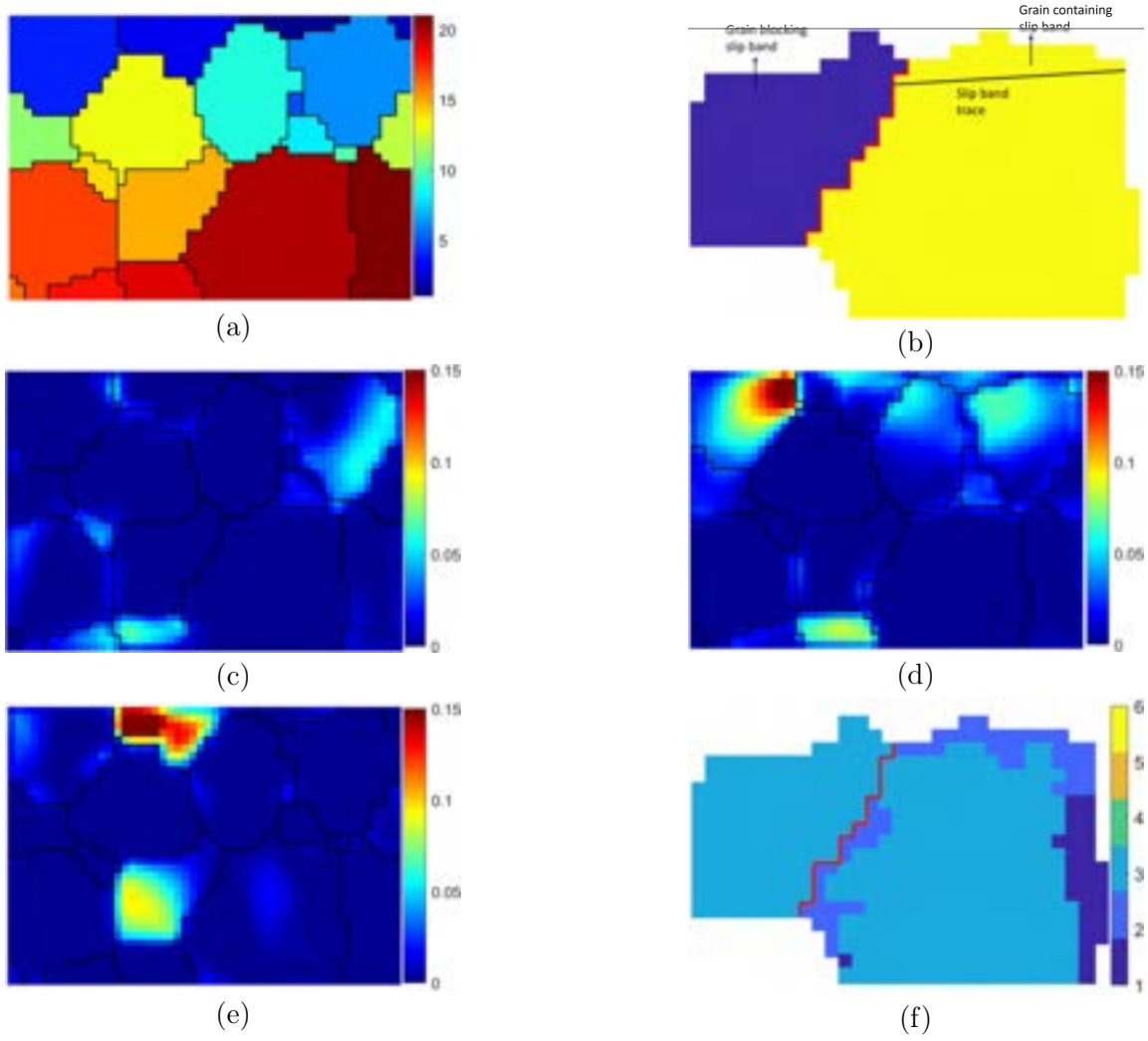

Figure 3.15: (a) Microstructure section corresponding to the GB neighborhood for GB 8 with grain IDs, (b) Illustration of the grains sharing the GB of interest along with the trace of the slip band in one grain blocked by the adjacent grain, (c) Accumulated slip for basal slip system 1, (d)Accumulated slip for basal slip system 2, (e) Accumulated slip for basal slip system 3, and (e) Most active slip system ID map for grains sharing GB of interest.

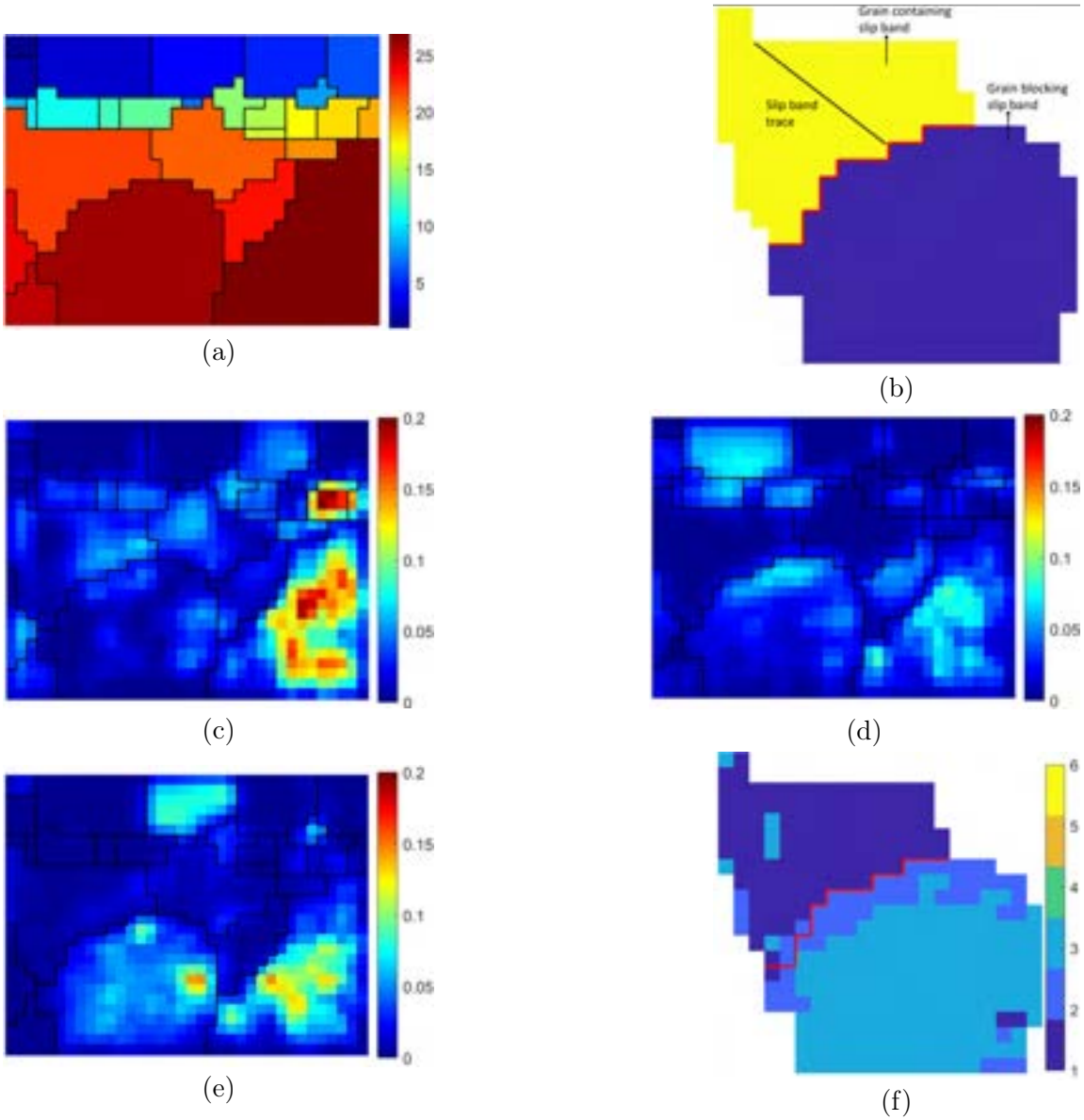

Figure 3.16: (a) Microstructure section corresponding to the GB neighborhood for GB 9 with grain IDs, (b) Illustration of the grains sharing the GB of interest along with the trace of the slip band in one grain blocked by the adjacent grain, (c) Accumulated slip for basal slip system 1, (d)Accumulated slip for basal slip system 2, (e) Accumulated slip for basal slip system 3, and (e) Most active slip system ID map for grains sharing GB of interest.

GB ID	Incoming slip system	Potential outgoing slip system
1	$(0001)[1\bar{2}10]$	$(0001)[11\bar{2}0]$
2	$(0001)[1\bar{2}10]$	$(0001)[1\bar{2}10]$
3	$(0001)[\bar{2}110]$	$(0001)[\bar{2}110]$
4	$(0001)[11\bar{2}0]$	$(0001)[11\bar{2}0]$
5	$(0001)[\bar{2}110]$	$(0001)[1\bar{2}10]$
6	$(0001)[1\bar{2}10]$	$(0001)[1\bar{2}10]$
7	$(0001)[\bar{2}110]$	$(0001)[\bar{2}110]$
8	$(0001)[1\bar{2}10]$	$(0001)[1\bar{2}10]$
9	$(0001)[11\bar{2}0]$	$(0001)[\bar{2}110]$

Table 3.4: Incoming and potential outgoing slip systems for different GBs identified by the GB ID

3.3. Grain Boundary Parameters

To parametrize the micro-Hall-Petch parameters by different metrics associated with the GB, a number of angular quantities(Fig. 3.17) need to be determined. These angles are computed from some information of the slip systems in the two grains sharing the GB and also the GB itself. The previous section described the procedure to obtain the incoming and potential outgoing slip systems. Hence, the only information required to obtain is the GB plane orientation - the angles α and β - as illustrated in Fig. 3.18. Using this information the relevant angles(ψ, δ, θ, κ) are computed, as listed in Table. 3.5 for all the nine GBs.

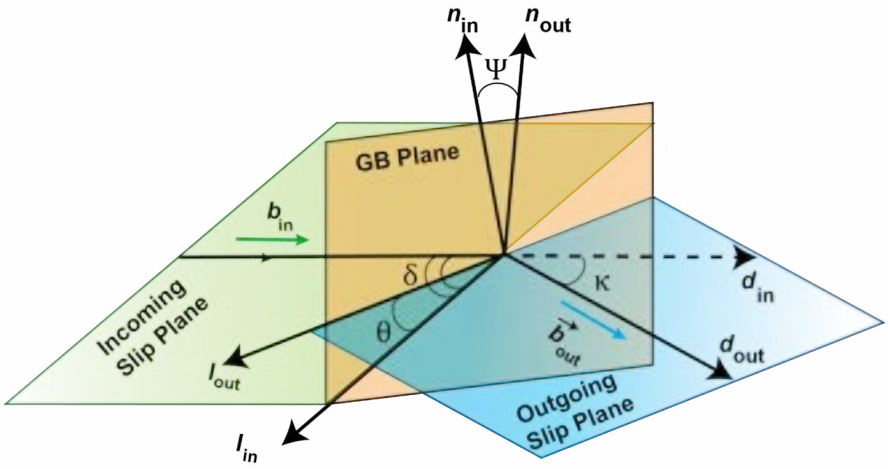

Figure 3.17: A schematic representative for slip transmission through a GB. $\vec{b}_{in}$: Burgers vector of the incoming slip system, $\vec{b}_{out}$: Burgers vector of the outgoing slip system, $\vec{n}_{in}$: Slip plane normal of the incoming slip system, $\vec{n}_{out}$: Slip plane normal of the outgoing slip system, $\vec{l}_{in}$: Intersection line of the incoming slip plane and GB, $\vec{l}_{out}$: Intersection line of the outgoing slip plane and GB, $\vec{d}_{in}$: Slip direction of the incoming slip system, $\vec{d}_{out}$: Slip direction of the outgoing slip system, θ: Angle between the two slip plane traces on the GB plane, κ: Angle between slip directions, ψ: Angle between slip plane normals, δ: Angle between the incoming slip direction and the incoming slip plane trace on the GB plane.

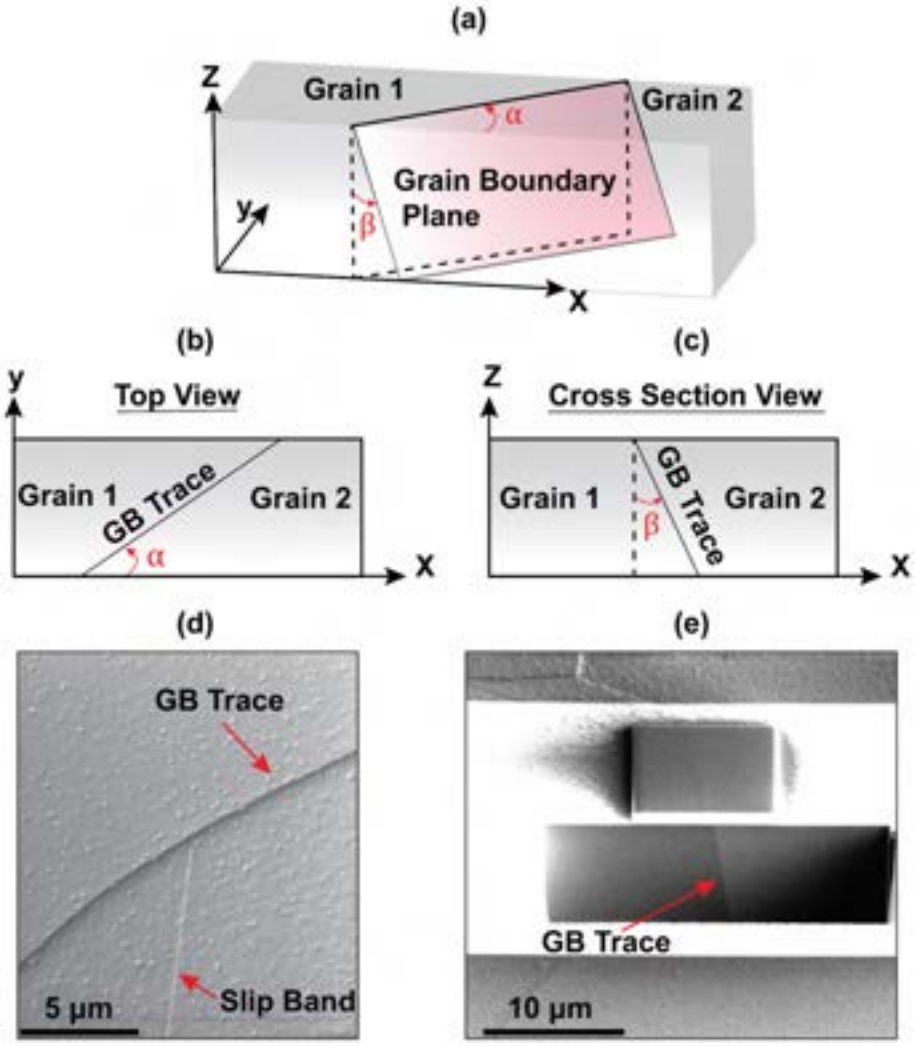

Figure 3.18: (a) Schematic showing the GB plane, which is described by (b) the GB trace angle, and (c) the GB plane angle. (d) The GB trace angle (α) is measured using the plan view image of the GB. (e) The GB plane angle (β) is measured using cross-section lamellae of GB prepared by field ion beam milling.

GB ID	$\theta(\circ)$	$\kappa(\circ)$	$\psi(\circ)$	$\delta(\circ)$
1	58.54	73.75	70.68	84.55
2	53.31	5.61	54.59	73.21
3	73.79	37.30	31.70	45.24
4	76.16	87.81	31.77	55.64
5	33.87	55.69	25.95	26.46
6	38.84	54.14	48.32	86.18
7	46.52	46.94	47.13	24.57
8	74.92	66.16	87.18	34.41
9	70.16	88.42	86.91	86.38

Table 3.5: Relevant geometric quantities(angles) computed from the slip system and GB information to parametrize the micro-Hall-Petch parameter.

3.4. Parametrizing the micro-Hall-Petch parameter

Among the multitude of relationships that can be established between the micro-Hall-Petch parameter and the different angular quantities, we consider two particular GB metrics for the parametrization. These GB metrics are motivated from earlier studies targeted towards the development of slip transmission criteria[138] :

- The Lee-Robertson-Birnbaum(LRB) factor[139, 140, 141] defined as $\cos(\theta)\cos(\kappa)$. This factor was originally proposed in the context of determining the outgoing slip system as a result of slip transmission across GBs, based on in situ straining TEM experiments on FCC alloys. This relationship agrees with studies by

Lim et al.[142] where the strengthening effect of GBs in Fe–3%Si was modeled by defining the GB obstacle stress, τ_{obs} as $\tau_{obs} = \tau^*(1 - \cos(\theta)\cos(\kappa))$ where τ^* represents the maximum obstacle strength. The Hall-Petch coefficient is also known to be correlated with the GB obstacle stress[134] and hence is indirectly related to the LRB factor. We note that this parameter depends on the slip system information in neighboring grains, and the GB inclination.

- The Luster-Morris(LM) factor[143, 138] defined as $\cos(\psi)\cos(\kappa)$. A slip transmission criterion was proposed in their work on the study of a two-phase Ti-Al alloy where they conducted a detailed analysis of active slip systems using transmission electron microscopy (TEM) on deformed samples. Based on a theoretical calculation of a geometric compatibility factor characterizing the best slip transfer across adjacent grains, they were able to deduce the role played by the type of orientation relationship between grains in producing active deformation systems that allow the maximum compatibility of deformation. We note that this parameter depends solely on the slip system information in the neighboring grains.

Let m' denote either the LRB factor or LM factor, which we refer to as the compatibility factor since it is a measure of compatibility between adjacent grains - higher the value of m' greater the probability of slip transmission. Then we consider a simple empirical power-law dependence of the micro-Hall-Petch parameter on the compatibility factor :

$$k_\mu^\alpha = K_\mu^\alpha \left(1 - m'\right)^{c^\alpha} \;\; ; \;\; c^\alpha > 0 \tag{3.7}$$

where K_μ^α is the micro-Hall-Petch multiplier and c^α is the micro-Hall-Petch exponent. Since a higher value of the micro-Hall-Petch parameter k_μ^α signifies higher blocking tendency of the GB to an incoming slip band, it is assumed to monotonically increase with the factor $1 - m'$ which signifies the loss of compatibility in some sense. c^α denotes the exponent appearing in the empirical power-law relationship. Performing a linear least-squares fit of $\log\left(k_\mu^\alpha\right)$ relative to $\log\left(1 - m'\right)$ yields the best fit micro-Hall-Petch multiplier and exponent, which is considered a material property since the GB dependence is now subsumed in m'. Figs. 3.19a- 3.19b depict the plots of the micro-Hall-Petch parameter against the corresponding metrics, i.e. the LRB factor and LM factor, respectively. The fit results in $K_\mu^\alpha = 173$ MPa $\mu m^{1/2}$, $c^\alpha = 1.04$ for the LRB factor and $K_\mu^\alpha = 159$ MPa $\mu m^{1/2}$, $c^\alpha = 0.6$ for the LM factor. It is interesting to note a close-to-linear relationship between micro-Hall-Petch parameter and $(1 - m')$ where m' is the LRB factor. Even though the parametrization of the micro-Hall-Petch parameter relative to the LRB factor is more appropriate, the parametrization relative to the LM factor is simple both in terms of ease of constructing the LM factor from experiments and in incorporating it in CPFE models where the GBs are not explicitly captured except in terms of shared faces between grains.

3.5. Conclusion

An integration between experimental measurements, dislocation pile-up theory, crystal plasticity simulations and some empirical modeling has been presented in order to determine the micro-Hall-Petch multiplier and exponent for basal slip, which are

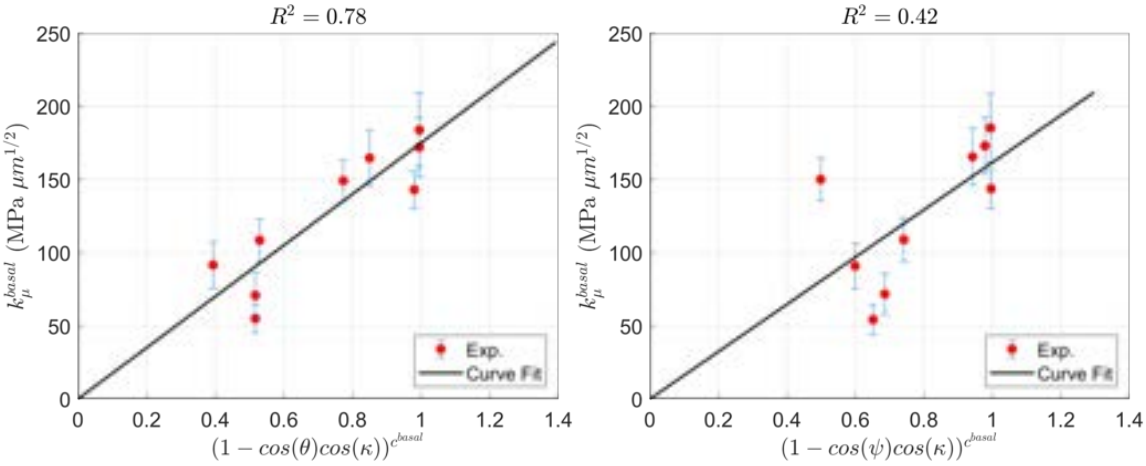

(a) (b)

Figure 3.19: (a) micro-Hall-Petch parameter plotted against $(1 - m')^{c^\alpha}$ where m' is the LRB factor, along with the linear fit. $K_\mu^\alpha = 0.173$ MPa $\mu m^{1/2}$, $c^\alpha = 1.04$. (b) micro-Hall-Petch parameter plotted against $(1 - m')^{c^\alpha}$ where m' is the LM factor, along with the linear fit. $K_\mu^\alpha = 159$ MPa $\mu m^{1/2}$, $c^\alpha = 0.6$.

the relevant material properties characterizing the dependence of the size-dependent contribution of the slip system resistance on certain GB parameters. Pile-up stress measurements were fit to a theoretical expression derived from continuum dislocation pile-up theory to obtain estimates of the micro-Hall-Petch parameter for nine different GBs. To parametrize the micro-Hall-Petch parameters relative to different metrics encoding the slip system information, CPFE simulations were conducted on neighborhoods of the GBs to obtain the incoming slip system(corresponding to the observed experimental slip band) and the potential outgoing slip system(in the adjacent grain blocking the slip band). Using this information and GB inclination information two parametrizations were considered for the micro-Hall-Petch parameter relative to the LRB factor and LM factor based on an empirical power-law relationship. The multiplier and exponents associated with the power-law furnish material

parameters which encode the effect of the GB on the size-dependent contribution of the slip system resistance corresponding to basal slip.

CHAPTER IV

Micro-Hall-Petch Parameters for Prismatic Slip

In this chapter, we detail the integration of theory and computation with experiments to obtain estimates of the micro-Hall-Petch parameters for different GBs, and subsequently compute the micro-Hall-Petch coefficients. We start by describing the procedure to identify potential grains where the notch may be constructed in order to initiate prismatic slip from the notch tips. This is followed by the continuum dislocation pile-up theory in one-dimension to model the notch-slip band combination as a continuous distribution of dislocations, which furnishes a closed-form expression for the stress ahead of the pile-up. This expression is fit to HR-EBSD measurements of the pile-up from which the micro-Hall-Petch parameters for basal slip are estimated for different GBs. We then outline the calibration procedure to obtain constitutive model parameters which are then used to simulate neighborhoods of GBs of interest to obtain the potential outgoing slip system in the grain blocking the slip band, which are used to construct relevant GB metrics. The micro-Hall-Petch parameters are then related to two GB metrics motivated from slip transmission studies in order

to identify the micro-Hall-Petch coefficients - the micro-Hall-Petch multiplier and the micro-Hall-Petch exponent for basal slip [132, 133]. [144].

4.1. Grain Identification for Notch Creation

It is well known that the anisotropy of the HCP crystal structure reflects significantly higher critical resolved shear stress for prismatic relative to the basal slip system. To preferentially activate prismatic slip at the low level of stress (which is important to consider for capturing high-resolution Kikuchi patterns) a series of sharp micro-notches were machined in grains oriented (relative to the loading direction) specifically for the prismatic slip to act as slip initiation sites. Given the EBSD data of the microstructure section(an example microstructure), grains were then identified using the following procedure :

1. Read in the EBSD data using MTEX and partition the microstructure section into different grains(Fig. 4.1).

2. Identify grains for which at least one prismatic slip system possesses a Schmid factor (corresponding to tension along the extrusion direction) greater than or equal to 0.4(Fig. 4.2). This was to ensure that there is at least one prismatic slip system-oriented favorably for plastic slip relative to loading.

3. Separate grains with threshold in the ratio of the maximum Schmid factor of basal slip systems to the maximum Schmid factor of prismatic slip systems(Fig. 4.3). This is to ensure that the basal system is not as favorably oriented as the prismatic system obtained from the previous step.

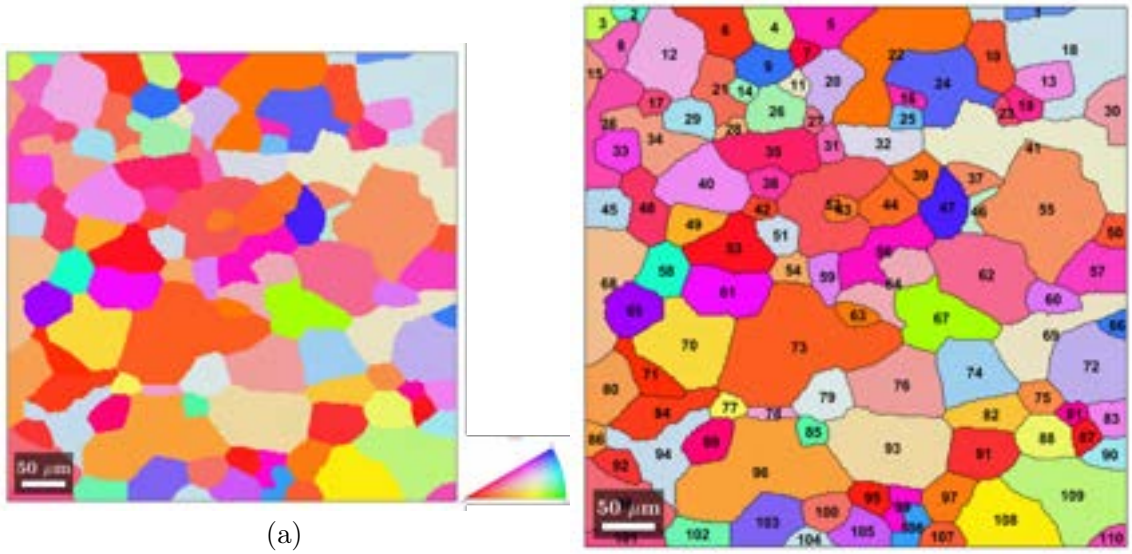

(a)

(b)

(c)

Figure 4.1: (a) EBSD data corresponding to microstructure section, (b) Partition microstructure into grains, and (c) Basal slip trace for all grains.

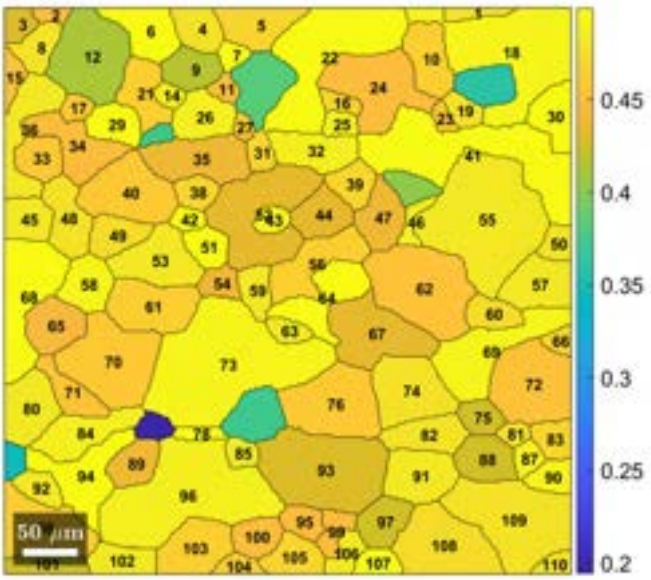

Figure 4.2: Plot of maximum Schmid factor among prismatic systems with grain ids of grains satisfying satisfying the criterion from the second step.

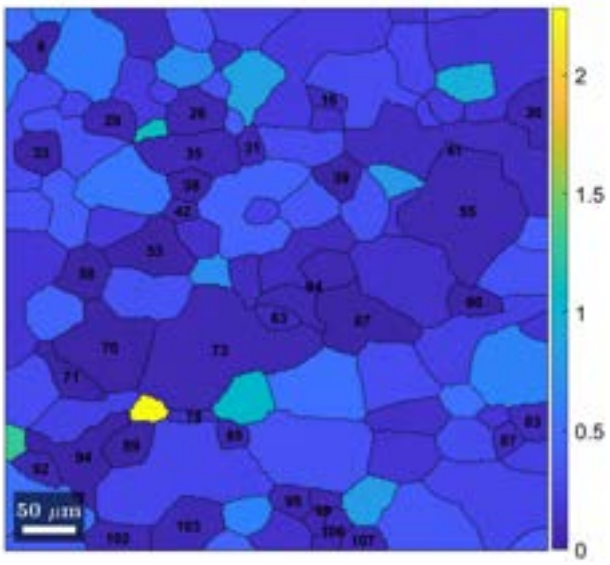

Figure 4.3: Plot of ratio of maximum Schmid factor among basal systems to maximum Schmid factor among prismatic systems, with grain ids of grains satisfying the criterion from the third step.

4. For ease of fabricating the notch using FIB milling, identify those grains with prismatic systems obtained from the previous steps(Fig. 4.4a) having a plane normal lying favorably in the plane of the sample surface(Fig. 4.4b).

The above steps were automated using a MATLAB script using the MTEX [128, 129] toolbox to postprocess EBSD data.

4.2. Dislocation Pile-up Model of Notch-Slip Band Combination

A simple one-dimensional continuum dislocation pile-up model is used as an analogy to describe the region in the grain constituting the notch and the slip band (Fig. 4.5). Both the notch and the slip band are represented by a continuous distribution of straight parallel edge dislocations [145, 146] with the dislocation line pointing in the z-direction, and Burgers vector along the x-direction with magnitude b_e. Let $\rho(x)$ denote the distribution of dislocations in the domain $[-a, a]$ where the subinterval $[-b, b]$ represents the notch. We would then like to solve for $\rho_e(x)$ which is the dislocation density in equilibrium with an effective resolved stress $\tau_e(x)$, where the equilibrium condition takes the following form [147] :

$$\frac{\mu b_e}{2\pi(1-\nu)}\left[\int_{-a}^{-b}\frac{\rho_e(x')dx'}{x-x'}+\int_{-b}^{b}\frac{\rho_e(x')dx'}{x-x'}+\int_{b}^{a}\frac{\rho_e(x')dx'}{x-x'}\right]+\tau_e(x)=0$$

$$\tau_e=\begin{cases}\tau & ;\ |x|<b\\ \tau-\tau_f & ;\ b<|x|<a\end{cases} \tag{4.1}$$

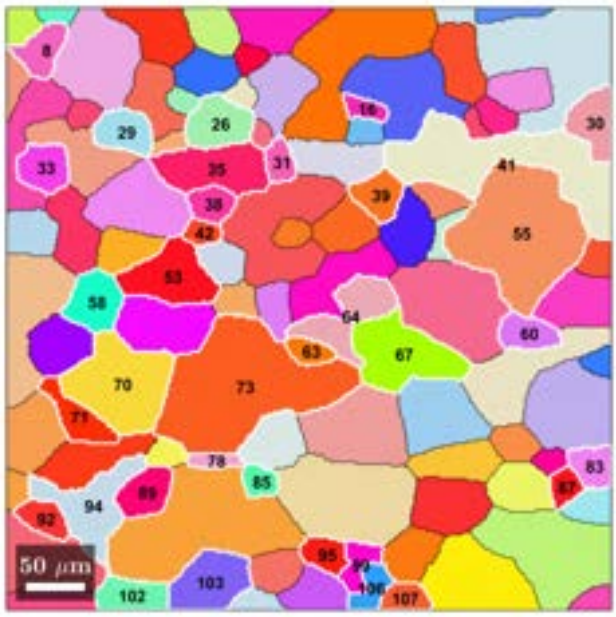

(a)

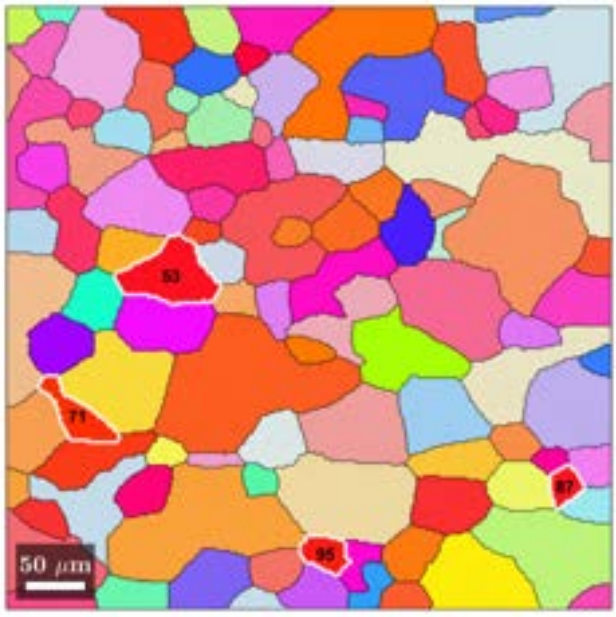

(b)

Figure 4.4: (a) Grains selected based on first two steps, (b) Grains selected based on orientation of prismatic plane normal from the final step.

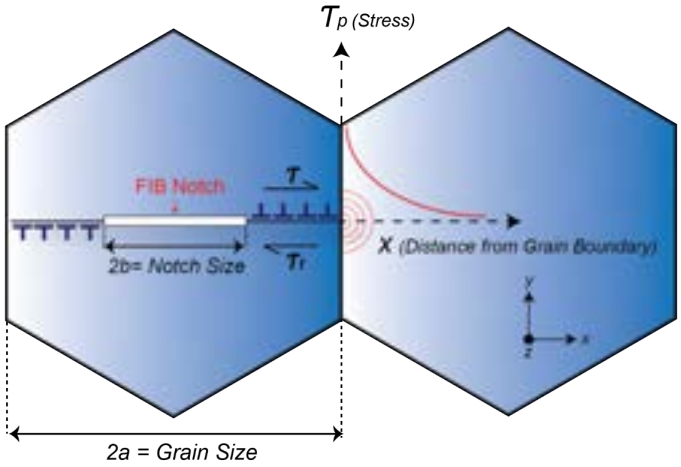

Figure 4.5: Notch and slip band idealized as a continuous distribution of parallel edge dislocations.

where μ is the shear modulus, ν is the Poisson's ratio, τ is the applied shear and τ_f is the friction stress acting only in the slip band inhibiting the motion of prismatic dislocations. τ_f is assumed to be constant. We are interested in a closed-form expression for the pile-up stress, $\tau_p(x)$ defined as follows :

$$\tau_p(x) = \frac{\mu b_e}{2\pi(1-\nu)} \left[\int_{-a}^{-b} \frac{\rho_e(x')dx'}{x-x'} + \int_{-b}^{b} \frac{\rho_e(x')dx'}{x-x'} + \int_{b}^{a} \frac{\rho_e(x')dx'}{x-x'} \right] \; ; \; x > a \qquad (4.2)$$

Eqn. 4.1 is an integral equation with a closed-form solution for $\rho_e(x)$, which upon substituting into Eqn. 4.2 yields [147, 148]

$$\tau_p(x) = \frac{\tau - 2\tau_f \cos^{-1}\left(\frac{b}{a}\right)}{\sqrt{1-\left(\frac{a}{x}\right)^2}} + 2\tau_f \mathrm{cosec}^{-1}\left(\sqrt{1+\frac{(x^2-a^2)\,b^2}{(a^2-b^2)\,x^2}}\right) - \tau \; ; \; x > a \qquad (4.3)$$

Shifting the origin to $x = a$ by a change of variables $X \coloneqq x - a$ the expression for the pile-up stress is

$$\tau_p(X) = \frac{\tau - 2\tau_f \cos^{-1}\left(\frac{b}{a}\right)}{\sqrt{1 - \left(\frac{a}{X+a}\right)^2}} + 2\tau_f \operatorname{cosec}^{-1}\left(\sqrt{1 + \frac{X\left(2a+X\right)b^2}{\left(a^2-b^2\right)\left(X+a\right)^2}}\right) - \tau \ ; \ X > 0 \tag{4.4}$$

Invoking the micro-Hall-Petch assumption with decomposition of τ into size-independent and size-dependent contributions at the level of the slip system, we replace τ with τ^α corresponding to slip system α. The decomposition then takes the simple form

$$\tau^\alpha = \tau_0^\alpha + \frac{k_\mu^\alpha}{\sqrt{2a}} \tag{4.5}$$

where τ_0^α is the size-independent contribution to the critical resolved shear stress on slip system α, k_μ^α is the micro-Hall-Petch parameter and a is the grain size. Substituting Eqn. 4.5 into Eqn. 4.4 and specializing to slip system α yields

$$\tau_p^\alpha(X) = \frac{\tau_0^\alpha + \frac{k_\mu^\alpha}{\sqrt{2a}} - 2\tau_f \cos^{-1}\left(\frac{b}{a}\right)}{\sqrt{1 - \left(\frac{a}{X+a}\right)^2}} + 2\tau_f \operatorname{cosec}^{-1}\left(\sqrt{1 + \frac{X\left(2a+X\right)b^2}{\left(a^2-b^2\right)\left(X+a\right)^2}}\right) - \left(\tau_0^\alpha + \frac{k_\mu^\alpha}{\sqrt{2a}}\right) \tag{4.6}$$

Eqn. 4.6 furnishes an expression for the pile-up stress ahead of the pile-up, which is fit to the data obtained from HR-EBSD residual stress measurements. Here a and b are known parameters since they are lengths which can be measured in experiments. An estimate of τ_0^α is obtained by multiplying σ_0(the Hall-Petch intercept) and the

average Schmid factor associated with prismatic slip for the as-extruded texture. The average Schmid factor for prismatic slip is obtained by first computing the maximum Schmid factor for each orientation among the prismatic slip systems, and then finding the mean of those values. In our case, this value is 0.451, very similar to previous work [149] which reported a value of 0.43. σ_0 denotes the yield strength for the microstructure with theoretically infinite grain size, and multiplying this by the average Schmid factor for prismatic slip results in an estimate of the grain-size independent critical resolved shear stress for prismatic slip. In our case we obtain $\tau_0^\alpha = 42.54$ MPa. The parameters k_μ^α and τ_f^α are the unknowns which are optimized for by performing a least-squares fit of Eqn. 4.6 to the pile-up stress measurements from experiments(Fig. 4.6). This was carried out for seven different GBs for which the slip band size, notch size and micro-Hall-Petch parameter are included in Table. 4.1.

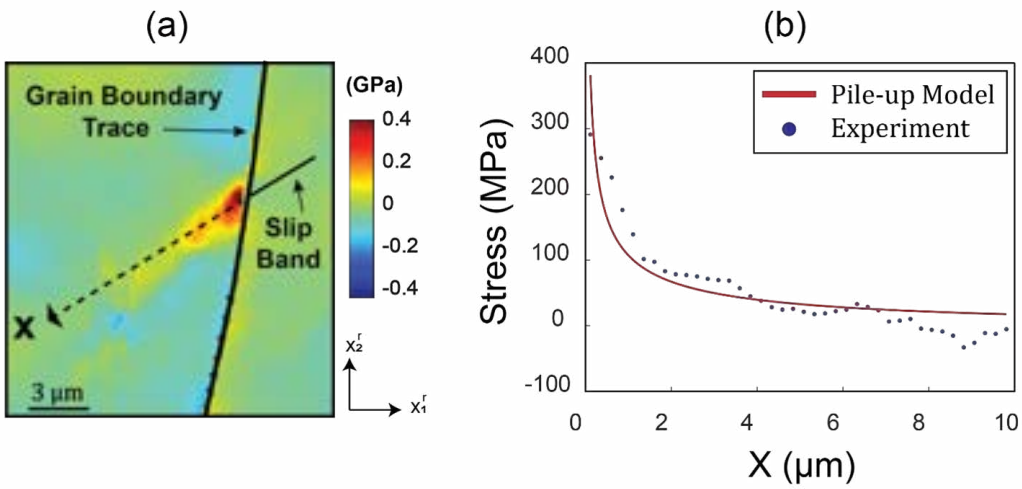

Figure 4.6: (a) HR-EBSD stress map of the resolved shear stress on the active slip system in the right grain. The active slip system is defined based on the trace analysis and CPFE. The observed stress profile in front of the pile-up is extracted along the dashed line and compared with the pile-up model. (b) The comparison of resolved shear stress ahead of pile up was measured by HR-EBSD and the pile-up model (Eqn. 4.6) to estimate the prismatic micro-Hall-Petch parameter for different GBs.

GB ID	Slip band size (μm)	Notch size (μm)	micro-Hall-Petch parameter (MPa $\mu m^{1/2}$)
1	40	20	455 ± 50
2	40	20	618 ± 60
3	39	19	661 ± 70
4	44	21	635 ± 70
5	41	18	685 ± 20
6	41	17	138 ± 20
7	41	17	641 ± 70

Table 4.1: List of micro-Hall-Petch parameters for prismatic slip bands for different GBs.

4.3. Crystal Plasticity Simulations

To parametrize the micro-Hall-Petch parameter values for different GBs relative to GB metrics, relevant information about the slip systems in the grains sharing the boundary is necessary. The information of the incoming slip system in the grain containing the slip band is available by analyzing the trace of the slip band, since this time it is a prismatic slip system. Since we do not know apriori which slip system will be chosen as the one to transmit slip in the neighboring grain, we setup crystal plasticity simulations of the GB neighborhoods to obtain this information similar to Chapter III. We now cover details regarding calibration of the crystal plasticity

constitutive model and simulations of GB neighborhoods.

4.3.1. Constitutive Model Calibration

The crystal plasticity constitutive model parameters are obtained by matching the stress-strain curves between simulations and experiments for Mg-4Al samples for two different textures. Fig. 4.7 depicts the pole figures and the synthetic microstructures corresponding to both textures generated using DREAM.3D represented as a 60 x 60 x 60 voxelated grid containing approximately 2000 grains. Microstructures from both scenarios were subject to simple tension along the z-direction(Fig. 4.8) to different values of strain - (i) the microstructure with texture 1 was subject to approximately 2.5% elongation, and (ii) the microstructure with texture 2 was subject to approximately 0.6% elongation. All crystal plasticity simulations were performed assuming possible activity of 12 slip systems - 3 basal, 3 prismatic, 6 pyramidal <c+a> - and 6 extension twin systems. Fig. 4.9 depicts the comparison between the stress-strain curves from CPFE simulations and experiments for the first and second scenario, respectively, showing a reasonable match. The elastic stiffness constants for Mg-4Al have been adopted from earlier work [150, 151] - $C_{11} = 59.4$ GPa, $C_{33} = 61.6$ GPa, $C_{12} = 25.61$ GPa, $C_{13} = 21.44$ GPa and $C_{44} = 16.4$ GPa. Table 4.2 lists the crystal plasticity constitutive model parameters obtained post-calibration. In the hardening law, the latent hardening coefficient was set to $q = 1.0$, while the flow rule parameters were set as $\dot{\gamma}_0 = 0.001\text{s}^{-1}$ and $m = 34$.

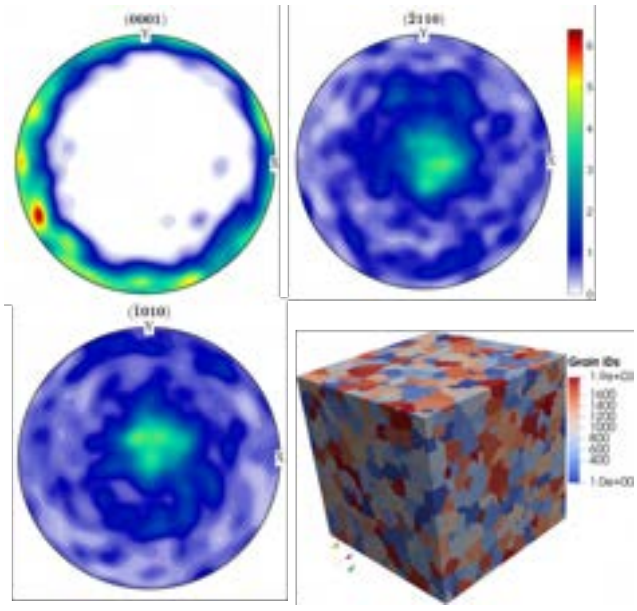

(a)

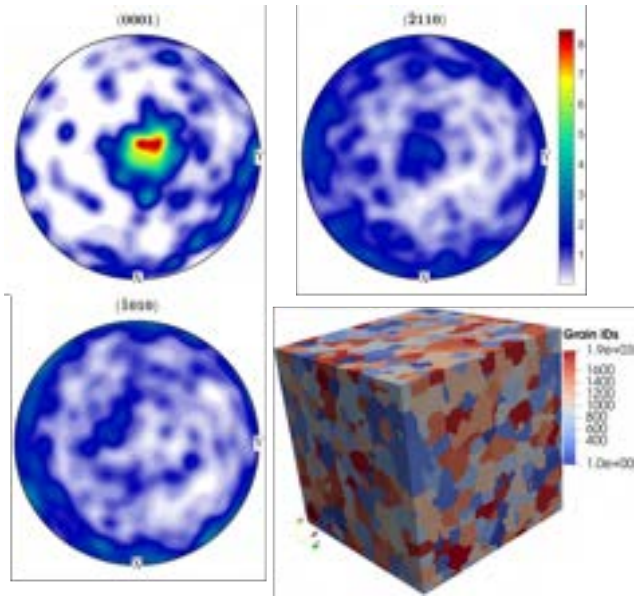

(b)

Figure 4.7: Pole figures and synthetic microstructure for (a) Texture 1, and (b) Texture 2.

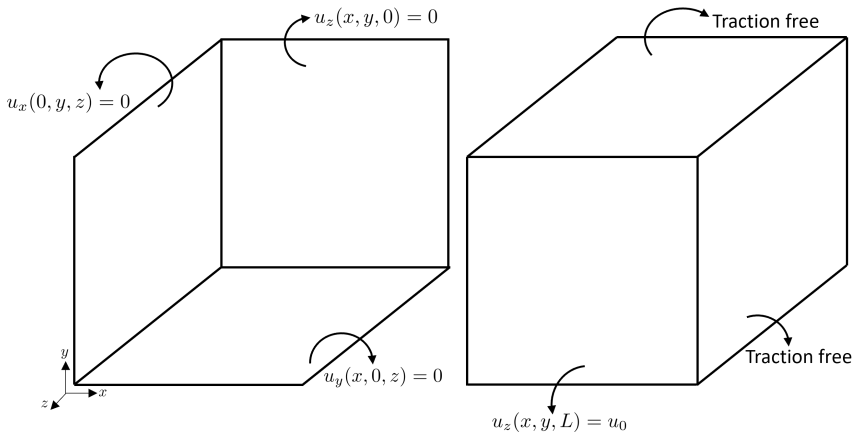

Figure 4.8: Simple tension boundary conditions that the microstructures are subject to. u_0 denotes the displacement enforced based on the strain - 2.5 % for texture 1 and 0.6 % for texture 2. Then $u_0 = 0.025L$ for texture 1 and $u_0 = 0.006L$ for texture 2.

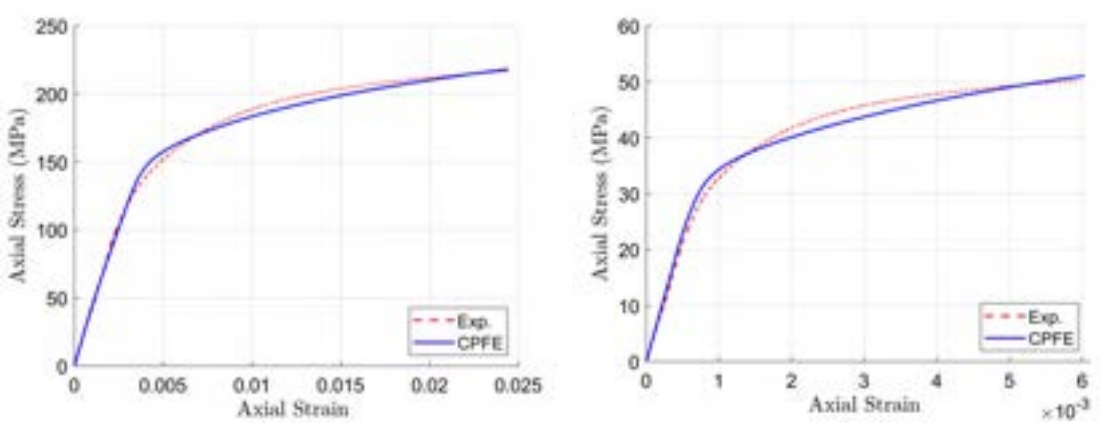

(a) (b)

Figure 4.9: Stress-strain curve comparison between experiments and CPFE for (a) Texture 1, and (b) Texture 2.

Deformation mode	s_0^α(MPa)	h_0^α(MPa)	s_s^α(MPa)	a^α
Basal	10.0	0	-	1.0
Prismatic	78.0	1000.0	150.0	1.0
Pyramidal	140.0	0.0	-	1.0
Twin	18.0	0	-	1.0

Table 4.2: Calibrated crystal plasticity constitutive model parameters.

4.3.2. Grain Boundary Neighborhood Simulations

To construct GB descriptors through which a relationship can be drawn to the micro-Hall-Petch parameter, some information about the slip activity in the grains is necessary. By virtue of capturing the resolved stress ahead of the blocked slip band, the slip system in the adjacent grain which could potentially accommodate slip transmission, is not known. In the grain containing the slip band, the slip trace and crystallographic orientation can be used to infer the slip system corresponding to that slip band (incoming slip system). To find the slip system that could potentially accommodate slip transmission (potential outgoing slip system), crystal plasticity simulations are employed.

To accomplish this, for each GB case studied, a rectangular region around this GB is identified (Figs.4.10a-4.10b), which contains the grains sharing this boundary and some of their neighbors. The approximate coordinates of the center of the notch and its length are identified. This information is then used to create a rectangular geometry of the region of interest, with the notch approximated as an ellipse with the same center as that of the notch and major axis length equal to the notch size.

This microstructure section (a 2D section) is then meshed using 4-noded quadrilateral elements using Gmsh [4], an open-source 3D finite element mesh generator (Fig. 4.10c), with a finer mesh in the neighborhood of the notch. The elements are then assigned an identifier corresponding to whichever grain the element centroid constitutes in the original microstructure (Fig. 4.10d). The 2D microstructure section is then extruded along the third direction to create a 3D microstructural slice with 8-noded hexahedral elements. The microstructure slices were then subject to simple tension boundary conditions with deformation along x-direction upto 2% strain(Fig. 4.11). Simulations were performed for seven different GB neighborhoods for which the micro-Hall-Petch parameters were computed from the pile-up stress measurements combined with curve fitting. Simulations were conducted on GB neighborhoods for seven GB cases. Fig. 4.12 depicts the variation of accumulated slip for the three basal and three prismatic slip systems for the specific GB neighborhood. It is interesting to observe relatively significant prismatic slip corresponding to all three prismatic slip systems in the grain containing a notch close to both notch ends. This is most likely caused by significant changes in the in-plane stress state around the notch due to the curvature of the sharp notch. Crystal plasticity finite element simulations cannot capture the nucleation and propagation of slip bands as observed in the experiments. However, the experimental hypothesis associated with the activation of prismatic slip ahead of the notch tip is corroborated by the accumulated slip variation which shows profuse prismatic slip activity close to the notch. While the true physics associated with choice of a specific slip band is a very complex problem to study, such simulations can be setup with models more

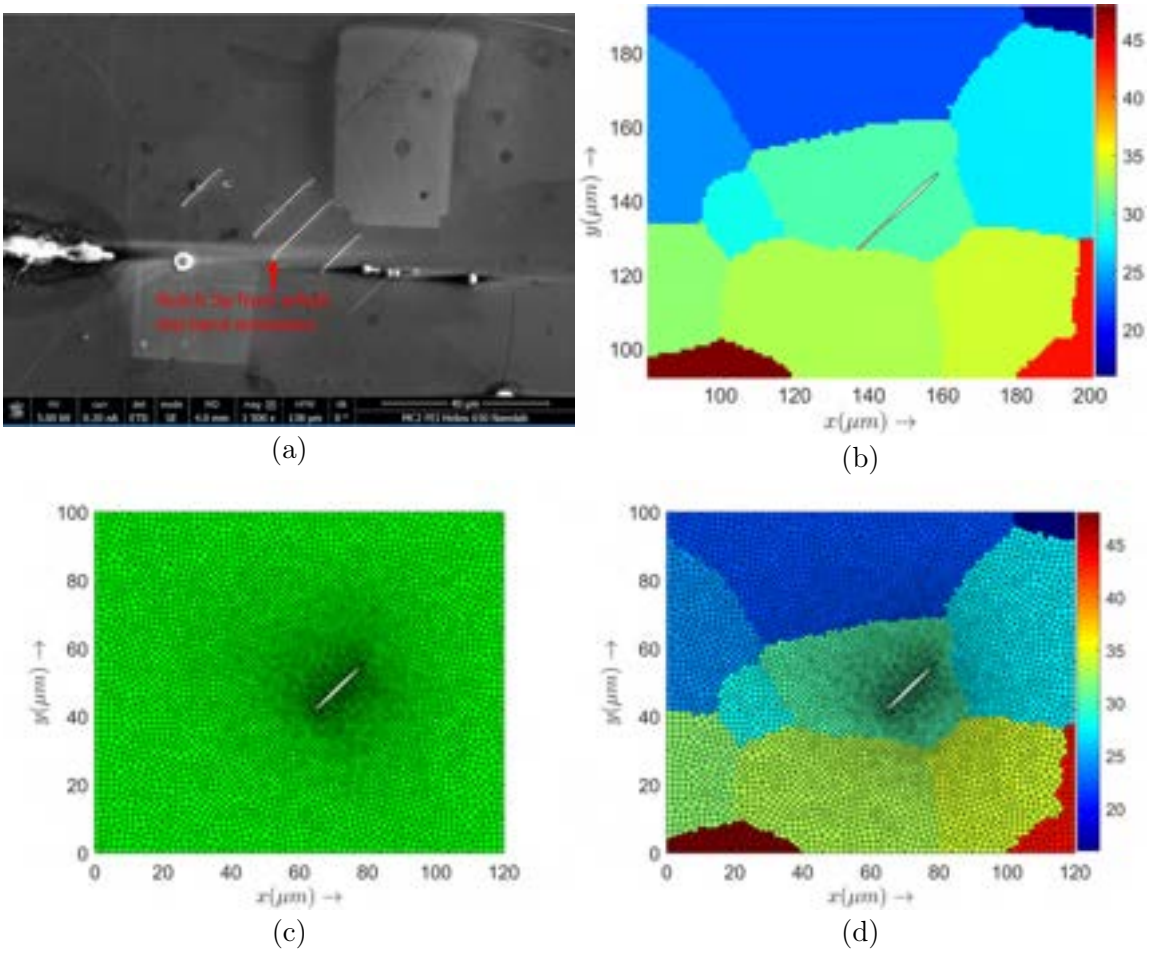

Figure 4.10: (a) Microstructure section from experiment containing a notch with the tip shown from which a slip band emanates, (b) Read in experimental data and assign grain IDs, (c) Rectangular domain containing notch meshed using Gmsh [4] containing 7780 elements, and (d) Grain IDs assigned to elements of the mesh.

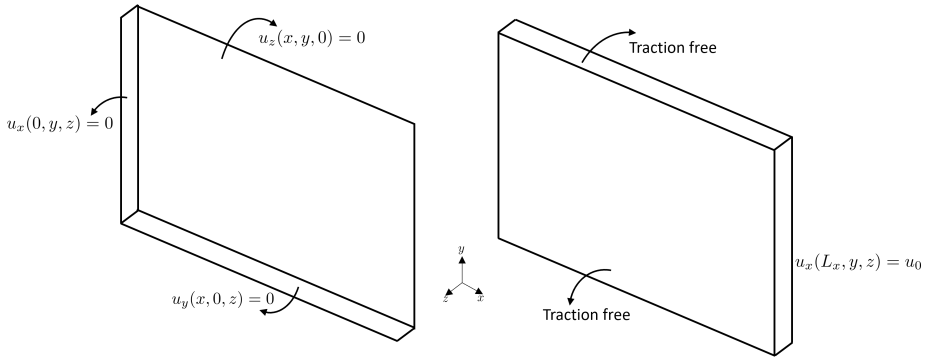

Figure 4.11: Simple tension boundary conditions applied to the microstructure slice with deformation along x-direction upto 2%, i.e., $u_0 = 0.02L_x$.

enriched with the underlying physics to capture slip band initiation. For the present case, our interest lies in the potential outgoing slip system in the neighboring grain blocking the slip band in the experiment. Fig. 4.13b is a discrete map denoting the slip system ID with the most accumulated slip at each element of the FE mesh, with Fig. 4.13a zooming in on the region around the notch from which the slip band emanates in experiments. This map particularly highlights the point made earlier about different prismatic slip systems being dominant at different regions around the notch. In this particular case, the alignment of the notch corresponds to that of the $[1\bar{2}10]\,(10\bar{1}0)$ prismatic system, for which the slip band emanates from the notch tip in the experiments. The slip system ID map is used to obtain the potential outgoing slip system. We choose this to be the slip system with the highest accumulated slip in the neighborhood of the slip band trace-GB intersection at the end of deformation. In the case of conflict in the choice of slip systems, we choose the potential outgoing system as the one that is the most dominant in the neighborhood of the slip trace-GB intersection. In this case, the potential outgoing slip system is chosen as

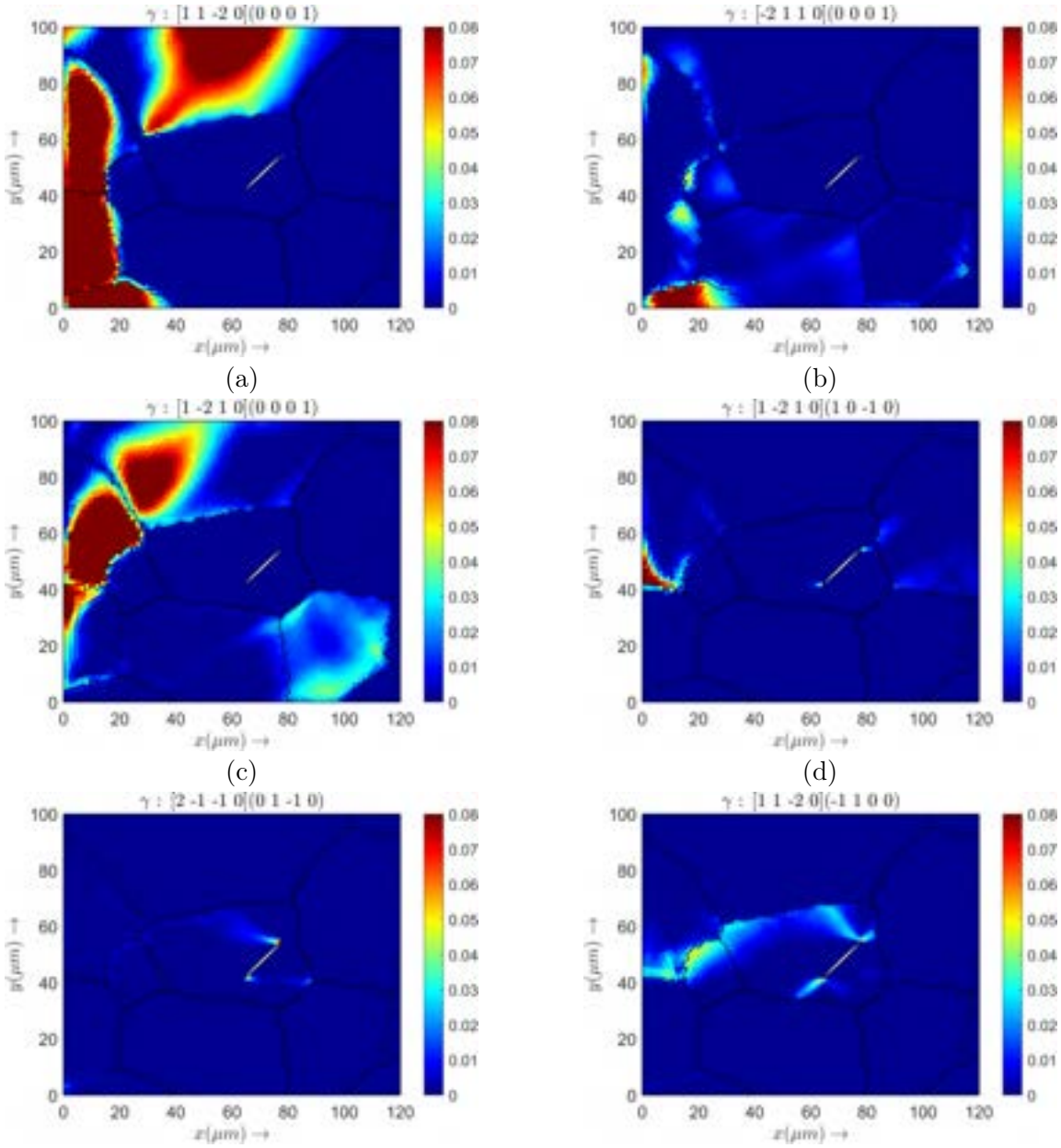

(a) (b) (c) (d) (e) (f)

Figure 4.12: Accumulated slip variation of different slip systems : (a) Basal 1 - $[11\bar{2}0](0001)$, (b) Basal 2 - $[\bar{2}110](0001)$, (c) Basal 3 - $[1\bar{2}10](0001)$, (d) Prismatic 1 - $[1\bar{2}10](10\bar{1}0)$, (e) Prismatic 2 - $[\bar{2}110](01\bar{1}0)$, (f) Prismatic 3 - $[11\bar{2}0](\bar{1}100)$.

the one with ID 2, which is the basal system $[\bar{2}110](0001)$. Repeating this procedure

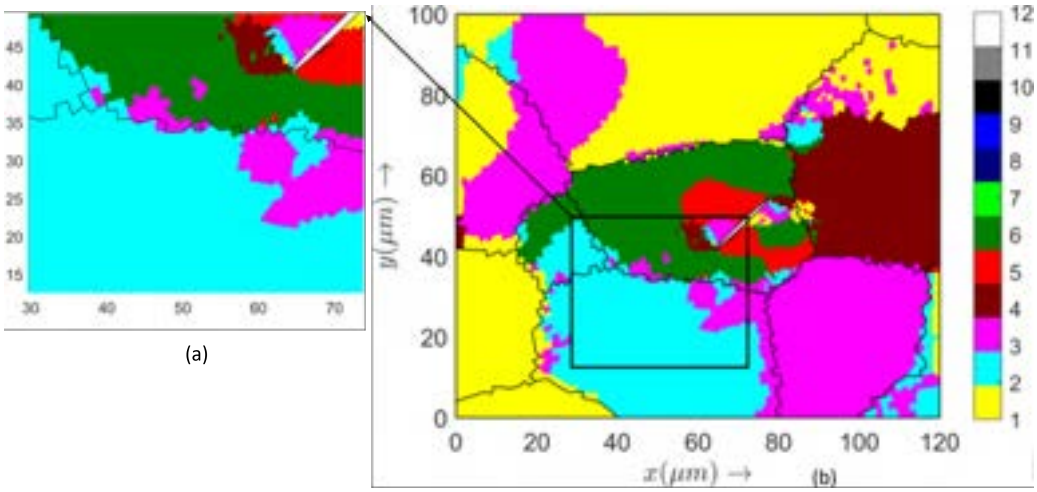

Figure 4.13: (a) Close-up of most active slip system ID map for GB 1, (b) Complete map for most active slip system ID for GB 1.

for the remaining 6 boundaries yields a potential outgoing slip system for each case. Figs.4.14-4.19 depict some information associated with each of those cases - (i) the microstructure with the slip band trace (ii) the mesh generated using Gmsh with Grain IDs assigned (iii) accumulated slip variation for just the prismatic systems, and (iv) the most active slip system ID considering all slip systems. Table.4.3 lists the incoming and potential outgoing slip system for all seven GBs.

GB ID	Incoming slip system	Potential outgoing slip system
1	$(01\bar{1}0)[\bar{2}110]$	$(0001)[\bar{2}110]$
2	$(01\bar{1}0)[\bar{2}110]$	$(10\bar{1}0)[1\bar{2}10]$
3	$(10\bar{1}0)[1\bar{2}10]$	$(0001)[\bar{2}110]$
4	$(\bar{1}100)[11\bar{2}0]$	$(0001)[\bar{2}110]$
5	$(10\bar{1}0)[1\bar{2}10]$	$(0001)[1\bar{2}10]$
6	$(01\bar{1}0)[\bar{2}110]$	$(01\bar{1}0)[\bar{2}110]$
7	$(01\bar{1}0)[\bar{2}110]$	$(0001)[\bar{2}110]$

Table 4.3: Incoming and potential outgoing slip systems for different GBs.

4.4. Grain Boundary Parameters

To parametrize the micro-Hall-Petch parameters by different metrics associated with the GB, a number of angular quantities(Fig. 4.20) need to be determined. These angles are computed from some information of the slip systems in the two grains sharing the GB and also the GB itself. The previous section covered the procedure to obtain the incoming and potential outgoing slip systems. Hence, the only information required to obtain is the GB plane orientation - the angles α and β - as illustrated in Fig. 4.21. Using this information the relevant angles(ψ, δ, θ, κ) are computed, as listed in Table. 4.4 for all the seven GBs.

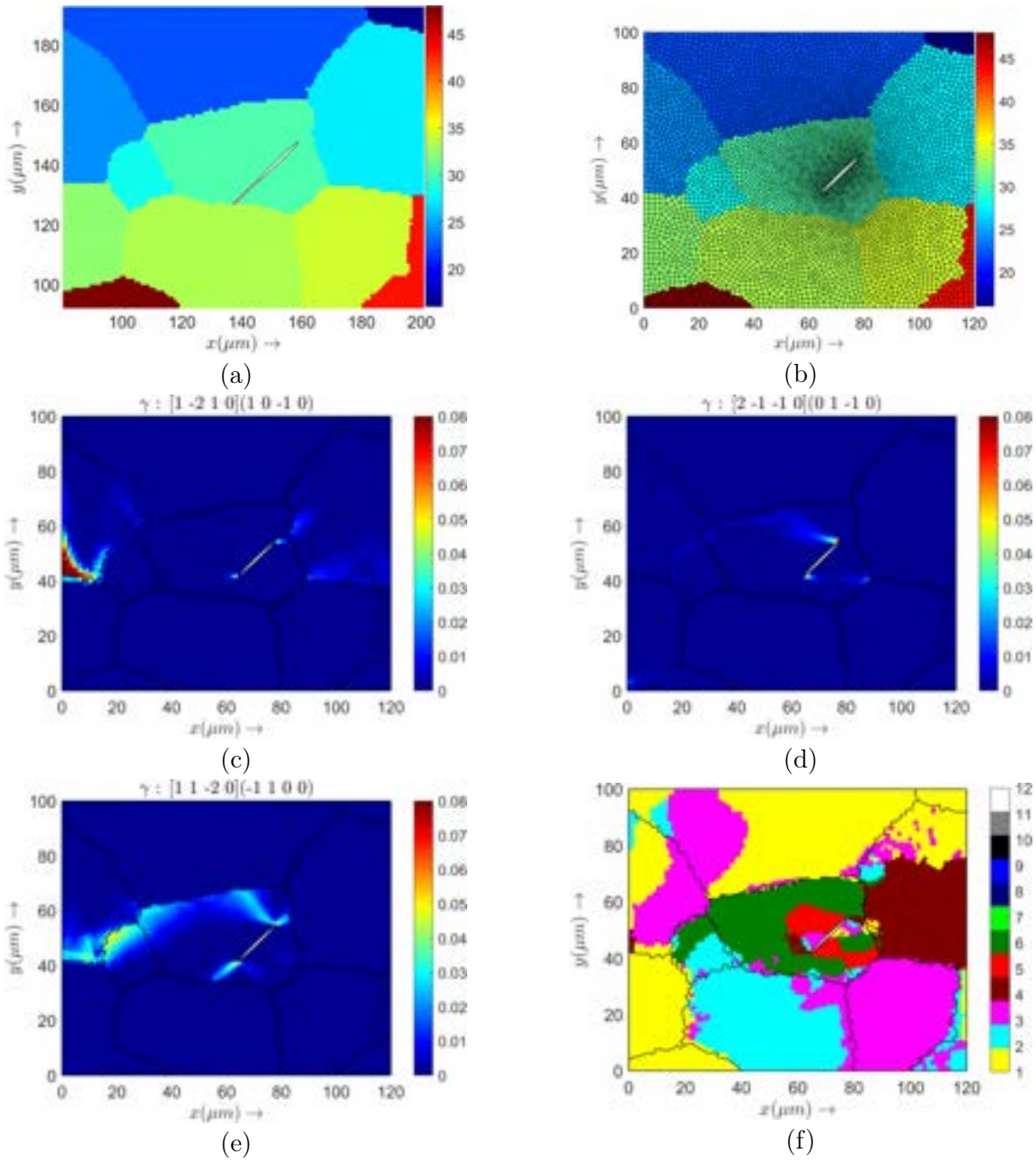

Figure 4.14: Accumulated slip variation of different slip systems : (a) microstructure for GB 2 with slip band trace, (b) Gmsh mesh containing 7780 elements, (c) Accumulated slip for prismatic 1, (d) Accumulated slip for prismatic 2, (e) Accumulated slip for prismatic 3, (f) Most active slip system ID map.

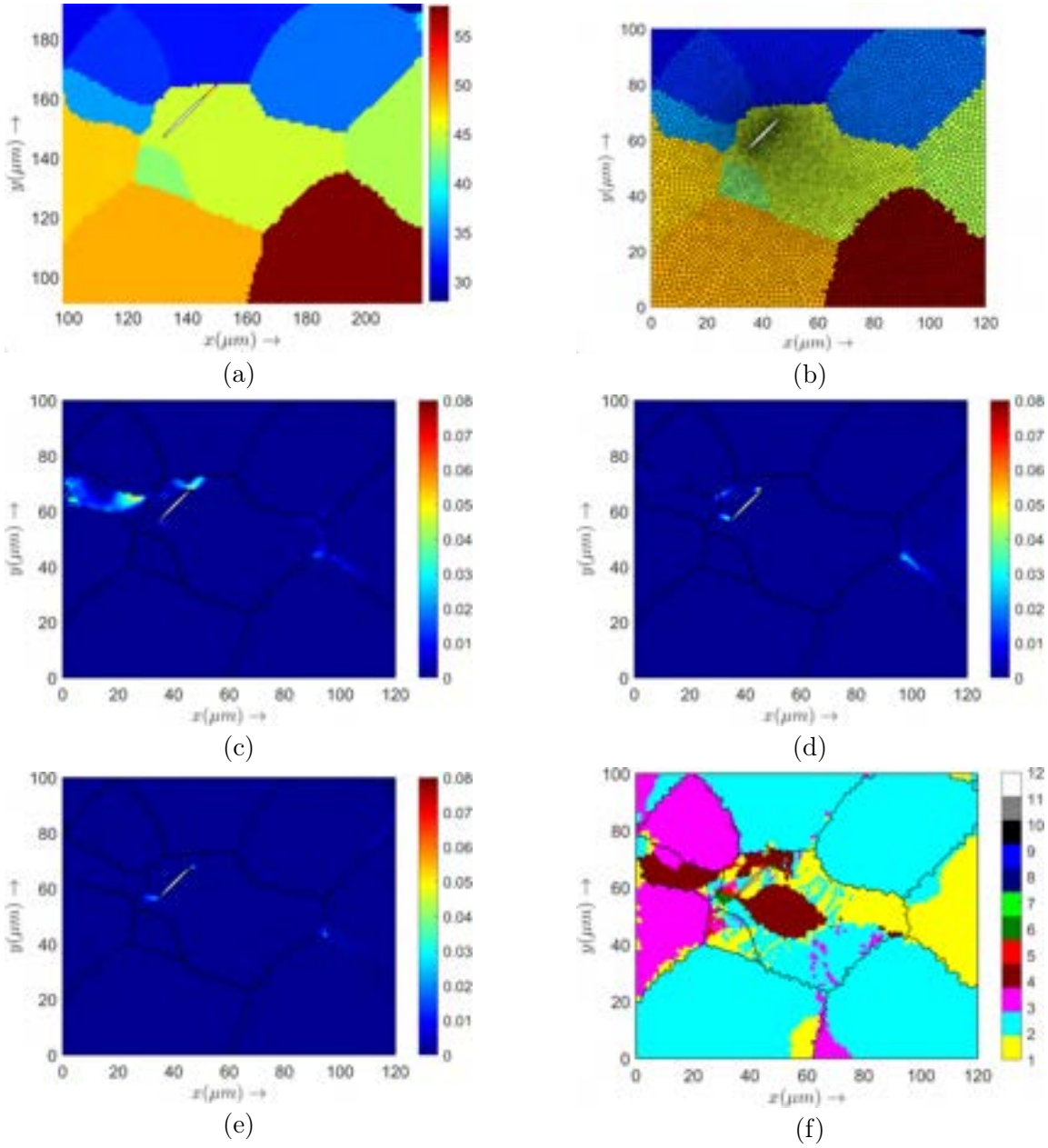

Figure 4.15: Accumulated slip variation of different slip systems : (a) microstructure for GB 3 with slip band trace, (b) Gmsh mesh containing 7635 elements, (c) Accumulated slip for prismatic 1, (d) Accumulated slip for prismatic 2, (e) Accumulated slip for prismatic 3, (f) Most active slip system ID map.

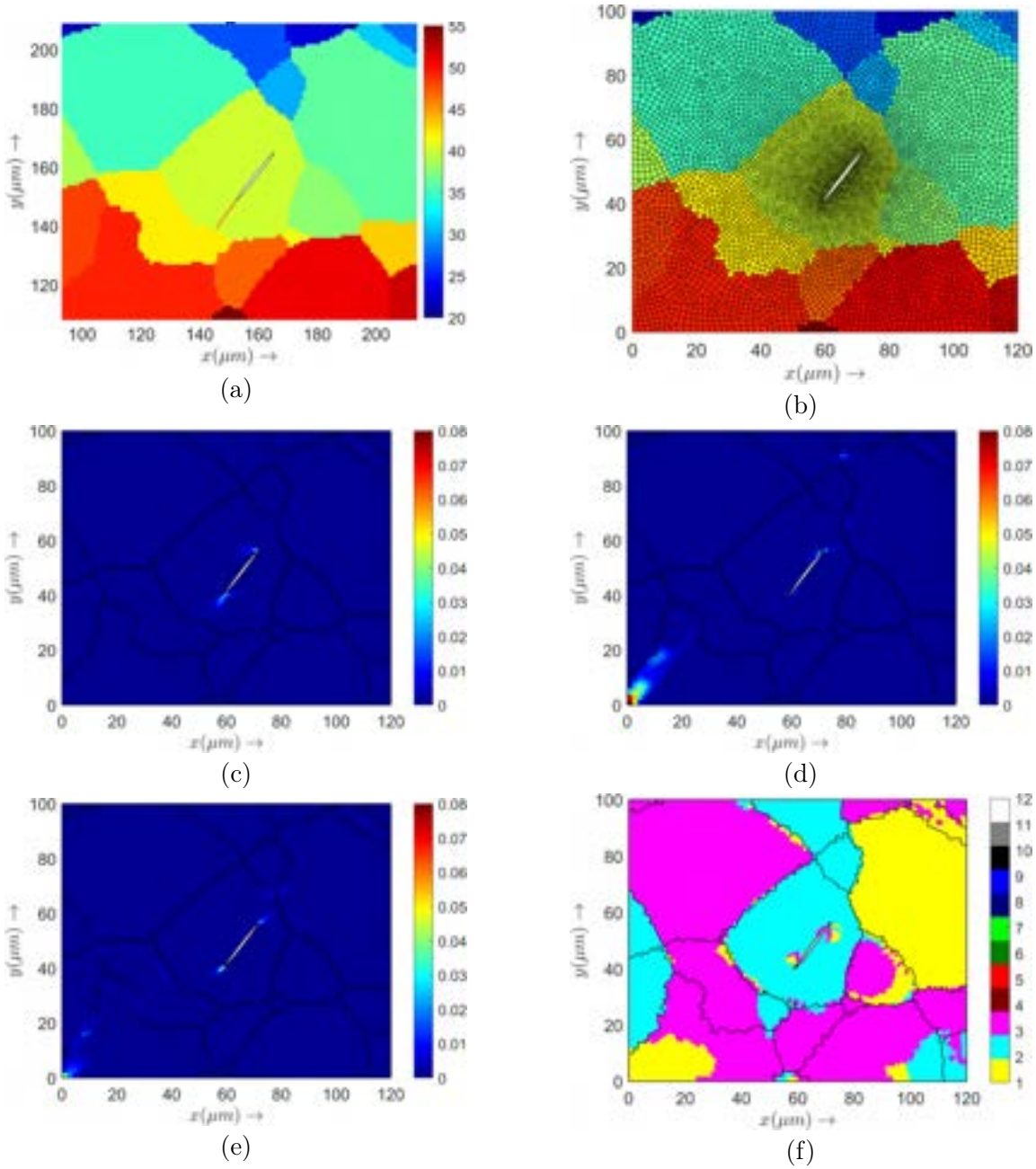

Figure 4.16: Accumulated slip variation of different slip systems : (a) microstructure for GB 4 with slip band trace, (b) Gmsh mesh containing 8118 elements, (c) Accumulated slip for prismatic 1, (d) Accumulated slip for prismatic 2, (e) Accumulated slip for prismatic 3, (f) Most active slip system ID map.

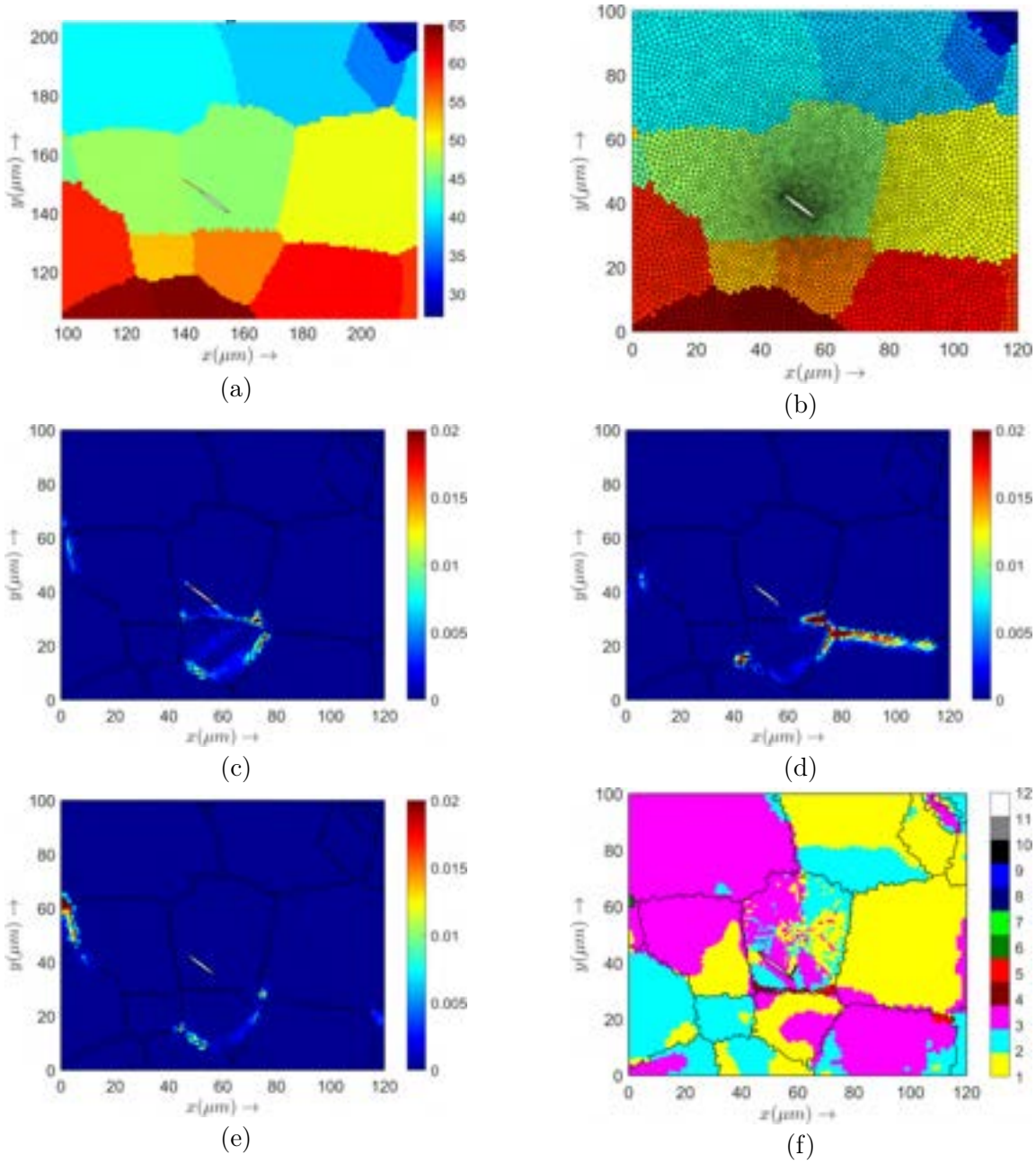

Figure 4.17: Accumulated slip variation of different slip systems : (a) microstructure for GB 5 with slip band trace, (b) Gmsh mesh containing 7479 elements, (c) Accumulated slip for prismatic 1, (d) Accumulated slip for prismatic 2, (e) Accumulated slip for prismatic 3, (f) Most active slip system ID map.

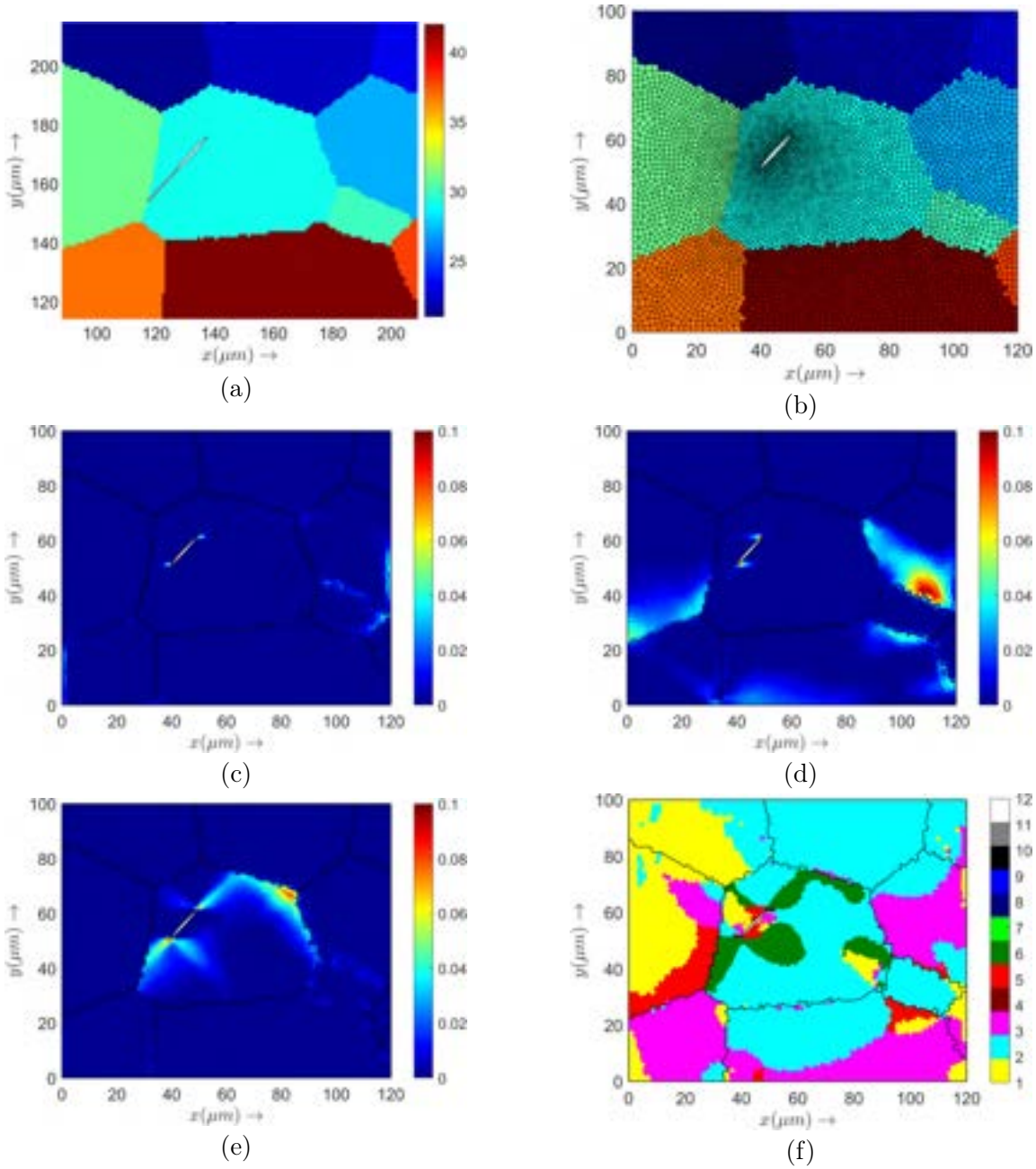

Figure 4.18: Accumulated slip variation of different slip systems : (a) microstructure for GB 6 with slip band trace, (b) Gmsh mesh containing 8042 elements, (c) Accumulated slip for prismatic 1, (d) Accumulated slip for prismatic 2, (e) Accumulated slip for prismatic 3, (f) Most active slip system ID map.

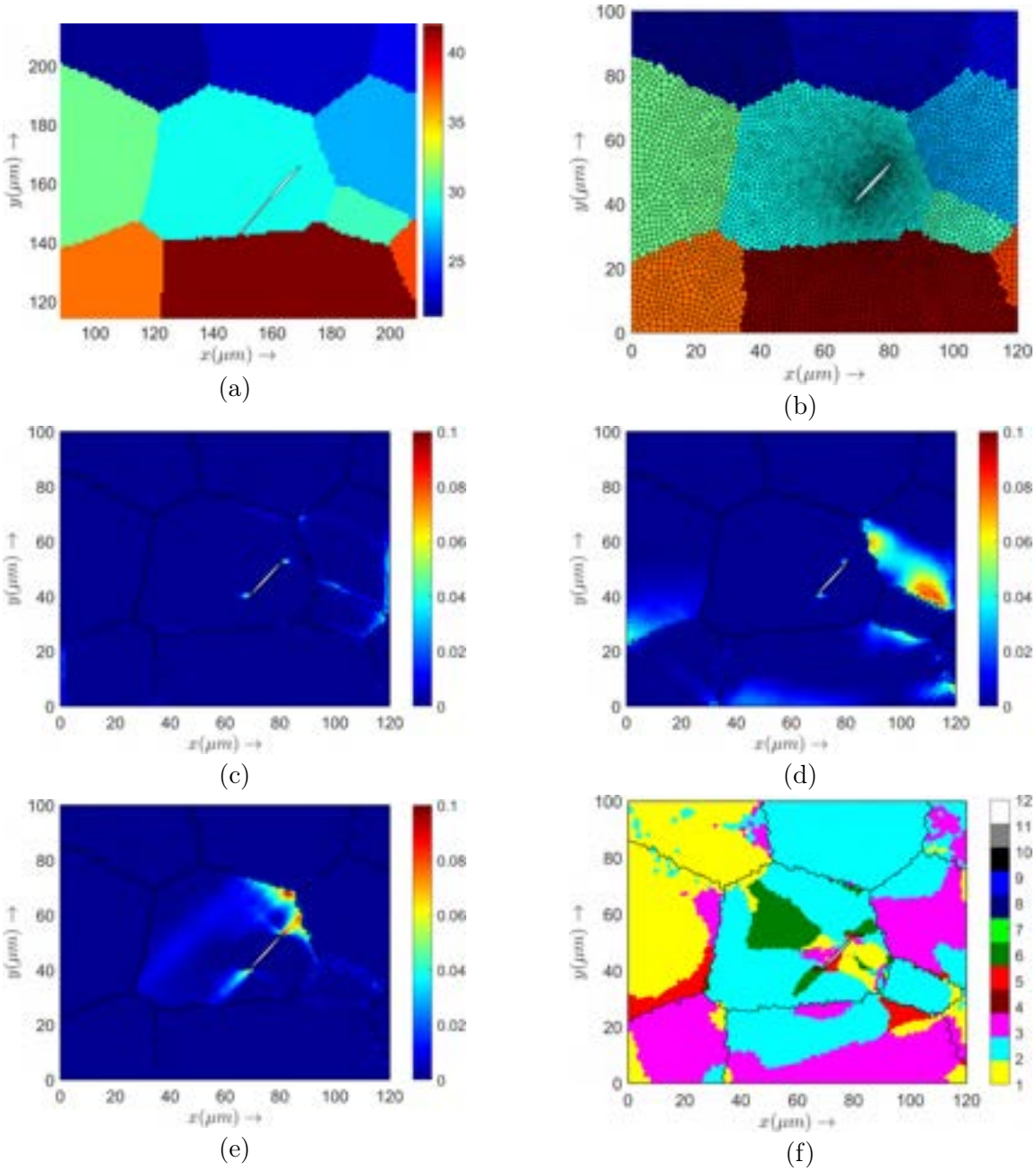

Figure 4.19: Accumulated slip variation of different slip systems : (a) microstructure for GB 7 with slip band trace, (b) Gmsh mesh containing 7799 elements, (c) Accumulated slip for prismatic 1, (d) Accumulated slip for prismatic 2, (e) Accumulated slip for prismatic 3, (f) Most active slip system ID map.

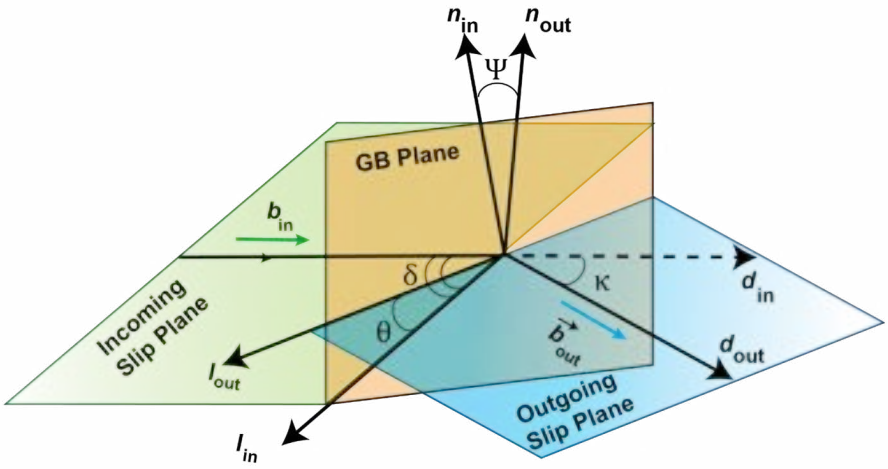

Figure 4.20: A schematic representative for slip transmission through a GB. $\vec{b}_{in}$: Burgers vector of the incoming slip system, $\vec{b}_{out}$: Burgers vector of the outgoing slip system, $\vec{n}_{in}$: Slip plane normal of the incoming slip system, $\vec{n}_{out}$: Slip plane normal of the outgoing slip system, $\vec{l}_{in}$: Intersection line of the incoming slip plane and GB, $\vec{l}_{out}$: Intersection line of the outgoing slip plane and GB, $\vec{d}_{in}$: Slip direction of the incoming slip system, $\vec{d}_{out}$: Slip direction of the outgoing slip system, θ: Angle between the two slip plane traces on the GB plane, κ: Angle between slip directions, ψ: Angle between slip plane normals, δ: Angle between the incoming slip direction and the incoming slip plane trace on the GB plane.

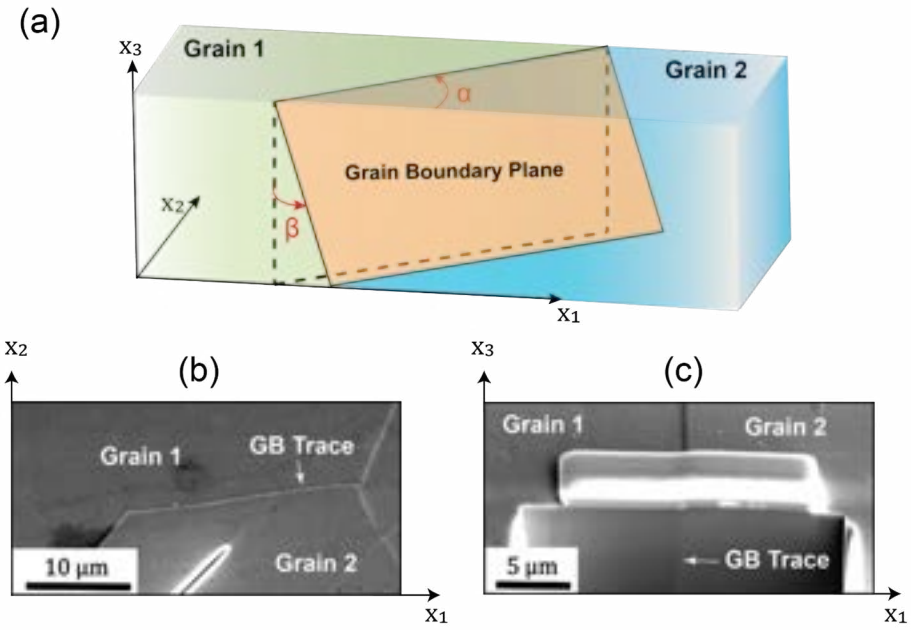

Figure 4.21: (a) Schematic representation of the GB plane. (b) The GB trace angle α is measured using the GB's plan view image (SEM image). (c) The GB plane angle β is measured using a cross-section of the GB after FIB removal of adjacent material.

GB ID	$\theta(\circ)$	$\kappa(\circ)$	$\psi(\circ)$	$\delta(\circ)$
1	65.89	69.94	63.26	27.48
2	70.22	88.33	88.35	9.64
3	80.95	70.06	65.53	26.67
4	79.26	59.01	53.72	49.29
5	47.36	47.53	40.92	59.65
6	43.92	31.10	22.73	86.94
7	87.95	70.54	72.79	58.48

Table 4.4: Relevant geometric quantities(angles) computed from the slip system and GB information to parametrize the micro-Hall-Petch parameter.

4.5. Parametrizing the micro-Hall-Petch parameter

Among the multitude of relationships that can be established between the micro-Hall-Petch parameter and the different angular quantities, we consider two particular GB metrics for the parametrization. We follow the procedure identical to the parametrization performed for the micro-Hall-Petch parameters for basal slip. Let m' denote either the LRB factor or LM factor, which we refer to as the compatibility factor since it is a measure of compatibility between adjacent grains - higher the value of m' greater the probability of slip transmission. Then we consider a simple empirical power-law dependence of the micro-Hall-Petch parameter on the compatibility factor

$$k_{\mu}^{\alpha} = K_{\mu}^{\alpha} \left(1 - m'\right)^{c^{\alpha}} \;\; ; \;\; c^{\alpha} > 0 \tag{4.7}$$

where K_μ^α is the micro-Hall-Petch multiplier and c^α is the micro-Hall-Petch exponent. Since a higher value of the micro-Hall-Petch parameter k_μ^α signifies higher blocking tendency of the GB to an incoming slip band, it is assumed to monotonically increase with the factor $1 - m'$ which signifies the loss of compatibility in some sense. c^α denotes the exponent appearing in the empirical power-law relationship. Performing a linear least-squares fit of $\log\left(k_\mu^\alpha\right)$ relative to $\log\left(1 - m'\right)$ yields the best fit micro-Hall-Petch multiplier and exponent, which is considered a material property since the GB dependence is now subsumed in m'. Figs. 4.22a- 4.22b depict the plots of the micro-Hall-Petch parameter against the corresponding metrics, i.e. the LRB factor and LM factor, respectively. The fit results in $K_\mu^\alpha = 687$ MPa $\mu m^{1/2}$, $c^\alpha = 1.83$ for the LRB factor and $K_\mu^\alpha = 699$ MPa $\mu m^{1/2}$, $c^\alpha = 1.07$ for the LM factor. It is interesting to note a close-to-linear relationship between micro-Hall-Petch parameter and $(1 - m')$ where m' is the LRB factor. Even though the parametrization of the micro-Hall-Petch parameter relative to the LRB factor is more appropriate, the parametrization relative to the LM factor is simple both in terms of ease of constructing the LM factor from experiments and in incorporating it in CPFE models where the GBs are not explicitly captured except in terms of shared faces between grains.

4.6. Conclusion

An integration between experimental measurements, dislocation pile-up theory, crystal plasticity simulations and some empirical modeling has been presented in order to determine the micro-Hall-Petch multiplier and exponent for prismatic slip, which are

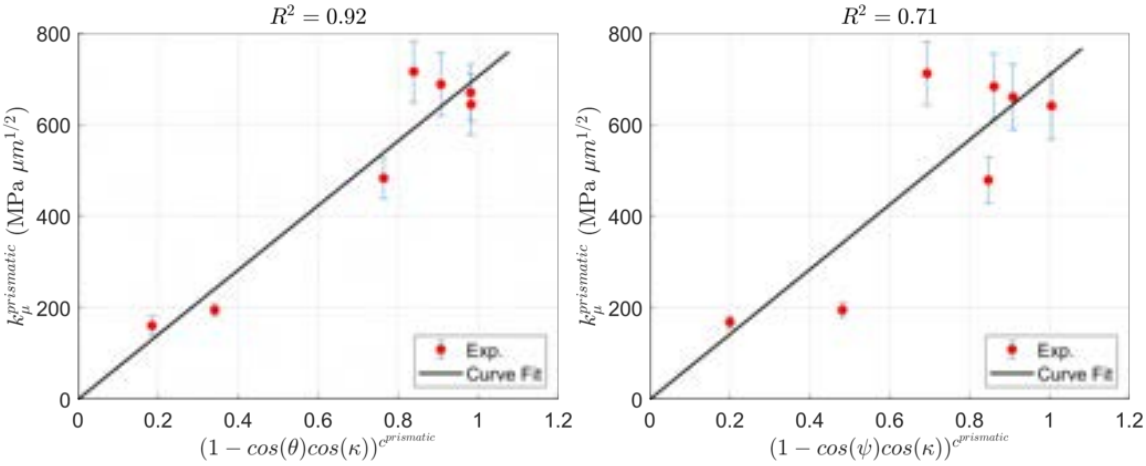

(a) (b)

Figure 4.22: (a) micro-Hall-Petch parameter plotted against $(1 - m')^{c^\alpha}$ where m' is the LRB factor, along with the linear fit. $K_\mu^\alpha = 687$ MPa $\mu m^{1/2}$, $c^\alpha = 1.83$. (b) micro-Hall-Petch parameter plotted against $(1 - m')^{c^\alpha}$ where m' is the LM factor, along with the linear fit. $K_\mu^\alpha = 699$ MPa $\mu m^{1/2}$, $c^\alpha = 1.07$.

material properties characterizing the dependence of the size-dependent contribution of the slip system resistance on certain GB parameters. First grains were identified in the microstructure to create notches to initiate prismatic slip since they possess relatively high critical resolved shear stress compared to basal slip. Subsequently, pile-up stress measurements were fit to a theoretical expression derived from continuum dislocation pile-up theory to obtain estimates of the micro-Hall-Petch parameter for seven different GBs. To parametrize the micro-Hall-Petch parameters relative to different metrics encoding the slip system information, CPFE simulations were conducted on neighborhoods of the GBs to obtain the the potential outgoing slip system(in the grain blocking the slip band). Using this information and GB inclination information two parametrizations were considered for the micro-Hall-Petch parameter relative to the LRB factor and LM factor based on an empirical power-law relationship. The

multiplier and exponents associated with the power-law furnish material parameters which encode the effect of the GB on the size-dependent contribution of the slip system resistance corresponding to prismatic slip.

CHAPTER V

Micro-Hall-Petch Modeling in PRISMS-CPFE

This chapter covers the implementation of the micro-Hall-Petch constitutive model into the PRISMS-CPFE code, followed by calibration of constitutive parameters and comparison with predictions using the original set of parameters obtained from integration of experiments, theory and simulations. The calibrated parameters are then used to perform some parametric studies to investigate the behavior this constitutive model.

5.1. Micro-Hall-Petch Constitutive Model

The incorporation of the micro-Hall-Petch constitutive model into crystal plasticity involves modification of the initial slip resistance using the micro-Hall-Petch equation :

$$s_0^\alpha = s_I^\alpha + s_S^\alpha = s_I^\alpha + \frac{k_\mu^\alpha}{\sqrt{d^\alpha}} \tag{5.1}$$

where s_0^α denotes the initial slip resistance associated with slip system α, decomposed into a grain size-independent contribution, s_I^α and a grain size-dependent contribution, s_S^α. The grain size-dependent contribution has a form similar to the classical Hall-Petch equation but extended to the slip system level where k_μ^α denotes the micro-Hall-Petch parameter and d^α is a measure of the slip system-level grain size. Chapters III and IV concluded with empirical expressions relating k_μ^α to different grain boundary metrics for basal and prismatic slip systems involving the micro-Hall-Petch multiplier and the micro-Hall-Petch exponent as the primary material properties. The computation of k_μ^α and d^α in the context of implementation within the crystal plasticity framework is detailed(illustrated in Fig. 5.1).

5.1.1. Computation of slip system-level grain size

Let's start with a microstructure discretized as a uniform grid of voxels with the grains identified by a set of grain identifiers(integers). Associated with each grain we also have the orientation information. Given this setup, the slip system-level grain size is computed in the following manner

1. Consider any particular voxel defined by it's centroidal coordinates $\boldsymbol{p}_c = (x_c, y_c, z_c)$ and the corresponding grain, G, it resides in. For this particular voxel, consider the slip system α with $\boldsymbol{m}^\alpha$ denoting the corresponding slip direction.

2. For grain G, identify its boundary ∂G, which is essentially represented as a collection of rectangular faces since the microstructure is represented as a uniform voxelated grid.

3. Find the point $\boldsymbol{p}_1$ on ∂G closest to point $\boldsymbol{p}_c$ along direction $\boldsymbol{m}^\alpha$ and denote this closest distance by d_1^α.

4. In a similar fashion, find the point $\boldsymbol{p}_2$ on ∂G closest to point $\boldsymbol{p}_c$ along direction $-\boldsymbol{m}^\alpha$ and denote this closest distance by d_2^α.

5. Define the slip system-level grain size, d^α for point $\boldsymbol{p}$ and slip system α as $d^\alpha = d_1^\alpha + d_2^\alpha$. A very similar methodology has been adopted by Nieto-Valeiras et al. [152], where the computed distances were used in dislocation-density evolution equations to study the effect of slip transfer at GBs on the strength of FCC polycrystals.

Conceptually, the slip system-level grain size for point $\boldsymbol{p}$ and slip system α denotes the smallest distance along the direction $\boldsymbol{m}^\alpha$ subtended by the corresponding grain boundary. We note that this is a heterogeneous property varying throughout the microstructure and can be computed apriori with the knowledge of the microstructural points and orientations alone.

5.1.2. Computation of micro-Hall-Petch parameter

The micro-Hall-Petch parameter was related to different grain boundary metrics defined based on the slip systems in neighboring grains and the grain boundary inclination. While the grain boundary inclination is an important part of this characterization it is not particularly well-suited for implementation into crystal plasticity models involving discretized microstructures for the following reasons

1. Most of the commonly used synthetic microstructure generation softwares do

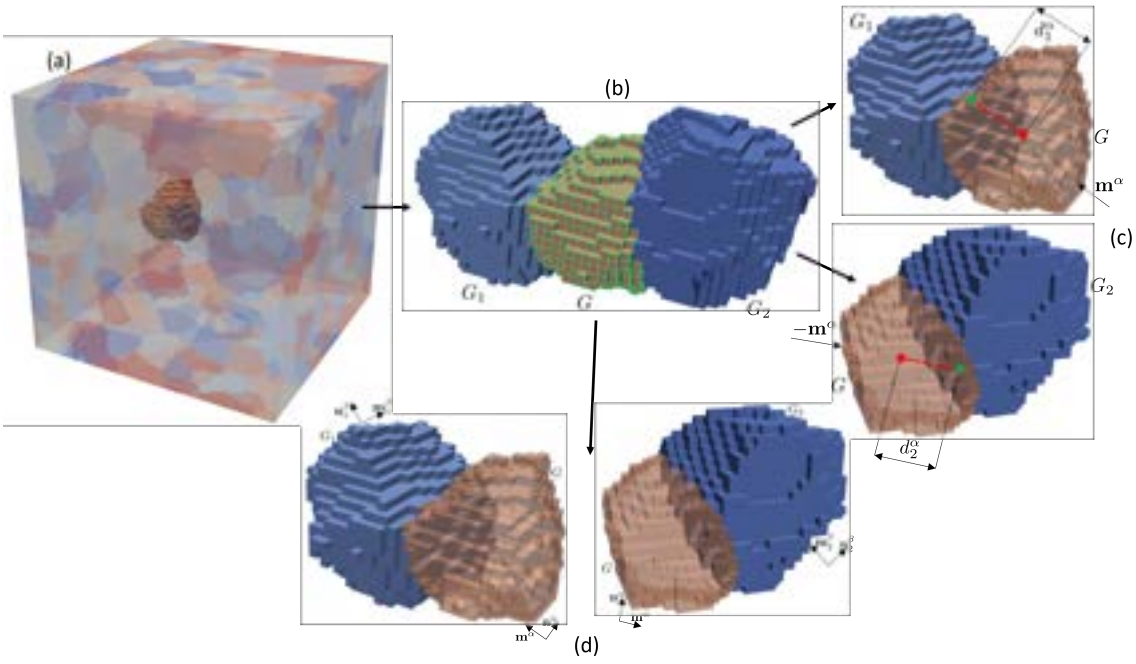

Figure 5.1: Illustration depicting the computation of d^α and k_μ^α. (a) Uniform voxelated microstructure (b) For any microstructural point in grain G and line passing through it with slip direction $\boldsymbol{m}^\alpha$, find the neighboring grains G_1 and G_2 based on the points of intersection of the line with the boundary. (c) The slip system level grain size d^α is computed for every point in the microstructure by finding the length of the line segment passing through that point connecting the two points on the grain boundary along direction $\boldsymbol{m}^\alpha$. (d) To compute k_μ^α the primary quantity is the maximum compatibility factor which is computed using the knowledge of slip systems corresponding to the neighboring grains G_1 and G_2.

not possess the functionality to include statistical information associated with grain boundary inclinations as an input to the microstructure generation engines.

2. The grain boundary inclination is dependent on how the microstructure is meshed and while two microstructures might be quite similar in their description, depending on how those microstructures are meshed, the grain boundary inclination can be different. This is also evident in that a package like DREAM.3D generates voxelated meshes where the grain boundary face normals can only be aligned with one of the three sample axes, while a software like Neper generates polyhedra where different faces of a grain can be oriented differently.

As noted earlier, the angles θ and δ depend on the grain boundary inclination while ψ and κ do not. Then we parametrize the micro-Hall-Petch parameter on the grain boundary metrics through the angles ψ and κ as follows :

$$k_{\mu}^{\alpha} = K_{\mu}^{\alpha} \left(1 - \cos(\psi)\cos(\kappa)\right)^{c^{\alpha}} \tag{5.2}$$

where K_{μ}^{α} is the micro-Hall-Petch multiplier and c^{α} is the micro-Hall-Petch exponent, both of which are constants for a particular material. Note that the quantity $\cos(\psi)\cos(\kappa)$ is commonly referred to as the Luster-Morris factor motivated from earlier studies [143, 138] on slip transmission. Then k_{μ}^{α} is computed as follows :

1. In the process of computing d^{α} we had identified the points $\boldsymbol{p}_1$ and $\boldsymbol{p}_2$ lying on the grain boundary. Using this information we identify the neighboring grains

sharing these points with grain G. Denote by G_1 and G_2 those grains sharing points $\boldsymbol{p}_1$ and $\boldsymbol{p}_2$, respectively, with grain G.

2. Define $\psi_1^{\alpha\beta}$ as the angle satisfying the relation $\cos\left(\psi_1^{\alpha\beta}\right) = \boldsymbol{n}^{\alpha} \cdot \boldsymbol{n}_1^{\beta}$ where $\boldsymbol{n}^{\alpha}$ is the slip plane normal corresponding to slip system α and $\boldsymbol{n}_1^{\beta}$ is the slip plane normal corresponding to slip system β in G_1.

3. Define $\kappa_1^{\alpha\beta}$ as the angle satisfying the relation $\cos\left(\kappa_1^{\alpha\beta}\right) = \boldsymbol{m}^{\alpha} \cdot \boldsymbol{m}_1^{\beta}$ where $\boldsymbol{m}^{\alpha}$ is the slip direction corresponding to slip system α and $\boldsymbol{m}_1^{\beta}$ is the slip direction corresponding to slip system β in G_1.

4. Compute the quantity μ_1^{α} obtained by maximizing $\left|\cos\left(\kappa_1^{\alpha\beta}\right)\cos\left(\psi_1^{\alpha\beta}\right)\right|$ over all admissible slip systems in G_1, i.e., $\mu_1 = \max_{\beta}\left|\cos\left(\kappa_1^{\alpha\beta}\right)\cos\left(\psi_1^{\alpha\beta}\right)\right|$. Here $|\cdot|$ denotes the absolute value of the argument.

5. Define $\psi_2^{\alpha\beta}$ as the angle satisfying the relation $\cos\left(\psi_2^{\alpha\beta}\right) = \boldsymbol{n}^{\alpha} \cdot \boldsymbol{n}_2^{\beta}$ where $\boldsymbol{n}^{\alpha}$ is the slip plane normal corresponding to slip system α and $\boldsymbol{n}_2^{\beta}$ is the slip plane normal corresponding to slip system β in G_2.

6. Define $\kappa_1^{\alpha\beta}$ as the angle satisfying the relation $\cos\left(\kappa_2^{\alpha\beta}\right) = \boldsymbol{m}^{\alpha} \cdot \boldsymbol{m}_2^{\beta}$ where $\boldsymbol{m}^{\alpha}$ is the slip direction corresponding to slip system α and $\boldsymbol{m}_2^{\beta}$ is the slip direction corresponding to slip system β in G_2.

7. Compute the quantity μ_2^{α} obtained by maximizing $\left|\cos\left(\kappa_2^{\alpha\beta}\right)\cos\left(\psi_2^{\alpha\beta}\right)\right|$ over all admissible slip systems in G_2, i.e., $\mu_2 = \max_{\beta}\left|\cos\left(\kappa_2^{\alpha\beta}\right)\cos\left(\psi_2^{\alpha\beta}\right)\right|$. Here $|\cdot|$ denotes the absolute value of the argument.

8. Define $\mu^\alpha \coloneqq \max(\mu_1^\alpha, \mu_2^\alpha)$, which we refer to as the maximum compatibility factor for the point under consideration for slip system α. Then compute $k_\mu^\alpha = k_\mu^\alpha(1-\mu^\alpha)^{c^\alpha}$.

Identical to d^α, k_μ^α is a heterogeneous property varying throughout the microstructure for different slip systems. Conceptually, this is based on the hypothesis that the slip system in the neighboring grain used to compute the relevant metrics is the one that is in some sense best aligned with the slip system in the grain of interest. We now cover aspects about synthetic microstructure generation using experimental data and subsequent calibration of crystal plasticity constitutive parameters.

5.2. Synthetic Microstructure Generation

Here we outline the procedure for generating synthetic microstructures which we use for all our forthcoming simulation studies. This microstructure information is passed as an input to the preprocessing step detailed earlier to compute the slip system-level grain size and micro-Hall-Petch parameter for all voxels in the microstructure.

We use DREAM.3D for generating synthetic microstructures given certain input statistics. The primary inputs supplied to DREAM.3D are the orientation information in terms of crystallographic texture, and the grain size information in terms of the grain size distribution. As input from experiments, we have a 2D section of the EBSD data in the form of an orientation image map. This data is read in MATLAB using MTEX toolbox which stores the relevant data - the positions and crystallographic orientation of the all pixels constituting the 2D section. The orientation data is then output in the form of Bunge Euler angles to a text file which can be read

into DREAM.3D.

Using the pixel position information we then compute the 2D grain size, which is the equivalent area circle diameter, i.e., the diameter of the circle encompassing the same area as the grain. Since the 2D dataset also contains grains on the boundary which are truncated, and hence their grain size is underestimated. To prevent this we only use the 2D grain size information from grains which are completely contained within the 2D section without being intercepted by the boundaries. It is important to note here that the 2D grain size is not a true representation of the grain size for that grain. This is apparent since the 2D grain size is computed based on a 2D section of a 3D grain. In other words, the 2D grain size is also a lower estimate on the actual grain size that is required as input to the micro-Hall-Petch preprocessor which computes the slip system-level grain sizes for a 3D microstructure. To address this problem we employ the Saltykov method [153, 154, 155, 156] to obtain an estimate of the 3D grain size distribution. In the context of microstructures, the Saltykov method is particularly well-suited when grains are equiaxed, which is a fairly good approximation for the microstructures considered for our study. The output from the Saltykov method implementation is a histogram bin data - the centers of the histogram bins representing a particular 3D grain size, and the height of the bins denoting the fraction of grains with a 3D grain size belonging to that bin with a particular width. Since the grain size input to DREAM.3D is parameters of a standard lognormal distribution, the 3D grain size histogram dataset is fit with a standard lognormal distribution yielding the best fit parameters - the mean and standard deviation of the natural logarithm of the random variable. The standard

lognormal probability distribution function takes the form

$$P(X) = \frac{1}{x\bar{\sigma}\sqrt{2\pi}}\exp\left(-\frac{(\ln(x)-\bar{\mu})^2}{2\bar{\sigma}^2}\right) \tag{5.3}$$

where $\bar{\mu}$ and $\bar{\sigma}$ are the mean and standard deviation of the natural logarithm of the random variable, X. We apply the Saltykov method of unfolding the 2D grain distribution using **GrainSizeTools** [157], an open-source Python script for grain size analysis and paleopiezometry. The orientation data and 3D lognormal distribution parameters are then fed to a DREAM.3D pipeline to generate a synthetic microstructure represented as a uniform grid of voxels(illustrated in Fig. 5.2).

5.3. Calibration of constitutive parameters

The crystal plasticity constitutive model is calibrated with nine stress-strain curves obtained from experimental mechanical tests. These nine stress-strain curves correspond to different texture-loading direction-grain size combinations noted below :

1. Samples corresponding to Texture 1(Fig. 5.3(a)) with three different grain size distributions were deformed along the z-direction under tension with periodic boundary constraints to a strain of 1 %.

2. Samples corresponding to Texture 2(Fig. 5.3(b)) with three different grain size distributions were deformed along the z-direction under tension with periodic boundary constraints to a strain of 0.35%.

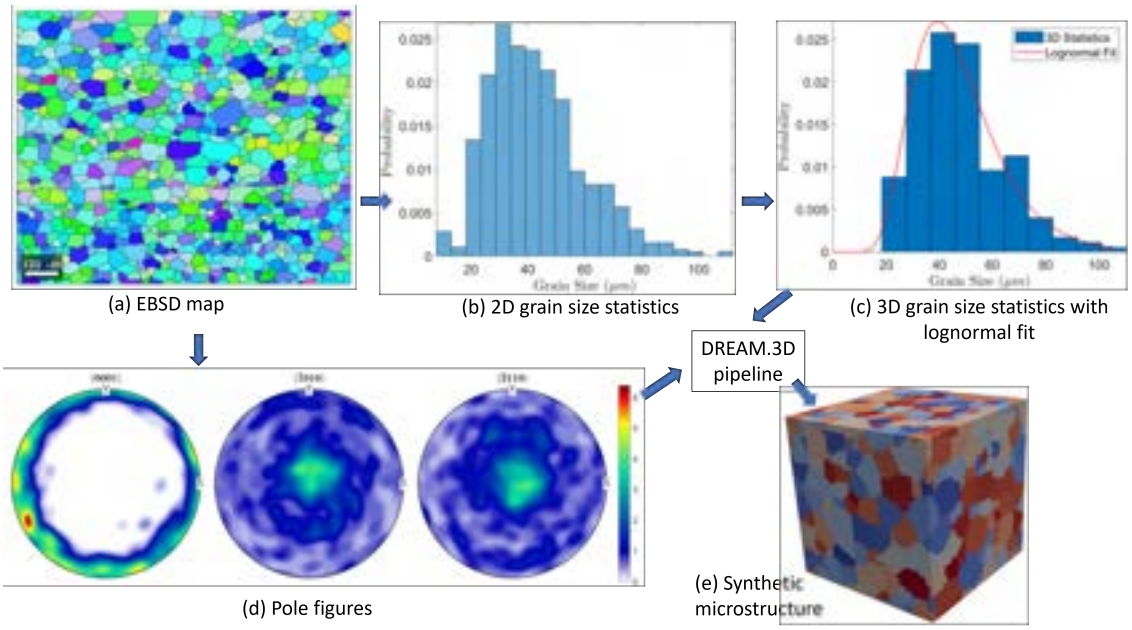

Figure 5.2: Illustration depicting the workflow for synthetic microstructure generation in DREAM.3D. (a) 2D microstructure section from experiment, (b) 2D grain size statistics extracted from microstructure section not including boundary grains, (c) Use Saltykov method to obtain 3D grain size statistics and fit it with lognormal distribution, (d) Pole figures from experimental texture data, (e) Use best-fit lognormal distribution parameters and orientation information as input to DREAM.3D to generate synthetic microstructure.

3. Samples corresponding to Texture 2(Fig. 5.3(b)) with three different grain size distributions were deformed along the x-direction under tension with periodic boundary constraints to a strain of 1%.

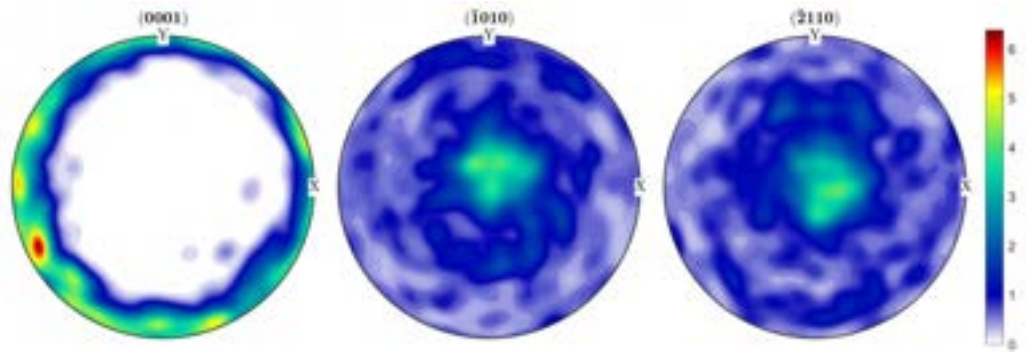

(a)

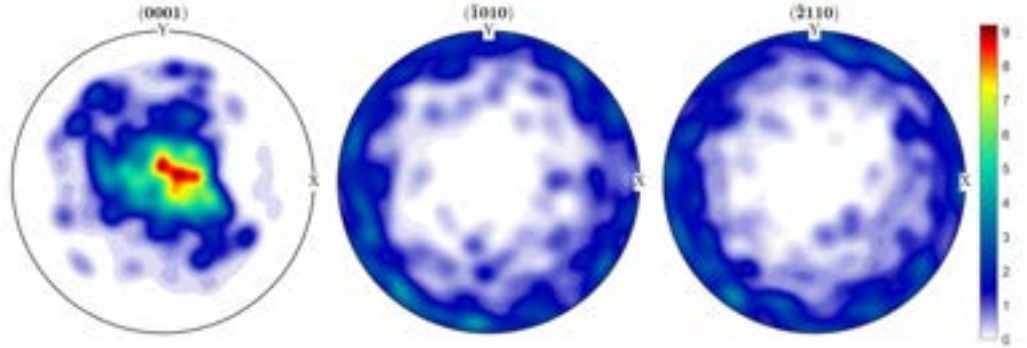

(b)

Figure 5.3: Pole figures for (a) Texture 1, and (b) Texture 2.

Then following the procedure outlined in the previous section, microstructures were generated for these nine cases using DREAM.3D with inputs being the texture and 3D grain size distribution, which were obtained from microstructure sections available for all the cases. We note that only six synthetic microstructures were generated since there are in total two texture combinations with three grain sizes per texture. The remaining three cases involve simply a change in the loading direction so that

new microstructures were required to be generated. The six microstructures are represented as a 50 x 50 x 50 uniform voxelated grid consisting of approximately 500 grains. The best-fit lognormal distribution parameters are included in Table 5.1 along with the measure of 2D grain size commonly used, i.e., the grain area average size. The grain area average size is computed for the 2D microstructural section by computing the weighted average of the grain sizes with the grain area playing the role of the weights.

Texture	Average size (μm)	$\bar{\mu}$	$\bar{\sigma}$
Texture 1	55	3.796	0.351
Texture 1	187	5.103	0.255
Texture 1	333	5.387	0.633
Texture 2	68	3.707	0.587
Texture 2	227	5.168	0.329
Texture 2	343	5.556	0.425

Table 5.1: Grain size information for the six different texture-grain size distribution cases.

All crystal plasticity simulations are setup considering 12 slip systems - 3 basal, 3 prismatic, 6 pyramidal <c+a> - and 6 extension twin systems. The elastic stiffness constants for Mg-4Al have been adopted from earlier work [150, 151] - $C_{11} = 59.4$ GPa, $C_{33} = 61.6$ GPa, $C_{12} = 25.61$ GPa, $C_{13} = 21.44$ GPa and $C_{44} = 16.4$ GPa. In the hardening law, the latent hardening coefficient was set to $q = 1.0$, while the flow rule parameters were $\dot{\gamma}_0 = 0.001s^{-1}$ and $m = 34$. Additionally, for all simulations

the micro-Hall-Petch coefficients are set to specific values - c^{α} for basal = 0.6 and c^{α} for prismatic = 1.07 - based on Chapter III and Chapter IV, respectively. We also set the slip resistance for the pyramidal $< c + a >$ slip systems to 140 MPa without any hardening. For the scenarios studied in this work, the primary slip systems are basal and prismatic with some role played by twinning. While we have a micro-Hall-Petch model for basal and prismatic slip, we account for the size effect from twinning via a simple Hall-Petch type modification to the slip resistance. In this modification, the twinning resistance s^t is expressed as $s^t = s_0^t + K^t/\sqrt{d_{eq}}$, where s_0^t is the size-independent contribution of the slip resistance, while the additional term $K^t/\sqrt{d_{eq}}$ accounts for the size-dependent contribution with d_{eq} denoting the average grain size based on the lognormal distribution. We refer to K^t as the twinning Hall-Petch coefficient. Nine parameters are considered as free parameters for calibration purpose - the micro-Hall-Petch multipliers, slip resistances and hardening coefficient for basal and prismatic, the twinning Hall-Petch coefficient, slip resistance and hardening coefficient.

Figs. 5.4(a)-5.4(c) depict the stress-strain curve comparison between CPFE simulations and experiments for all nine cases considered after calibration. The calibrated parameters are included in Table 5.2. Figs. 5.5(a)-5.5(c) depict the yield stress, σ_Y plotted against the corresponding inverse square-root of grain size, $1/\sqrt{d}$ based on the simulations with the calibrated parameters. The yield stress for all cases is defined as the 0.2% offset, and the Hall-Petch intercept, σ_0 and Hall-Petch slope, K_{HP} are the intercept and slope, respectively, of the corresponding linear least-squares fit from σ_Y vs $1/\sqrt{d}$ dataset. It is important to note that in the σ_Y vs $1/\sqrt{d}$ plots,

d refers to the grain area average grain size computed from the corresponding 2D dataset, since this is the measure of grain size that has been traditionally used in such plots. Table 5.3 shows the comparison between the Hall-Petch coefficients for the three texture-loading direction cases considered.

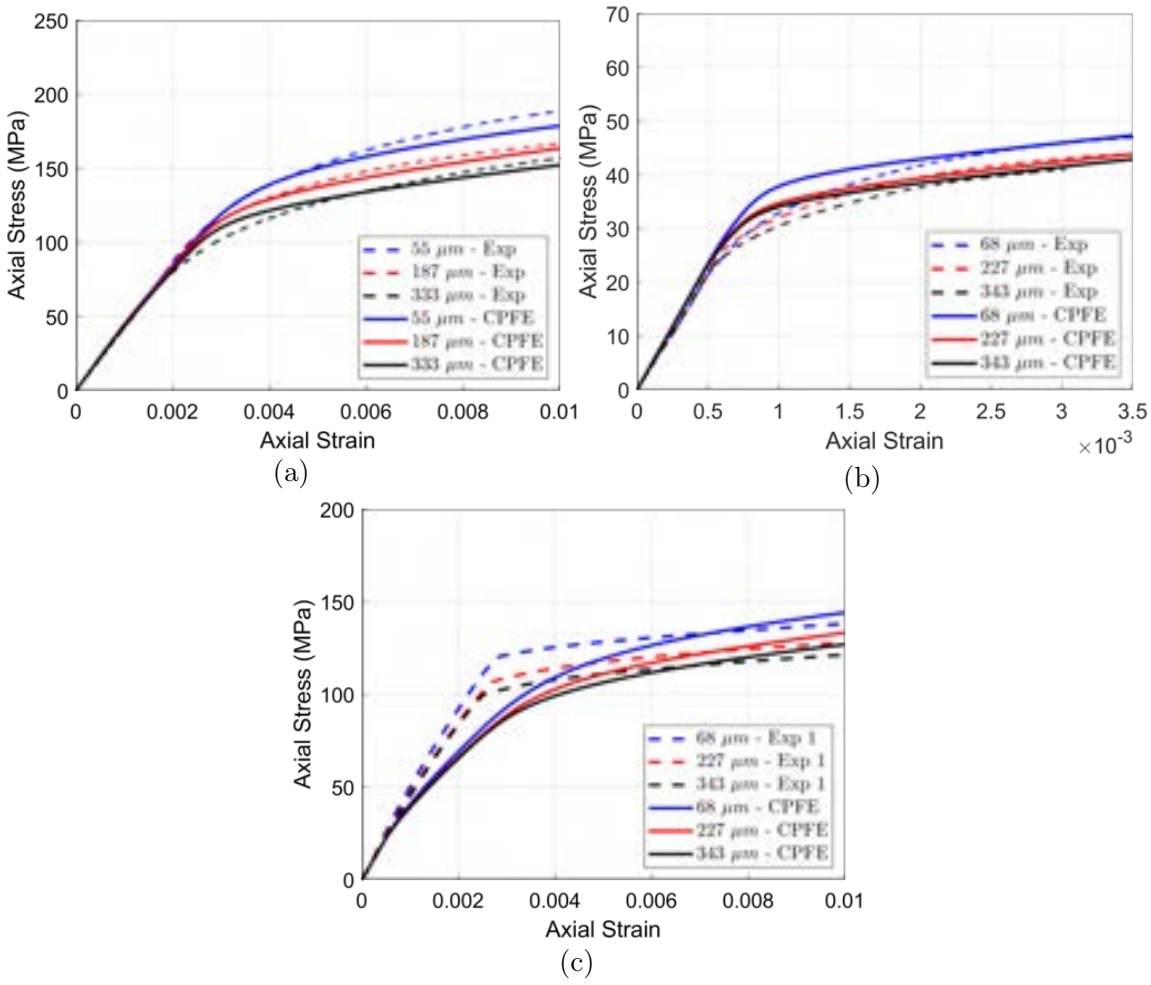

Figure 5.4: Stress-strain curve comparison between CPFE simulations and experiments using calibrated parameters for (a) Texture 1, z-direction loading, (b) Texture 2, z-direction loading and (c) Texture 2, x-direction loading.

Deformation mode	s_0^α(MPa)	h_0^α(MPa)	s_s^α(MPa)	a^α	K_μ^α (MPa $\mu m^{1/2}$)	c^α
Basal	9.3	300	150	1.0	60	0.6
Prismatic	51	600	150	1.0	1000	1.07
Pyramidal	140	0	200	1.0	0	0
Twin	17.5	500	100	1.0	25	0

Table 5.2: Calibrated micro-Hall-Petch crystal plasticity constitutive model parameters for Mg-4Al.

Hall-Petch coefficient	Texture 1, z-direction loading : Exp.	Texture 1, z-direction loading : CPFE	Texture 2, z-direction loading : Exp.	Texture 2, z-direction loading : CPFE
σ_0(MPa)	110.06	112.59	37.66	37.52
K_{HP}(MPa $\mu m^{1/2}$)	372.42	308.36	69.44	68.96

Hall-Petch coefficient	Texture 2, x-direction loading : Exp.	Texture 2, x-direction loading : CPFE
σ_0(MPa)	97.44	91.84
K_{HP}(MPa $\mu m^{1/2}$)	254.62	200.52

Table 5.3: Comparison of Hall-Petch coefficients for the three texture-loading direction cases between CPFE simulations and experiments, using the calibrated parameters.

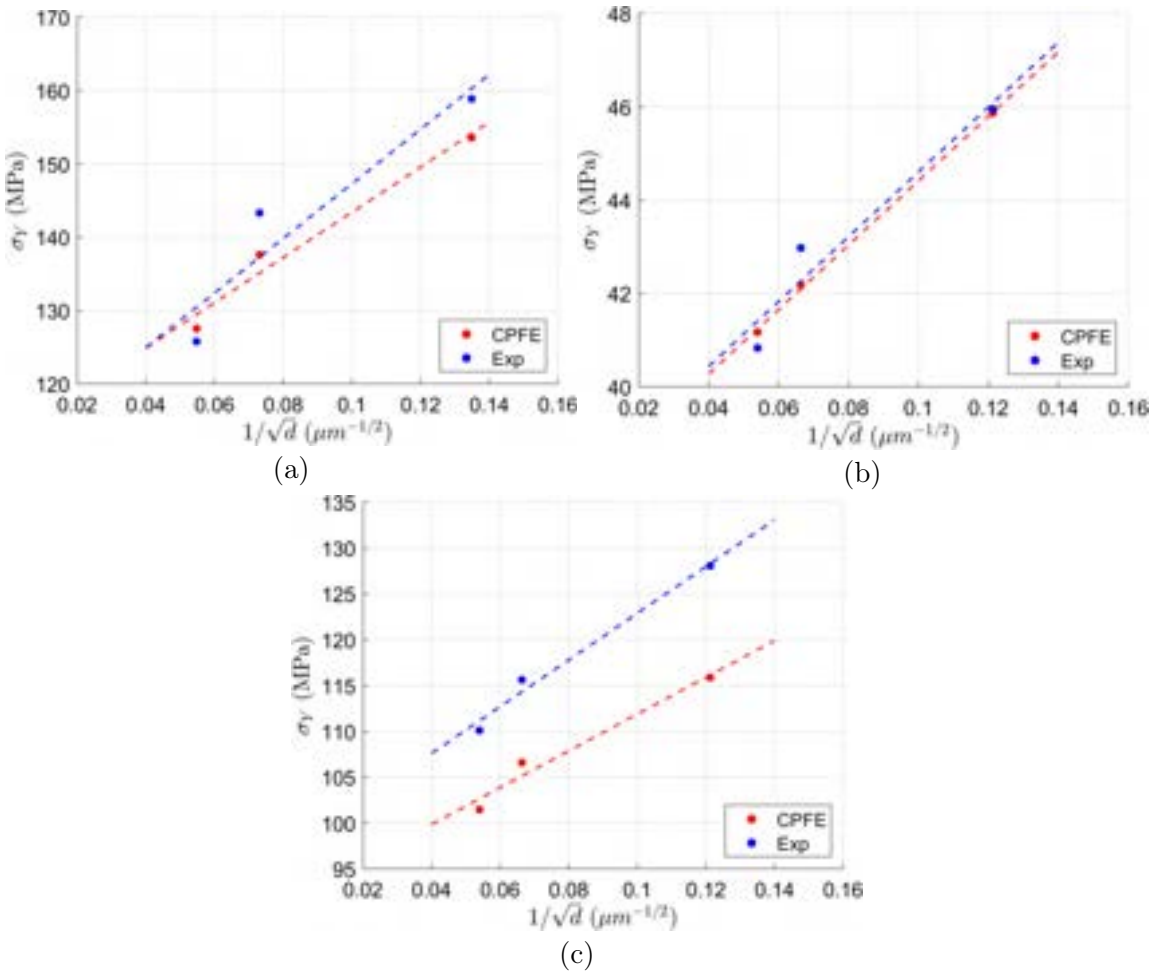

Figure 5.5: Yield stress(σ_Y) vs inverse square-root grain size($1/\sqrt{d}$) comparison between CPFE simulations and experiments using calibrated parameters for (a) Texture 1, z-direction loading, (b) Texture 2, z-direction loading and (c) Texture 2, x-direction loading. Dotted lines denote corresponding linear least-squares fit.

Figs. 5.6(a)-5.6(c) depict the stress-strain curve comparison between CPFE simulations and experiments for all nine cases with the original parameters(Table 5.4) obtained from experiments as noted in Chapter III and Chapter IV. The only parameters modified here are the basal and prismatic slip resistances and micro-Hall-Petch multipliers to the original parameters, while the rest of the parameters are set identical to the calibrated parameters in Table 5.2. It is interesting to note that even though the stress-strain curves don't all match with a single parameter set, they produce quite reasonable stress-strain curves. This is especially considering the fact that the slip resistance values used here were fed to dislocation pile-up models, and the micro-Hall-Petch coefficients were then obtained from localized pile-up stress measurements ahead of slip bands blocked by grain boundaries. Figs. 5.7(a)-5.7(c) depict the yield stress plotted against the corresponding inverse square-root of grain size based on the simulations with the original parameters. Table 5.5 shows the comparison between the Hall-Petch coefficients for the three texture-loading direction cases between experiments and CPFE simulations with the original parameters.

Deformation mode	s_0^α(MPa)	h_0^α(MPa)	s_s^α(MPa)	a^α	K_μ^α (MPa $\mu m^{1/2}$)	c^α
Basal	4.34	300	150	1.0	159	0.6
Prismatic	42.54	600	150	1.0	699	1.07
Pyramidal	140	0	200	1.0	0	0
Twin	17.5	500	100	1.0	25	0

Table 5.4: Original micro-Hall-Petch crystal plasticity constitutive model parameters for Mg-4Al. The original parameters here only refer to the basal and prismatic slip resistances and micro-Hall-Petch multipliers while the remaining parameters are retained as is for the simulations.

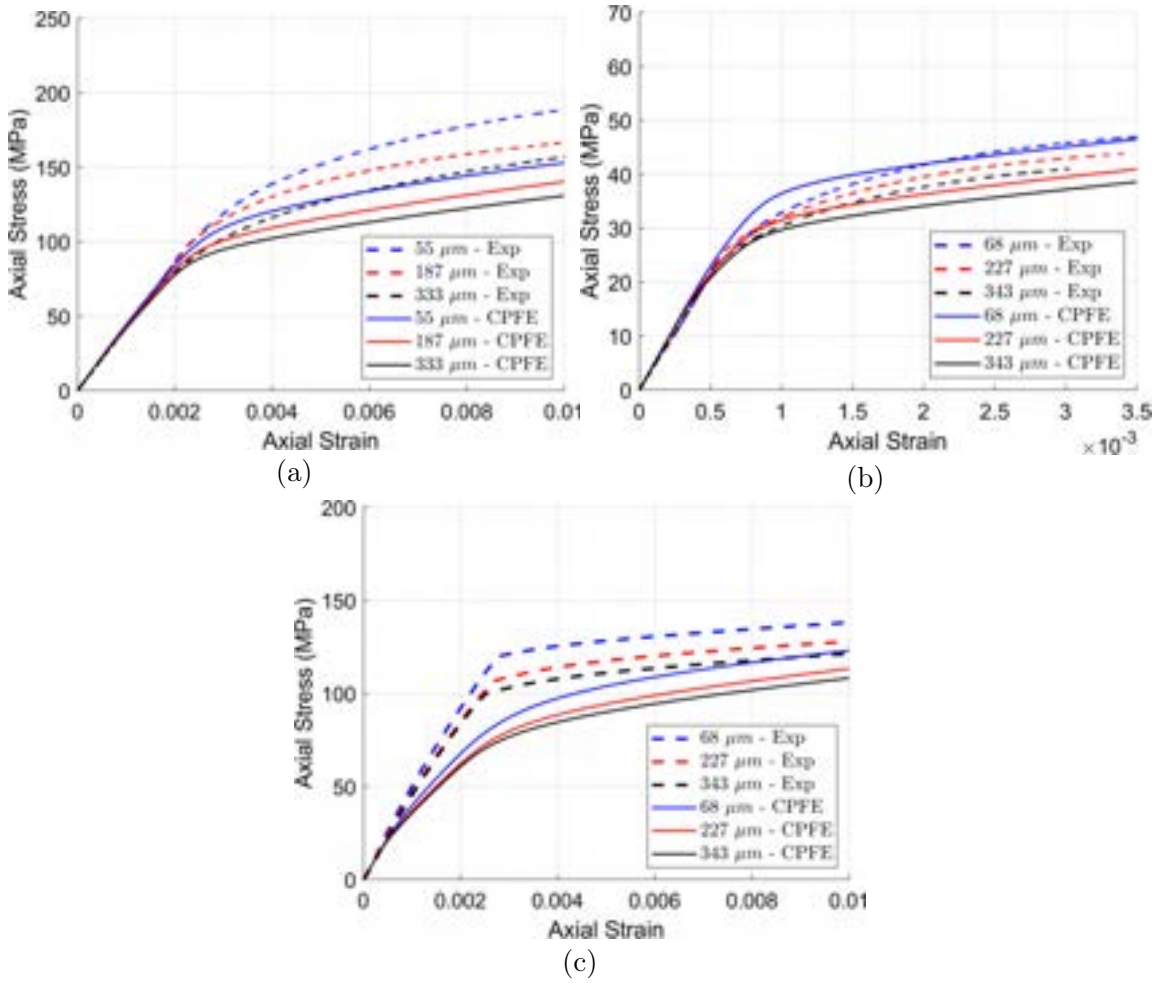

Figure 5.6: Stress-strain curve comparison between CPFE simulations and experiments using the original parameters for (a) Texture 1, z-direction loading, (b) Texture 2, z-direction loading and (c) Texture 2, x-direction loading.

Hall-Petch coefficient	Texture 1, z-direction loading : Exp.	Texture 1, z-direction loading : CPFE	Texture 2, z-direction loading : Exp.	Texture 2, z-direction loading : CPFE
σ_0(MPa)	110.06	91.02	37.66	30.55
K_{HP}(MPa $\mu m^{1/2}$)	372.42	267.96	69.44	120.07

Hall-Petch coefficient	Texture 2, x-direction loading : Exp.	Texture 2, x-direction loading : CPFE
σ_0(MPa)	97.44	73.06
K_{HP}(MPa $\mu m^{1/2}$)	254.62	216.77

Table 5.5: Comparison of Hall-Petch coefficients for the three texture-loading direction cases between CPFE simulations and experiments, using the original parameters from Chapter III and Chapter IV.

We note that the calibrated values of the basal and prismatic slip resistances and micro-Hall-Petch multipliers(Table 5.2) are not in agreement with the original values(Table 5.4). The calibrated basal slip resistance is about twice that of the original basal slip resistance, which was adopted from Akhtar et al. [137] who studied the substitutional solution hardening of magnesium single crystals with different alloying elements. The higher calibrated value indicates additional factors contributing to the initial slip resistance(without size effect contribution) possibly stemming from the underlying defect microstructure in the polycrystalline sample. The calibrated

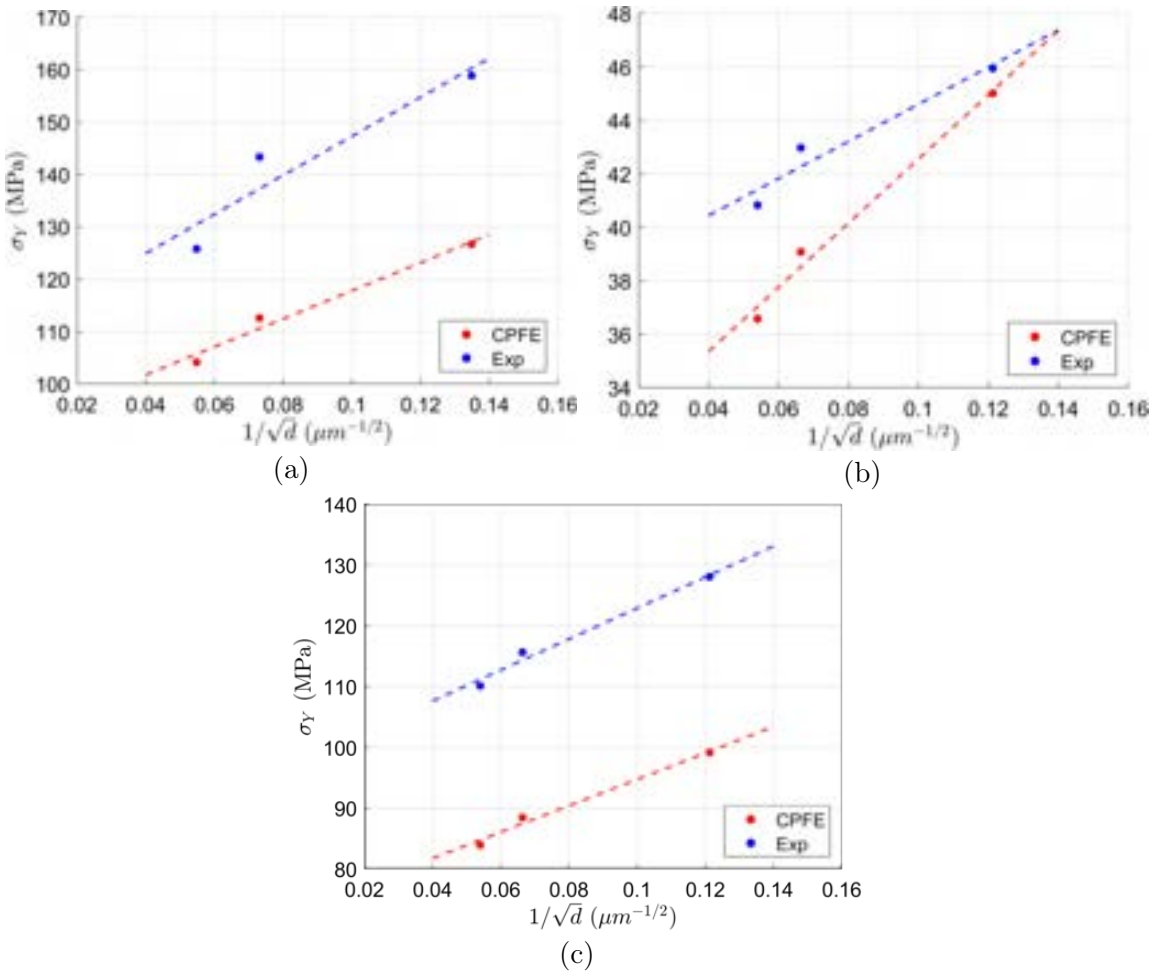

Figure 5.7: Yield stress(σ_Y) vs inverse square-root grain size($1/\sqrt{d}$) comparison between CPFE simulations and experiments using the original parameters for (a) Texture 1, z-direction loading, (b) Texture 2, z-direction loading and (c) Texture 2, x-direction loading. Dotted lines denote corresponding linear least-squares fit.

prismatic slip resistance is however, not very different from original prismatic slip resistance because the original values were estimated from yield stress of polycrystalline stress-strain curves rather than studies on single crystals.

The calibrated basal micro-Hall-Petch multiplier is about 0.4 times that of the original basal micro-Hall-Petch multiplier obtained from localized measurements of the pile-up stress ahead of blocked slip bands and parametric curve fitting. Here it is important to note that the original basal micro-Hall-Petch multiplier was obtained by fitting the micro-Hall-Petch parameters for eight grain boundaries to a power-law type function of the maximum compatibility factor. The micro-Hall-Petch parameters for those eight grain boundaries were obtained by fitting pile-up stress measurements ahead of a blocked slip band, to expressions obtained from a continuum dislocation pile-up model. On the other hand, the crystal plasticity finite element simulations form a homogenized representation of the microstructure where a large number of points in the simulated microstructure accommodate slip as opposed to localized slip bands in experiments. Since all microstructural points in the synthetic microstructures are endowed with a micro-Hall-Petch coefficient and an underlying slip system-level grain size, this implies that a lower value of the basal micro-Hall-Petch multiplier is sufficient to capture the contribution of basal slip to the grain size effect. We additionally note that if not all microstructural points but only select number were endowed with the basal micro-Hall-Petch multiplier, the calibrated basal micro-Hall-Petch multiplier will increase and be closer to the original basal micro-Hall-Petch multiplier.

On the contrary, the calibrated prismatic micro-Hall-Petch multiplier is about 1.4

times that of the original prismatic micro-Hall-Petch multiplier obtained from localized measurements of the pile-up stress ahead of blocked slip bands and parametric curve fitting. Here again the original prismatic micro-Hall-Petch multiplier was obtained by fitting the micro-Hall-Petch parameters for seven grain boundaries to a power-law type function of the maximum compatibility factor. The micro-Hall-Petch parameters for those seven grain boundaries were obtained by fitting pile-up stress measurements ahead of a blocked slip band(initiated from a notch within a grain), to expressions obtained from a continuum dislocation pile-up model. In this case, the implication is that even with a homogenized model like crystal plasticity where each microstructural point has a contribution to the size effect, a relatively higher prismatic micro-Hall-Petch multiplier is necessary to capture the grain size effect. In other words, the effect of grain boundaries on prismatic slip is possibly more profuse when analyzing many different boundaries as compared to just the seven boundaries. We also note that the implementation of the micro-Hall-Petch constitutive model accounts for the maximum compatibility factor purely dependent on the orientation of neighboring grains without accounting for grain boundary inclination, which is not very straightforward to account for in a universal manner just because it is dependent on the underlying mesh used for computational studies. However, if a possible standardization can be achieved in the inclusion of grain boundary information across microstructure generation frameworks, then this information can be included without much additional effort providing better insights and possibly even better agreement between calibration parameters and experimentally-informed parameters.

5.4. Parametric Studies

We now carry out some simple parametric studies with the calibrated parameters to explore different examples where the grain size and texture are coupled.

5.4.1. Effect of simulated spread in texture

Here we simulate and study the behavior of the Hall-Petch slope for microstructures whose crystallographic textures are represented by predominantly basal texture superposed with a spread in orientations. This spread is representative of orientations spreading almost uniformly, away from the basal poles. All the microstructures used in this study were generated using DREAM.3D in which the respective textures were created by specifying the Euler angle(Bunge convention) triplet of $(0, 0, 0)$ with a weight equal to 100 and spread(denoted by ϵ) equal to a positive value denoting the respective spread in the orientations. For each texture, a base microstructure was first generated for the smallest grain size using the lognormal distribution parameters corresponding to the smallest grain size for Texture 2. This base microstructure was then uniformly scaled to twice, thrice and four times its size, to generate geometrically similar microstructures with different grain sizes. For a measure of the average 2D grain size, we used the grain area average size of the experimental 2D microstructure from which the 3D lognormal distribution parameters were obtained. Then for the smallest grain size case, the grain area average size is $68\mu m$, and accordingly, $136\mu m$, $204\mu m$ and $272\mu m$ for the microstructures scaled to twice, thrice and four times the smallest size, respectively. Additionally, to better represent the

underlying texture, microstructures with larger number of grains were created for the textures corresponding to $\epsilon = 20$, $\epsilon = 23$ and random texture. Figs. 5.8(a) - 5.8(i) depict the pole figures generated for different values of the spread considered, denoted by the ϵ value, alongwith the approximate number of grains contained in the synthetic microstructure for that texture. Simulations were performed in which the microstructures were deformed in tension along the z-direction to 1% strain, with periodic boundary constraints. Fig. 5.9(a) depicts the plots of the yield stress(σ_Y) against inverse square-root of grain size($1/\sqrt{d}$) for the different textures from which a linear least-squares fit (denoted by dotted line in the plots) yields the Hall-Petch intercept and the Hall-Petch slope (Fig. 5.9(c)). Here d denotes the measure of average 2D grain size noted earlier. Fig. 5.9(b) depicts the variation of the size-dependent component of the yield stress with inverse square-root of grain size for the different textures to better visualize the Hall-Petch slope. The Hall-Petch slope increases progressively from 49 MPa $\mu m^{1/2}$ for $\epsilon = 5$ to 79 MPa $\mu m^{1/2}$ for $\epsilon = 23$, close to the Hall-Petch slope for random texture at about 93 MPa $\mu m^{1/2}$. First a gradual increase is observed from 49 MPa $\mu m^{1/2}$ for $\epsilon = 5$ to 58 MPa $\mu m^{1/2}$ for $\epsilon = 15$, after which the increase is more drastic to 79 MPa $\mu m^{1/2}$ to $\epsilon = 23$. We now investigate a measure of the slip activity of different slip system families to reason this behavior. Fig. 5.10 visualizes the average accumulated slip on the basal, prismatic and twin systems at the end of deformation for the smallest grain size. The average accumulated slip for a particular slip system type(basal, prismatic or twin) is computed by averaging the total slip contribution of all slip systems associated with that slip system type, over the entire microstructure. For example, for the basal system the

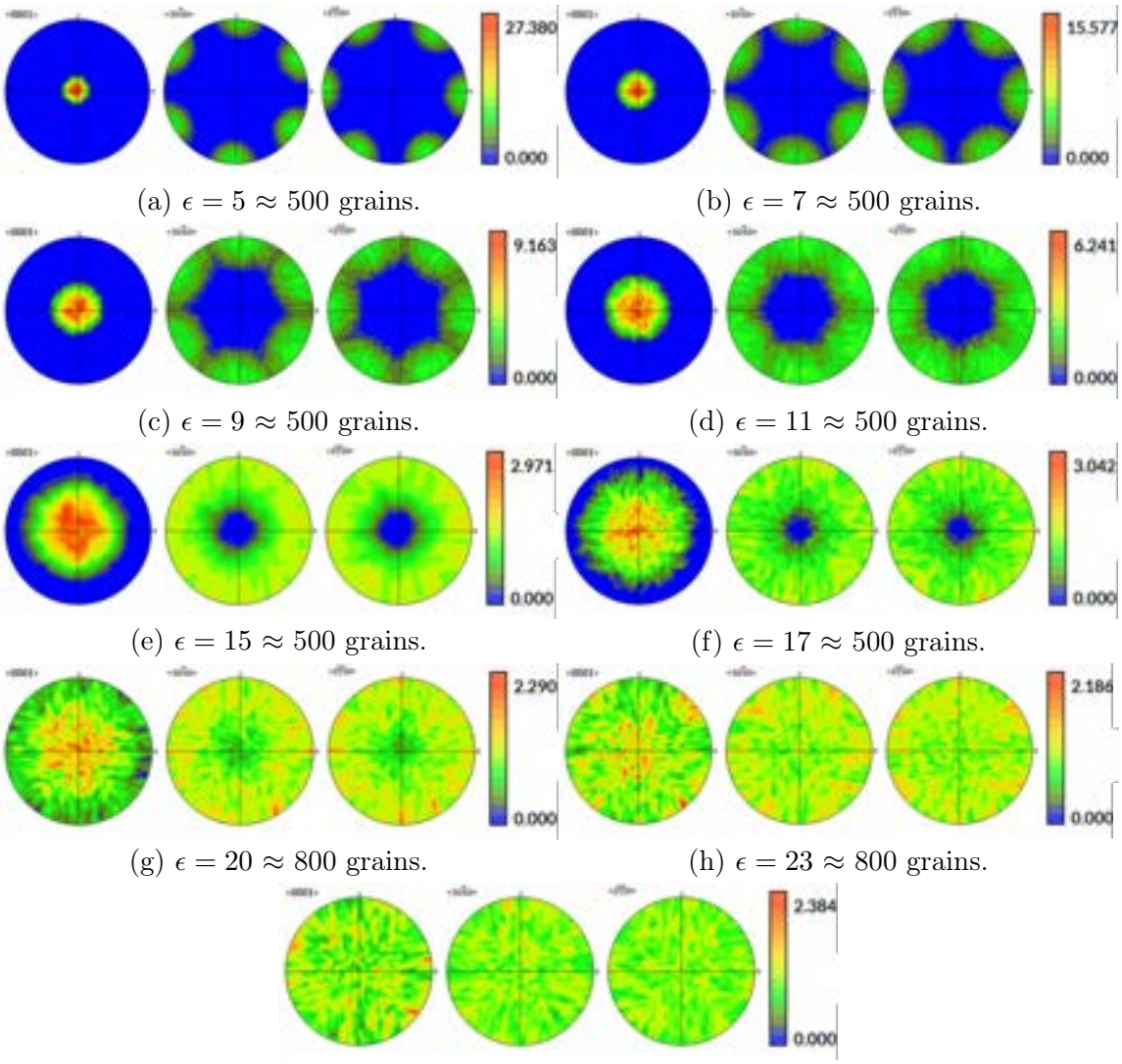

(a) $\epsilon = 5 \approx 500$ grains.

(b) $\epsilon = 7 \approx 500$ grains.

(c) $\epsilon = 9 \approx 500$ grains.

(d) $\epsilon = 11 \approx 500$ grains.

(e) $\epsilon = 15 \approx 500$ grains.

(f) $\epsilon = 17 \approx 500$ grains.

(g) $\epsilon = 20 \approx 800$ grains.

(h) $\epsilon = 23 \approx 800$ grains.

(i) Random texture ≈ 1300 grains.

Figure 5.8: Pole figures for increasing values of the ϵ value or spread in orientations and the approximate number of grains constituting the synthetic microstructure. Since, random texture corresponds to a uniform distribution of orientations, the pole figures were not generated in the same manner as the previous pole figures. Instead, a sample of random orientations was created using MTEX and specified as input to DREAM.3D.

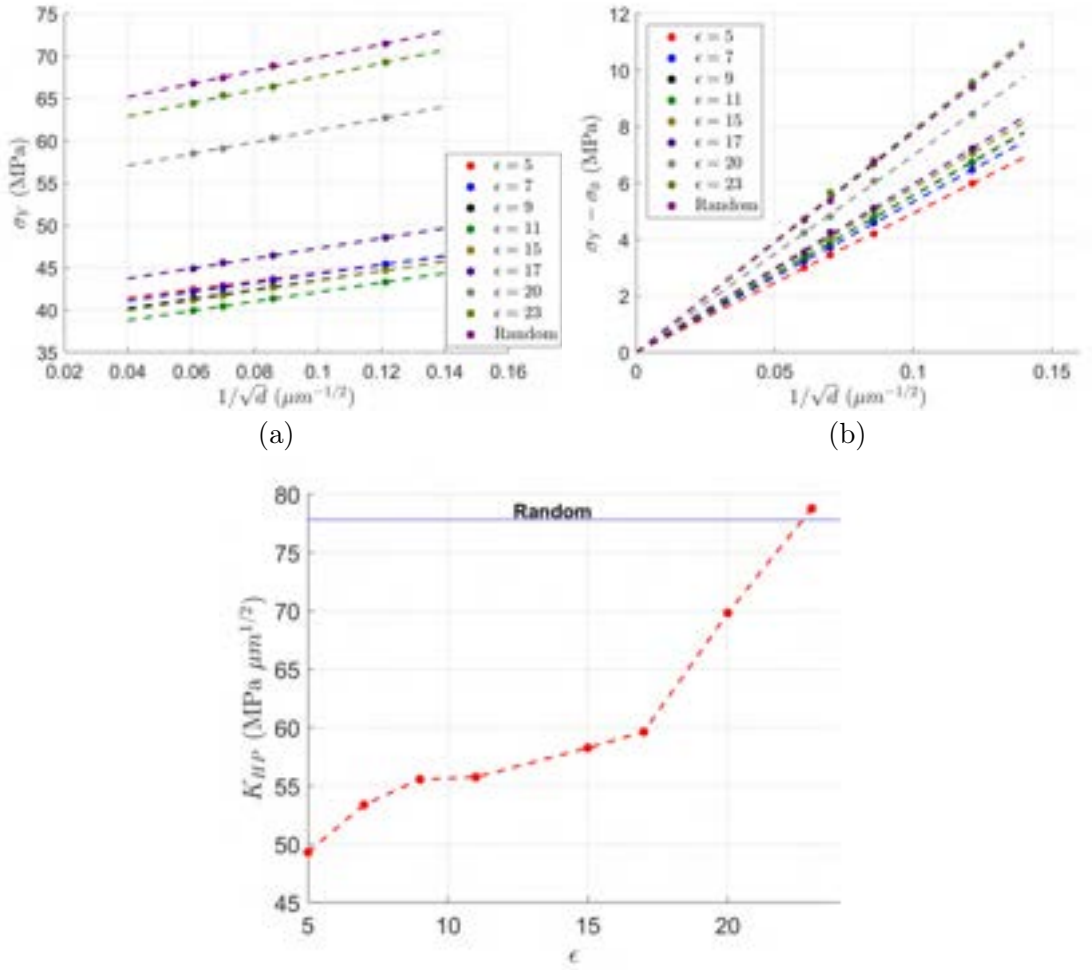

(a) (b)

(c)

Figure 5.9: (a) Yield stress(σ_Y) plotted against inverse square-root grain size($1/\sqrt{d}$) for different spreads of basal texture, and random texture. Dotted lines denote corresponding linear least-squares fit. (b) Size-dependent contribution of yield stress vs inverse square-root of grain size to visualize difference in Hall-Petch slopes. (c) Hall-Petch slope for different ϵ values.

total slip contribution from the three basal slip systems is computed for all points in the microstructure, and then the mean is taken over all those microstructural points. The Hall-Petch slope is a reflection of the activity of individual slip systems, since

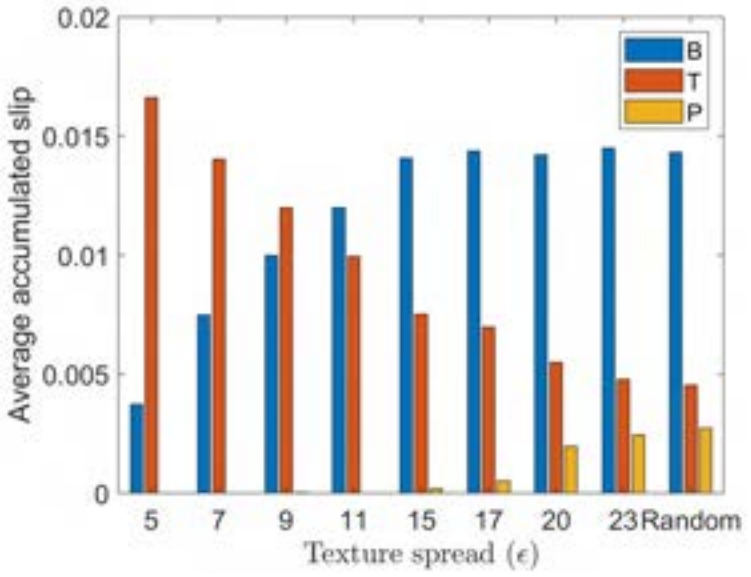

Figure 5.10: Comparison of average accumulated slip on basal, prismatic and twin systems at the end of deformation for different values of the spread ϵ. The average accumulated slip for a particular slip system type is computed by averaging the total slip contribution of all slip systems associated with that slip system type, over the entire microstructure. B–Basal, P–Prismatic, T–Twin.

even physically, slip has to ensue on individual slip systems for the effect of the grain boundaries(or alternatively the grain size) to be felt. As the spread increases from $\epsilon = 5$ to $\epsilon = 15$, there is an increase in the average basal accumulated slip and a decrease in the average twin accumulated slip. Note that for twinning there does not exist a maximum compatibility factor when accounting for the size-dependent contribution to the slip resistance, while for the basal systems the micro-Hall-Petch coefficient is multiplied with a power-law type function of the maximum compatibil-

ity factor. Additionally, for twinning there is a single average grain size used in the expression to modify the slip resistance, while for basal systems the slip system-level grain size, which is a heterogeneous property, comes into play. As a result, while the effect of twinning is almost homogeneous across all points where twinning accommodates slip, that is not the case for basal which shows a larger spread in it's contributions. Then there are two competing factors – (i) The decrease in twinning activity with increase in ϵ which reduces contribution of twinning to the Hall-Petch slope, while (ii) Increased basal activity combined with spread in texture increases basal contribution to the Hall-Petch slope due to delocalization of texture – more diffuse texture $\implies$ lower values of maximum compatibility factor $\implies$ increased contribution of basal slip to grain size effect. The increase in the Hall-Petch slope signifies the dominance of increased basal slip activity over twinning activity as we go from sharper texture for $\epsilon = 5$ to more diffuse texture for $\epsilon = 15$. Beyond $\epsilon = 15$ the Hall-Petch slope increases drastically and this is attributed to further delocalization of texture and the activation of prismatic systems, which have a relatively high micro-Hall-Petch coefficient compared to basal system. Even though prismatic slip systems don't show significant activity, combining the high micro-Hall-Petch coefficient of prismatic slip with smaller values maximum compatibility factor and increased prismatic slip activity ensures a steady increase in the Hall-Petch slope as the texture approaches random texture.

5.4.2. Effect of loading direction

In this section we study computationally the Hall-Petch slope of microstructures with sharp basal texture relative to the angle φ, made between the loading direction and direction of basal poles. This is in principle very similar to the experimental study presented by Wang et al. [37] which was performed for Mg-AZ31 alloy with more diffuse basal texture. Similar to that study, we consider five values of φ – 0°, 22.5°, 45°, 67.5° and 90°. For each φ, a microstructure was first generated for the smallest grain size using the lognormal distribution parameters corresponding to the smallest grain size for Texture 2. This microstructure was then uniformly scaled to twice, thrice and four times its size, hence generating the same microstructure with different grain sizes. Similar to the previous study, for the smallest grain size case, the grain area average size is taken to be 68 μm, and accordingly, 136 mum, 204 μm and 272 μm for the microstructures scaled to twice, thrice and four times the smallest size, respectively. Each microstructure was constructed as a 50 x 50 x 50 voxelated grid with approximately 500 grains. The synthetic microstructures were then deformed in tension along z-direction to a strain of 1% with periodic boundary constraints.

Fig. 5.11(a) a depicts the pole figures representing the orientation distribution based on which the synthetic microstructures were generated for this study. Fig. 5.11(b) depicts the plots of the yield stress(σ_Y) against inverse square-root of grain size($1/\sqrt{d}$) for different φ, from which a linear least-squares fit (denoted by dotted line) yields the Hall-Petch intercept and Hall-Petch slope (Fig. 5.11(d)). Here d denotes the measure of average 2D grain size noted earlier. Fig. 5.11(c) depicts the variation of

the size-dependent component of the yield stress with inverse square-root of grain size for the different φ. A very interesting behavior is observed here where the Hall-Petch slope first decreases to a minimum at $\varphi = 45°$ after which it increases again to $\varphi = 90°$. Fig. 5.12 visualizes the average accumulated slip on the basal, prismatic and twin systems at the end of deformation for the smallest grain size. As φ varies from 0° to 45° , the activity of basal slip increases while the twinning activity decreases. Unlike the previous parametric study, the texture is the same for different relative angles of loading and the decrease in effect of twinning activity dominates over the increased basal activity, resulting in a decrease in the Hall-Petch slope from 47 MPa $\mu m^{1/2}$ when twinning predominates at 0° to 15 MPa $\mu m^{1/2}$ when basal predominates at 45°. Subsequently, as φ increases from 45° to 90° prismatic activity increases significantly while basal activity decreases and twinning activity remains negligible. Due to the relatively high micro-Hall-Petch coefficient of prismatic system compared to basal system, the increase in prismatic activity dominates the decrease in basal activity, contributing to the net increase in the Hall-Petch slope from 45° to 90°.

5.4.3. Yield stress variation with grain morphology

In this section, we study the variation of yield stress of simulated microstructures with different grain morphologies with underlying crystallographic texture corresponding to the Texture 1 from experiments. First, a microstructure was generated for the smallest grain size using the lognormal distribution parameters corresponding to the smallest grain size. The synthetic microstructure used for this study is a 50 x 50 x

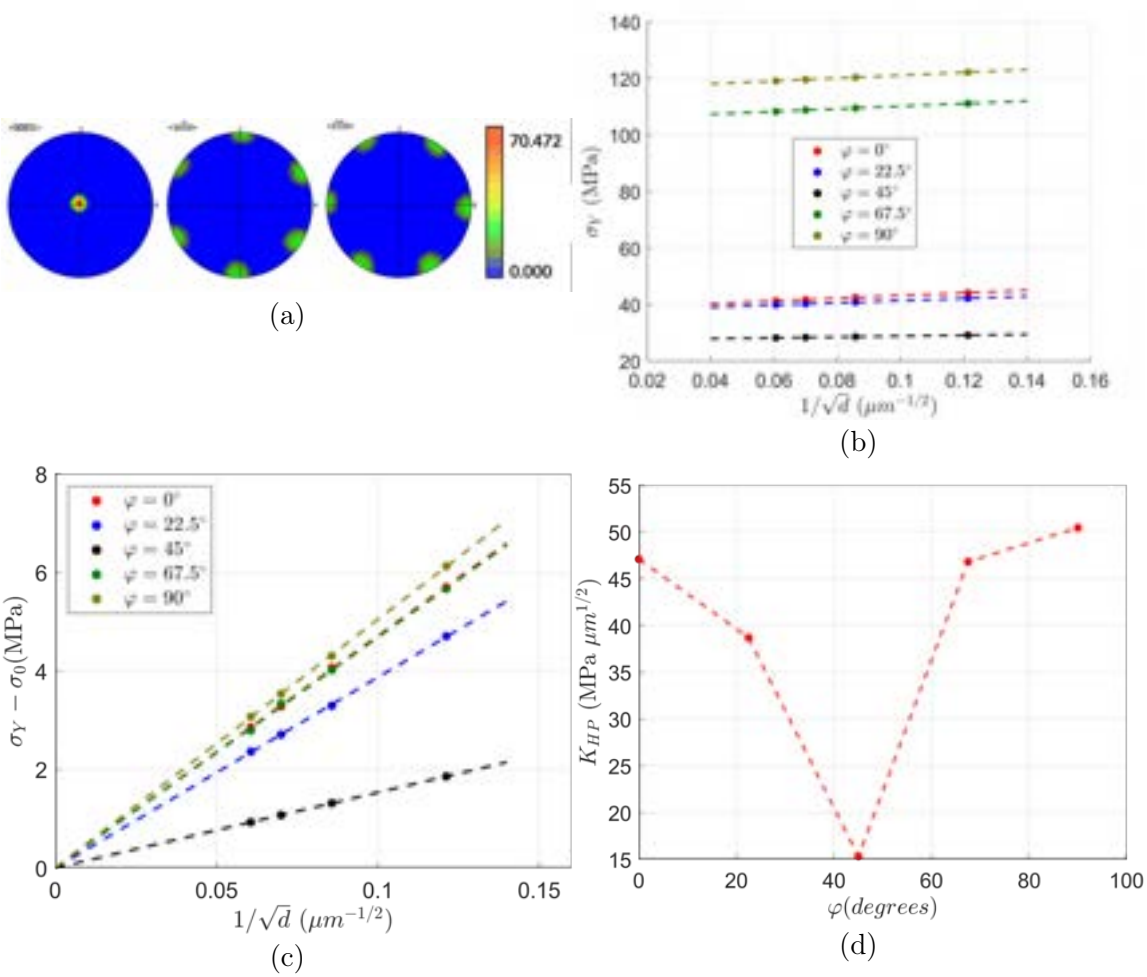

Figure 5.11: (a) Pole figures of strong basal texture used to generate the microstructures for this study. (b) Yield stress(σ_Y) plotted against inverse square-root grain size($1/\sqrt{d}$) for different relative loading directions given by φ. Dotted lines denote corresponding linear-fit. (c) Size-dependent contribution of yield stress. (d) Hall-Petch slope plotted for different φ values.

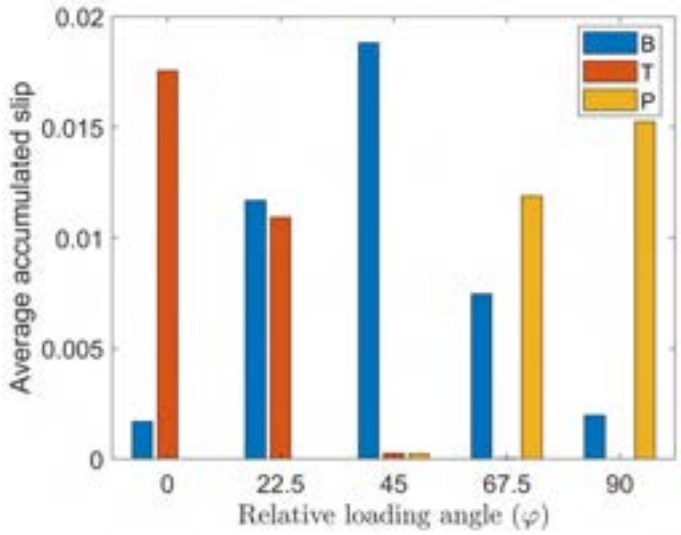

Figure 5.12: Comparison of average accumulated slip at the end of deformation for basal, prismatic and twin systems for different angles φ. B–Basal, P-Prismatic, T-Twin.

50 voxelated grid consisting of approximately 500 grains. Different morphologies are quantified by the aspect ratio α, which is used to modify the voxel spacings depending on the relative aspect ratios along three orthogonal directions. Let us consider a microstructure containing equiaxed grains with voxel resolutions of Δl along the x, y and z-direction, for which we wish to construct a microstructure with grains possessing an aspect ratio of α. Then the triplet of resolutions for the equiaxed microstructure, $(\Delta l, \Delta l, \Delta l)$ is transformed to the new triplet $(\alpha^{-1/3}\Delta l, \alpha^{-1/3}\Delta l, \alpha^{2/3}\Delta l)$. This preserves the volume of the each voxel and hence the entire grain, as a result preserving the grain size statistics as well. Additionally, the aspect ratio now corresponds to the ratio of the transformed resolution along the z-direction to that along the x(or y)-direction. This eventually affects the computation of slip system-level grain size

and subsequently the contribution to the slip resistance. Earlier work on incorporating the grain size effect has focused on modifying the slip resistance based on the average grain size alone, which in this case is the same for all microstructures since the grain volumes are preserved. As a result, the morphology of the grains cannot be captured in those models, unlike the present one where the morphology affects the slip system-level grain sizes.

CPFE simulations are performed on the microstructures which are deformed in tension along the z-direction to 1% engineering strain with periodic boundary constraints. Nine different aspect ratios(α) are considered: 1/5, 1/4, 1/3, 1/2, 1, 2, 3, 4, 5. Fig. 5.13 depicts the variation of the yield stress with change in aspect ratio. It is interesting to note that the yield stress is asymmetric relative to the

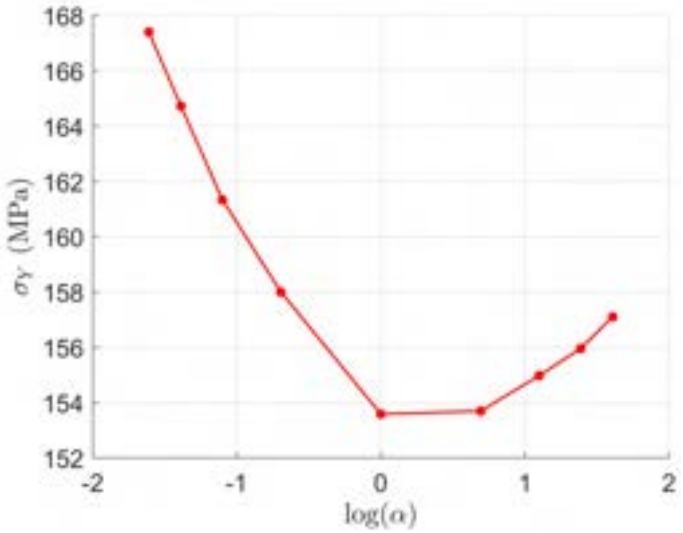

Figure 5.13: Yield stress (σ_Y) for different aspect ratios of grains. Note the asymmetry in the yield stress relative to the logarithm of the aspect ratio α.

logarithm of the aspect ratio. This is in contrast to a symmetric trend obtained by

Sun et al. [158] in their statistical approach using a grain size orientation distribution function to couple crystallographic texture and grain size in the study of grain size-effect in two-dimensional microstructures exhibiting two slip systems. To explain this asymmetry, we obtain the relevant expressions using elementary geometry and some crystallographic and plastic properties particular to as-extruded texture.

We first note that the microstructures for different aspect ratios used in this study are generated by uniform stretches along the three orthogonal directions of a microstructure with equiaxed grains. Since equiaxed grains are essentially space filling representations of spheres, the grains in microstructures with aspect ratios different from 1 are prolate or oblate spheroids depending on $\alpha > 1$ or $\alpha < 1$, respectively, with the axis of circular symmetry coinciding with the z-direction. Now consider such an ellipsoid with axes lengths abiding the ratio dictated by the triplet of resolutions used to generate the microstructure. Denote the semi-axes lengths along the x, y and z directions by a, b and c respectively, and let R denote the radius of the sphere representing the equivalent sphere grain diameter of the equiaxed grain from which the ellipsoidal grain was obtained. Then the semi-axes lengths must be $a = \alpha^{-1/3}R$, $b = \alpha^{-1/3}R$ and $c = \alpha^{2/3}R$ resulting in the following equation for the ellipsoid :

$$\begin{aligned} & \frac{x^2}{a^2} + \frac{y^2}{b^2} + \frac{z^2}{c^2} = 1 \\ \implies & \frac{x^2}{\alpha^{-2/3}} + \frac{y^2}{\alpha^{-2/3}} + \frac{z^2}{\alpha^{4/3}} = R^2 \\ \coloneqq & \frac{r^2}{\alpha^{-2/3}} + \frac{z^2}{\alpha^{4/3}} = R^2 \end{aligned} \tag{5.4}$$

In the context of the as-extruded texture, the $(10\bar{1}0)$ poles are concentrated in the ex-

trusion direction, as seen in the $(10\bar{1}0)$ pole figure. In addition to this, the basal plane normals are aligned perpendicular to the extrusion direction, with almost uniform distribution as evidenced by the close to vertical band in the (0001) pole figure. This suggests a theoretically uniform arrangement of the HCP unit cells about the extrusion direction with the $(10\bar{1}0)$ prismatic plane normal being parallel to the extrusion direction (Fig. 5.14). From the perspective of plasticity, the basal and prismatic systems are the primary slip systems activated when this texture is deformed along the extrusion direction. Fig. 5.15 depicts a plot of the percentage contribution to average accumulated slip at the end of deformation by the three individual basal and prismatic slip systems. Even though there is some difference in the average accu-

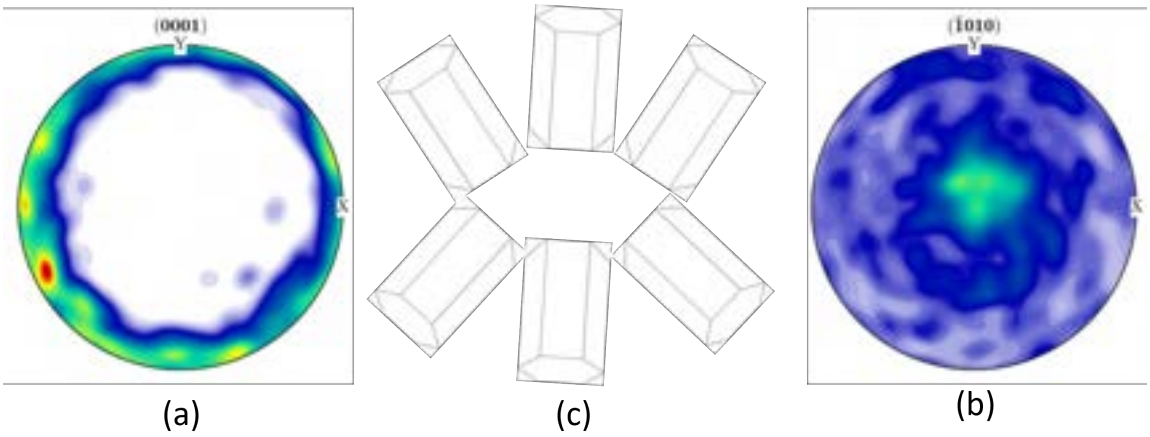

Figure 5.14: (a) (0001) pole figure, (b) $(10\bar{1}0)$ pole figure, and (c) theoretical arrangement of HCP unit cells symmetrically about the extrusion direction with the $(10\bar{1}0)$ plane normal pointing along the extrusion direction.

mulated slip by slip systems corresponding to different slip direction, let's assume for theoretical purposes that they are equal. In other words, slip systems corresponding to each slip direction contribute equally to the total average accumulated slip due to

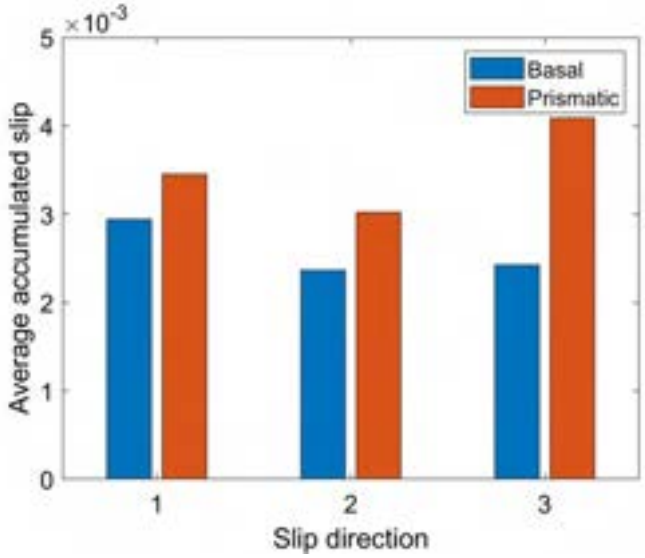

Figure 5.15: The average accumulated slip on the three basal and three prismatic slip systems. The integers on the x-direction denote a specific slip direction : '1' - $[11\bar{2}0]$, '2' - $[\bar{2}110]$ and '3' - $[1\bar{2}10]$.

basal and prismatic systems. This means that among the three slip directions one of them is always perpendicular to the extrusion direction while the remaining two are at 30° to the extrusion direction. In our case, slip direction '1' is perpendicular to the extrusion direction, while the remaining two directions are at 30° to the extrusion direction. Let's now consider the measure of grain size for a particular slip direction as the length of the line segment passing through the center of the ellipsoid with direction coinciding with the slip direction. Denote this grain size measure for slip direction 'i' by d_i. With knowledge of the slip directions relative to the ellipsoid the grain size measures are straightforward to obtain using Eqn. 5.4 :

$$d_1 = \alpha^{-1/3} R \; ; \; d_2 = d_3 = \frac{2R}{\sqrt{3}} \left(\frac{\alpha^{2/3}}{3} + \alpha^{-4/3} \right)^{-1/2} \tag{5.5}$$

With the earlier assumption of equal contribution of slip from the slip directions, the size-dependent contribution to the yield stress can be expressed as being proportional to the quantity β defined using Eqn. 5.5 with the inverse square-root dependence on grain size measure:

$$\begin{aligned}\beta :=& \sum_{i=1}^{3} \frac{1}{\sqrt{d_i}} = \frac{1}{\sqrt{\alpha^{-1/3}R}} + \frac{\sqrt{2}\left(\alpha^{2/3} + 3\alpha^{-4/3}\right)^{1/4}}{\sqrt{R}} \\ =& \frac{1}{\sqrt{R}}\left(\sqrt{\alpha^{1/3}} + \sqrt{2}\left(\alpha^{2/3} + 3\alpha^{-4/3}\right)^{1/4}\right) \\ =& \frac{\delta(\alpha)}{\sqrt{R}}\end{aligned} \tag{5.6}$$

Where $\delta(\alpha)$ encodes the dependence of the yield stress on the aspect ratio α. This function is visualized by plotting it(Fig. 5.16). We retrieve a curve very similar to the variation captured in Fig. 5.13, demonstrating that the trends in the role of aspect ratio on the yield stress based on the micro-Hall-Petch equation can be captured to a reasonable extent using simple theoretical arguments.

5.5. Conclusions

In this chapter we detailed one possible implementation of the micro-Hall-Petch constitutive model into the PRISMS-CPFE framework. Subsequently, the crystal plasticity constitutive parameters and micro-Hall-Petch coefficients were calibrated against macroscopic stress-strain curves from nine different texture-grain size-loading combinations. After comparison of the calibrated parameters with the original parameters obtained from Chapter III and Chapter IV, the calibrated parameters were

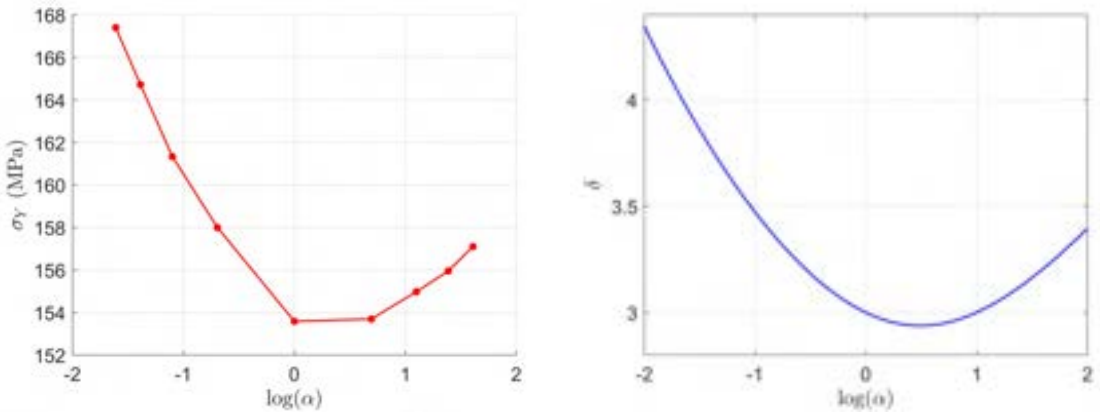

(a) (b)

Figure 5.16: (a) Variation of yield stress with aspect ratio (b) $\delta(\alpha)$ plotted against $\log(\alpha)$ based on the numerator in Eqn. 5.6.

used to perform parametric studies to study the Hall-Petch slope variation relative to changes in spread around basal texture and loading direction relative to basal poles. This was also followed by examining predictions of the yield stress for different aspect ratios of grains, where the asymmetry in the trend was explained based on a simple derivation.

CHAPTER VI

Conclusions and Future Work

6.1. Summary

The primary goal of this thesis was to propose and develop a general methodology to couple the grain size-effect with the underlying microstructural aspects, with specific application to Mg-4Al alloy system.

First, the rate-dependent crystal plasticity formulation, implementation into PRISMS-CPFE and some numerical examples were presented, which formed the basic constitutive model for all crystal plasticity simulations in the rest of the thesis. We then delved into the integration of dislocation pile-up theory, crystal plasticity simulations with HR-EBSD measurements to estimate the micro-Hall-Petch parameters corresponding to basal slip for different GBs. The micro-Hall-Petch parameters for basal slip were obtained by fitting HR-EBSD pile-up stress measurements ahead of a slip band blocked by a GB, to an analytical expression obtained from a CDD model combined with the micro-Hall-Petch assumptions. The relevant grain boundary required to parametrize the micro-Hall-Petch parameters required relevant slip

system information in the grains sharing the GB. Crystal plasticity simulations of the microstructural sections representing the neighborhoods of the GBs of interest were used to furnish this information. Subsequently, the micro-Hall-Petch parameters were parametrized relative to the LRB factor and LM factor via an empirical power-law expression, and the resulting fit yielded the micro-Hall-Petch multiplier and micro-Hall-Petch exponent for the basal system, which are the key material constants associated with the grain size-effect on basal slip.

A similar metholodology was adopted to estimate and parametrize the micro-Hall-Petch parameters for prismatic slip with some key differences - (i) identification of grains with notches to initiate a prismatic slip band due to the relatively high slip resistance compared to basal slip, (ii) a modified dislocation pile-up model accounting for the notch, and (iii) crystal plasticity simulations of microstructural sections representing neighborhoods of the GB, also accounting for the notch. Subsequently, the micro-Hall-Petch parameters were parametrized relative to two GB metrics motivated from slip transmission studies - the Lee-Robertson-Birnbaum (LRB) factor and Luster-Morris (LM) factor - which are geometric quantities that encode information about active slip systems in neighboring grains and the inclination of the GB plane. In particular, the LRB factor is computed from the trace of slip planes associated with relevant slip systems in neighboring grains on the GB, and the slip directions. The LM factor, on the other hand, is only computed from the slip plane and slip direction information associated with the relevant slip systems in neighboring grains, without any dependence on the GB inclination. This parametrization was performed via an empirical power-law expression, and the resulting fit yielded the micro-Hall-

Petch multiplier and micro-Hall-Petch exponent for the prismatic system, which are the key material properties associated with the grain size-effect on prismatic slip. Finally, the problem of incorporating the micro-Hall-Petch model into PRISMS-CPFE was addressed providing a specific procedure to accomplish this. The model was then calibrated with macroscopic stress-strain curves on Mg-4Al samples including nine texture-grain size-loading combinations. The calibrated parameters were then compared to the parameters estimated from localized experimental studies and the discrepancies were briefly addressed. We then concluded this with some parametric studies to investigate the model behavior with respect to different scenarios - texture modification, loading direction and aspect ratio of grains.

The key contributions of this thesis include the development of a framework integrating CP simulations, continuum dislocation pile-up theory, HR-EBSD pile-up stress measurements and empirical rules to obtain key material parameters that characterize the effect of the grain size on the slip system resistance of basal and prismatic slip systems. Further, we demonstrated a methodology to incorporate framework into CP constitutive models, performing calibration against experimental stress-strain data and performing some parametric studies to assess the model behavior. Such an approach can be quite useful in encoding the effect of grain size, or in general, a microstructural length scale in polycrystalline plasticity models so as to capture the coupling between grain size and texture for arbitrary alloy systems.

6.2. Future Work

The proposed methodology can be supplemented and extended in multiple ways :

1. Presently, the maximum compatibility factor used in the model is solely dependent on the orientation of neighboring grains and the slip systems under consideration through the LM factor. This approach can further be refined, with some caution, to include the grain boundary inclinations via the LRB factor. However, this must also be supplemented with usage of microstructure meshes which can furnish this information of the grain boundary inclinations and that this information is independent of the meshing itself. This is particularly important since two identical microstructures can be meshed to provide very different distribution of grain boundary inclinations, which can make the results irreproducible or too specialized. One possible way to achieve this is by using algorithms to smoothen the grain boundaries [159, 160] represented in the underlying microstructure mesh. More importantly, apart from texture and grain size distributions, some information associated with the grain boundary inclinations must also be included in synthetic microstructure generation algorithms. Rohrer et al. [161, 162] presented a review of techniques that can be used to study the mesoscopic crystallographic structure of grain boundary networks and to determine the grain boundary character distribution(GBCD), which is the essential information to construct LRB factors for the microstructure. Lieberman et al. [163] proposed new technique utilizing first order Cartesian moments of binary indicator functions, to determine grain boundary normals directly from a voxelized microstructure image. These aspects can be integrated to use the input GBCD to construct a synthetic microstructure from which the grain boundary normals can be computed from

the computational technique.

2. The micro-Hall-Petch coefficients obtained from our previous work involving localized experiments associated with slip bands blocked by grain boundaries, are not in agreement with the parameters obtain post-calibration with stress-strain curves. This is not unexpected since the basis of these two approaches is quite different – pile-up stress measurements are localized while crystal plasticity constitutive modeling is homogenized. One possible line of study could be trying to relate the two sets of coefficients through some multiscale modeling approach, in which the micro-Hall-Petch coefficients obtained from calibration can be derived(to some degree of approximation) through coarse-graining the micro-Hall-Petch coefficients obtained from pile-up stress studies. Without any reference to the micro-Hall-Petch model, some efforts in determining the Hall-Petch slope from the slip system-level Hall-Petch slope has been addressed in earlier work [37, 27, 5]. Such an approach can be adopted but with the micro-Hall-Petch model being the locally operating model to coarse-grain.

3. While the micro-Hall-Petch modification was incorporated for basal and prismatic slip systems, extending the approach to twinning is a natural next step. To accomplish this will involve developing a model to obtain expressions of the pile-up stress ahead of a twin blocked by a grain boundary. There has been previous work in the description of twins using dislocation models [164, 165, 166] and associated applications of these models [167, 168, 169]. This work can be integrated with experimental pile-up stress measurements ahead of a twin blocked by a grain boundary and then relate the micro-Hall-Petch parameters

to appropriate measures of compatibility [170, 171, 172].

4. One of the shortcomings of the micro-Hall-Petch constitutive model is that it addresses the effect of grain size through the microstructural aspects only on the initial slip resistance and not during the hardening stages. On the contrary, the well-researched field of strain-gradient plasticity [97, 98, 99, 100], which is based on the idea of GNDs targets exactly this issue, but without any modifications to the initial slip resistance. In this approach, the loss of compatibility of the lattice is captured using the plastic part of the deformation gradient($\boldsymbol{F^p}$) [173],

$$\boldsymbol{G} = \boldsymbol{F^p}\,(\nabla \times \boldsymbol{F^p}) \tag{6.1}$$

where $\boldsymbol{G}$ is the kinematic incompatibility tensor which is a measure of the incompatibility associated with the intermediate configuration. Attributing this incompatibility to the presence of dislocations which are required to be present in order to accommodate this geometric incompatibility we have

$$\mathbf{G^T} = \sum_{\alpha=1}^{N_G} \rho_G^\alpha \mathbf{b}^\alpha \otimes \mathbf{t}^\alpha \tag{6.2}$$

where N_G is the total number of GND systems, ρ_G^α denotes the GND density on GND system α, with Burgers vector $\mathbf{b}^\alpha$ and unit line direction $\mathbf{t}^\alpha$. The task to compute $\boldsymbol{\rho}_G = [\rho_G^\alpha]$ (GND density vector) when $\mathbf{G^T}$ is known, reduces to solving an under-determined system. Arsenlis et al. [174] proposed a way to address this issue by defining convex objective functions in terms of the GND

densities, whose minimizer, subject to Eqn. 6.2, is unique. Two objective functions were proposed - (i) L-2 norm of the GND density vector and (ii) L-1 norm of the GND density vector. While the quadratic objective function is reminiscent of the stored energy due to the GNDs the linear objective function relates to the total GND line length. In the present scenario, for the sake of simplicity we choose to minimize the L-2 norm objective function, which furnishes a closed-form expression for the GND density vector.

Denote $\boldsymbol{\rho}_G$ by the vector of GND densities. The objective function augmenting the constraint Eqn. 6.2 takes the form

$$\phi\left(\boldsymbol{\rho}_G, \boldsymbol{c}\right) = \boldsymbol{\rho}_G \cdot \boldsymbol{\rho}_G + \boldsymbol{c} \cdot \left(\boldsymbol{A}\boldsymbol{\rho}_G - \boldsymbol{b}\right) \tag{6.3}$$

where $\mathbf{b}$ and $\mathbf{A}$ are vector and matrix rearrangements of the LHS and RHS, respectively, of Eqn. 6.2. Further, we note that $\mathbf{A}$ is a $9 \times n$ while $\mathbf{b}$ is a 9×1 vector. The vector of GND densities takes the form

$$\boldsymbol{\rho}_G = \mathbf{A}^{\mathbf{T}}\left(\boldsymbol{A}\boldsymbol{A}^{\boldsymbol{T}}\right)^{-1}\mathbf{b} = \mathcal{A}\mathbf{b} \tag{6.4}$$

Fig. 6.1 depicts the $L2$-norm of the GND density vector(obtained through post-processing alone) for an FCC polycrystal deformed upto 3% tensile strain, where higher numerical values of the GND density are computd at the GBs. This can be particularly important in developing criteria based on the stored defect energy computed from the GND density to nucleate either second phases, twins or recrystallization nuclei at the GBs. The GND density can also be used

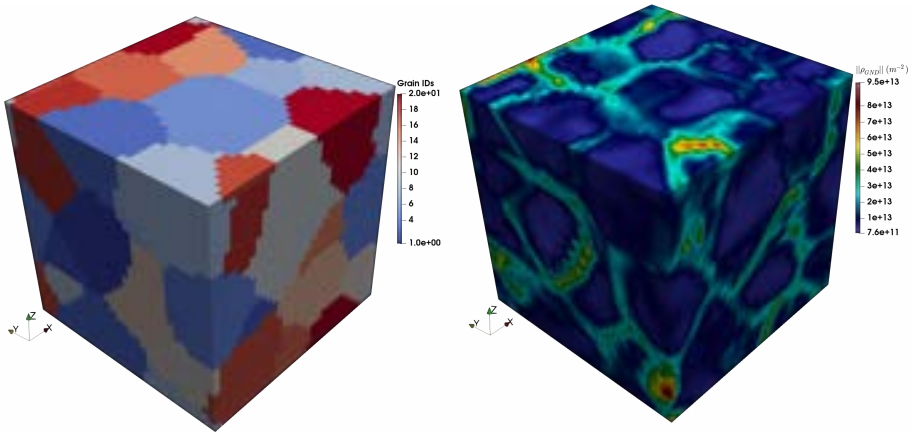

Figure 6.1: Map of $L2$-norm of GND density vector for FCC polycrystal subject to 3% tensile strain.

in informing both isotropic and kinematic hardening laws [175, 176, 177] which in turn can capture the effect of the microstructural length scale on hardening,

$$\tau_c^\alpha = \tau_0^\alpha + \mu^\alpha b^\alpha \sqrt{\sum_{\beta=1}^{N_g} L^{\alpha\beta} \rho_G^\beta} \tag{6.5}$$

Then the micro-Hall-Petch constitutive model can be integrated with a strain-gradient crystal plasticity model, wherein the initial slip resistances are modified based on the micro-Hall-Petch model and subsequent hardening is encoded within the strain-gradient plasticity framework. This, of course, comes at the cost of a large number of experiments that will need to be performed in order to calibrate the strain-gradient plasticity model due to the large number of parameters arising via the hardening matrix.

5. While the calibration of the constitutive model was performed with respective to macroscopic stress-strain curves, the calibrated parameters can be used to

examine predictions on local strain field distribution which can be extracted using 2D SEM-DIC experiments [131, 178, 179] or in 3D via High energy diffraction microscopy (HEDM) [180]. When using SEM-DIC, it is noted that the micro-Hall-Petch constitutive model requires 3D data of the microstructure which is not necessarily straightforward to obtain, specific algorithms can be used which preserve the same SEM-DIC section while generating different microstructure instances depending on different choices of the subsurface grains. Ganesan et al. [181] have developed a generalized inverse Voronoi approach for reconstruction of 3D microstructures from 2D images. They demonstrated the non-trivial effect of the subsurface grains in the third dimension, on the continuum fields for a given microstructural section. When using 3D HEDM, far field measurements can be used to obtain the strain distribution in the microstructure but this is accompanied by the loss of grain boundary features because only the center of masses of grains are obtained in this modality. Additional methods such as Markov random field sampling [182, 183, 184] can be used to develop realistic reconstructions of the microstructural samples for use in micro-Hall Petch CP codes.

6. It is well known that grain size plays an important role in fatigue life of alloys [185], primarily determined by the role grain boundaries play in accumulation of elastic stored energy in grains in the role of an impediment to dislocation transmission across grains [186]. Micro-Hall Petch models can be used to study this effect as a function of crystallographic texture, grain size, and grain morphologies to demonstrate the effects of these attributes on extreme value

fatigue response. Recently, the effects of crystallographic texture and grain morphology on the extreme value fatigue response of 7075 Aluminum alloy was computationally demonstrated using an ellipsoidal model of grains [187]. The results show that the grain morphology effect is critical for the microstructures that deviate from equiaxed grains. For example, addition of grain size and morphology effects in crystal plasticity simulations increase the maximum plastic shear strain range most notably for grains strained in the direction of grain elongation. The work also indicates that equiaxed grains represent the "worst case" scenario for the driving forces for fatigue crack formation. The effect of grain morphology predicted by theory can benefit from validation against experimental measurements using HEDM as well as the use of micro-Hall Petch based crystal plasticity models as a microstructure design tool to increase fatigue life can be explored [188, 189, 190].

The procedure described in this thesis is by no means restricted to a specific material system and can be extended to any crystalline material system where plasticity is dominated by dislocation flow which manifest in the form of localized slip bands, and where the grain size effect is linked to the ability of grain boundaries to blocking these slip bands.

APPENDICES

APPENDIX A

Stress Power

Following [191], the stress power per unit volume of the isoclinic intermediate configuration is given as,

$$\dot{\omega} = \det(\boldsymbol{F})\,\boldsymbol{\sigma} : \boldsymbol{L} \tag{A.1}$$

where $\boldsymbol{F}$ is the deformation gradient, $\boldsymbol{\sigma}$ is the Cauchy stress and $\boldsymbol{L}$ is the velocity gradient. Expanding $\boldsymbol{L}$ we obtain

$$\begin{aligned} \boldsymbol{L} &\coloneqq \dot{\boldsymbol{F}}\boldsymbol{F}^{-1} = \dot{\overline{\boldsymbol{F}^{e}\boldsymbol{F}^{p}}}\boldsymbol{F}^{e}\boldsymbol{F}^{p-1} \\ &= \dot{\boldsymbol{F}}^{e}\boldsymbol{F}^{e-1} + \boldsymbol{F}^{e}\dot{\boldsymbol{F}}^{p}\boldsymbol{F}^{p-1}\boldsymbol{F}^{e-1} \end{aligned} \tag{A.2}$$

which upon substituting into Eqn. A.1 yields

$$\dot{\omega} = \dot{\omega}^{e} + \dot{\omega}^{p}$$

$$= \left(\det(\boldsymbol{F})\,\boldsymbol{\sigma}\colon\ \left(\dot{\boldsymbol{F}}^{\boldsymbol{e}}\boldsymbol{F}^{\boldsymbol{e}-1}\right)\right) + \left(\det(\boldsymbol{F})\,\boldsymbol{\sigma}\colon\ \left(\boldsymbol{F}^{\boldsymbol{e}}\dot{\boldsymbol{F}}^{\boldsymbol{p}}\boldsymbol{F}^{\boldsymbol{p}-1}\boldsymbol{F}^{\boldsymbol{e}-1}\right)\right)$$

with $\dot{\omega^e}$ and $\dot{\omega^p}$ denoting the elastic and plastic contributions, respectively, to the total stress power.

The elastic stress power, $\dot{\omega^e}$ can be rearranged as follows

$$\begin{aligned}
\dot{\omega^e} &= \det(\boldsymbol{F})\sigma\colon\ \left(\dot{\boldsymbol{F}}^{\boldsymbol{e}}\boldsymbol{F}^{\boldsymbol{e}-1}\right) \\
&= \mathrm{tr}\left(\det(\boldsymbol{F})\sigma\boldsymbol{F}^{\boldsymbol{e}-T}\dot{\boldsymbol{F}}^{\boldsymbol{e}T}\right) \\
&= \mathrm{tr}\left(\boldsymbol{F}^{\boldsymbol{e}}\boldsymbol{F}^{\boldsymbol{e}-1}\det(\boldsymbol{F}^{\boldsymbol{e}})\sigma\boldsymbol{F}^{\boldsymbol{e}-T}\dot{\boldsymbol{F}}^{\boldsymbol{e}T}\right) \\
&= \mathrm{tr}\left(\boldsymbol{F}^{\boldsymbol{e}}\det(\boldsymbol{F}^{\boldsymbol{e}})\boldsymbol{F}^{\boldsymbol{e}-1}\sigma\boldsymbol{F}^{\boldsymbol{e}-T}\dot{\boldsymbol{F}}^{\boldsymbol{e}T}\right) \\
&= \mathrm{tr}\left(\boldsymbol{F}^{\boldsymbol{e}}\boldsymbol{T}\dot{\boldsymbol{F}}^{\boldsymbol{e}T}\right) \\
&= \mathrm{tr}\left(\boldsymbol{T}\dot{\boldsymbol{F}}^{\boldsymbol{e}T}\boldsymbol{F}^{\boldsymbol{e}}\right) \\
&= \mathrm{tr}\left(\boldsymbol{T}\dot{\boldsymbol{E}}^{\boldsymbol{e}}\right) \\
&= \boldsymbol{T}\colon\dot{\boldsymbol{E}}^{\boldsymbol{e}}
\end{aligned} \tag{A.3}$$

yielding power conjugate stress and strain measures which are related through a linear relationship using the generalized Hooke's law. Following a similar procedure for the plastic stress power results in,

$$\begin{aligned}
\dot{\omega^p} &= \det(\boldsymbol{F})\,\boldsymbol{\sigma}\colon\ \left(\boldsymbol{F}^{\boldsymbol{e}}\dot{\boldsymbol{F}}^{\boldsymbol{p}}\boldsymbol{F}^{\boldsymbol{p}-1}\boldsymbol{F}^{\boldsymbol{e}-1}\right) \\
&= \mathrm{tr}\left(\det(\boldsymbol{F})\,\boldsymbol{\sigma}\boldsymbol{F}^{\boldsymbol{e}-T}\boldsymbol{F}^{\boldsymbol{p}-T}\dot{\boldsymbol{F}}^{\boldsymbol{p}T}\boldsymbol{F}^{\boldsymbol{e}T}\right) \\
&= \mathrm{tr}\left(\boldsymbol{F}^{\boldsymbol{e}}\det(\boldsymbol{F})\,\boldsymbol{F}^{\boldsymbol{e}-1}\boldsymbol{\sigma}\boldsymbol{F}^{\boldsymbol{e}-T}\boldsymbol{F}^{\boldsymbol{p}-T}\dot{\boldsymbol{F}}^{\boldsymbol{p}T}\boldsymbol{F}^{\boldsymbol{e}T}\right)
\end{aligned}$$

$$
\begin{aligned}
&= \mathrm{tr}\left(\boldsymbol{F^e T F^{p-T}} \dot{\boldsymbol{F}}\boldsymbol{^{p^T}} \boldsymbol{F^{eT}}\right) \\
&= \mathrm{tr}\left(\boldsymbol{F^e T F^{p-T}} \dot{\boldsymbol{F}}\boldsymbol{^{p^T}} \boldsymbol{F^{eT}}\right) \\
&= \mathrm{tr}\left(\boldsymbol{F^{eT} F^e T F^{p-T}} \dot{\boldsymbol{F}}\boldsymbol{^{p^T}}\right) \\
&= \left(\boldsymbol{F^{eT} F^e T}\right) : \left(\dot{\boldsymbol{F}}\boldsymbol{^p F^{p-1}}\right) \\
&= \left(\boldsymbol{F^{eT} F^e T}\right) : \boldsymbol{L^p} \qquad \text{(A.4)}
\end{aligned}
$$

Expanding $\boldsymbol{L^p}$ in terms of the slip rates in individual slip systems yields

$$
\begin{aligned}
\dot{\omega}^p &= \left(\boldsymbol{F^{eT} F^e T}\right) : \left(\sum_{\alpha=1}^{n_s} \dot{\gamma}^\alpha \boldsymbol{S_0^\alpha}\right) \\
&= \sum_{\alpha=1}^{n_s} \dot{\gamma}^\alpha \left(\boldsymbol{F^{eT} F^e T}\right) : \boldsymbol{S_0^\alpha} \qquad \text{(A.5)}
\end{aligned}
$$

Equating the above expression to the plastic stress power arising from physical arguments, i.e., $\dot{\omega}^p = \sum_{\alpha=1}^{n_s} \tau^\alpha \dot{\gamma}^\alpha$, the resolved shear stress takes the form

$$
\begin{aligned}
\dot{\omega}^p = \sum_{\alpha=1}^{n_s} \tau^\alpha \dot{\gamma}^\alpha &= \sum_{\alpha=1}^{n_s} \left(\left(\boldsymbol{F^{eT} F^e T}\right) : \boldsymbol{S_0^\alpha}\right) \dot{\gamma}^\alpha \ ; \ \forall \ \dot{\gamma}^\alpha \\
\implies \tau^\alpha &= \left(\boldsymbol{F^{eT} F^e T}\right) : \boldsymbol{S_0^\alpha} \qquad \text{(A.6)}
\end{aligned}
$$

APPENDIX B

Matrix Exponential Gâteaux Derivative

A more comprehensive review of tensorial derivatives of tensor-valued functions is presented in [192] while it's importance in the context of rate-independent and rate-dependent crystal plasticity constitutive models is covered in [193]. Let $\mathcal{M}_n$ denote the space of all $n \times n$ matrices, closed under addition, scalar multiplication and matrix multiplication. Further let $\exp : \mathcal{M}_n \to \mathcal{M}_n$ denote the matrix exponential, which maps any $n \times n$ matrix $\boldsymbol{M}$ to another $n \times n$ matrix $\boldsymbol{M}_e$ via the following series

$$\boldsymbol{M}_e = \exp(\boldsymbol{M}) = \boldsymbol{I} + \boldsymbol{M} + \frac{1}{2!}\boldsymbol{M}^2 + \ldots + \frac{1}{k!}\boldsymbol{M}^k + \ldots \tag{B.1}$$

It is already known that the matrix exponential is well-defined, i.e., the series in Eqn. (B.1) is convergent for any arbitrary choice of $\boldsymbol{M}$. We wish to compute the Gâteaux derivative or the directional derivative of this exponential map. In other words, the

following limit is of interest to us

$$\left.\frac{\partial(\exp \boldsymbol{M})}{\partial \boldsymbol{M}}\right|_{\boldsymbol{M}} : \boldsymbol{H} = \mathcal{D}\exp(\boldsymbol{M})_{\boldsymbol{H}} := \lim_{t\to 0} \frac{\exp(\boldsymbol{M} + t\boldsymbol{H}) - \exp(\boldsymbol{M})}{t} \tag{B.2}$$

where $\boldsymbol{H} \in \mathcal{M}_n$. Eqn. (B.2) is precisely the directional derivative of the exponential map evaluated at $\boldsymbol{M}$ along the direction $\boldsymbol{H}$. Then

$$\begin{aligned}
\mathcal{D}\exp(\mathrm{M})_{\boldsymbol{H}} &= \lim_{t\to 0} \frac{\exp(\boldsymbol{M} + t\boldsymbol{H}) - \exp(\boldsymbol{M})}{t} \\
&= \lim_{t\to 0} \frac{1}{t}\left(\sum_{k=0}^{\infty} \frac{1}{k!}(\boldsymbol{M} + t\boldsymbol{H})^k - \sum_{k=0}^{\infty} \frac{1}{k!}\boldsymbol{M}^k\right) \\
&= \lim_{t\to 0}\left[\boldsymbol{H} + \frac{1}{2!}(\boldsymbol{H}\boldsymbol{M} + \boldsymbol{M}\boldsymbol{H}) + \frac{1}{3!}\left(\boldsymbol{H}\boldsymbol{M}^2 + \boldsymbol{M}\boldsymbol{H}\boldsymbol{M} + \boldsymbol{M}^2\boldsymbol{H}\right) + \ldots\right] \\
&+ \underbrace{\lim_{t\to 0} \mathcal{O}(t)}_{0} \\
&= \sum_{k=0}^{\infty} \frac{1}{(k+1)!}\left(\sum_{l=0}^{k} \boldsymbol{M}^{k-l}\boldsymbol{H}\boldsymbol{M}^l\right)
\end{aligned} \tag{B.3}$$

The final expression in Eqn. (B.1) is the directional derivative of the matrix exponential evaluated at $\boldsymbol{M}$ along $\boldsymbol{H}$. Now construct a $2n \times 2n$ matrix $\boldsymbol{P}$ as follows :

$$\boldsymbol{P} = \begin{bmatrix} \boldsymbol{M} & \boldsymbol{H} \\ \boldsymbol{0} & \boldsymbol{M} \end{bmatrix} \tag{B.4}$$

Computing a few powers of $\boldsymbol{P}$ and representing it in the block matrix form

$$\boldsymbol{P}^1 = \begin{bmatrix} \boldsymbol{M} & \boldsymbol{H} \\ \mathbf{0} & \boldsymbol{M} \end{bmatrix} \ , \ \boldsymbol{P}^2 = \begin{bmatrix} \boldsymbol{M}^2 & \boldsymbol{M}\boldsymbol{H} + \boldsymbol{H}\boldsymbol{M} \\ \mathbf{0} & \boldsymbol{M}^2 \end{bmatrix}$$
$$\boldsymbol{P}^3 = \begin{bmatrix} \boldsymbol{M}^3 & \boldsymbol{M}^2\boldsymbol{H} + \boldsymbol{M}\boldsymbol{H}\boldsymbol{M} + \boldsymbol{H}\boldsymbol{M}^2 \\ \mathbf{0} & \boldsymbol{M}^3 \end{bmatrix} \ , \ \ldots$$

Paying attention to the $(1,2)$ block for each power of $\boldsymbol{P}$, we observe successive contributions to the sum in Eqn. (B.3) appearing exactly once. Then it is clear that

$$\mathcal{D}\exp(\mathrm{M})_{\boldsymbol{H}} = \left[\sum_{k=1}^{\infty} \frac{1}{k!}\boldsymbol{P}^k\right]_{(1,2)} = [\exp(\boldsymbol{P})]_{(1,2)} \tag{B.5}$$

Eqn. (B.5) implies that computing $\mathcal{D}\exp(\mathrm{M})_{\boldsymbol{H}}$ reduces to evaluating $\exp(\boldsymbol{P})$. This is has already been implemented in the function '**dexpm**' which forms a part of (**Manopt**), a MATLAB toolbox for optimization on manifolds ([194]). I present an alternative procedure without the need to compute the exponential of a $2n \times 2n$ matrix, and that is based on the following property.

Theorem : The directional derivative of the exponential map can be expressed as

$$\mathcal{D}\exp(\mathrm{M})_{\boldsymbol{H}} = \sum_{i=0}^{\infty} \frac{1}{i!}\boldsymbol{T}_i$$

where the sequence $\{\boldsymbol{T}_i\}$ possesses the following generating function

$$\boldsymbol{T}_i = \boldsymbol{M}.\boldsymbol{T}_{i-1} + \boldsymbol{T}_{i-1}.\boldsymbol{M} - \boldsymbol{M}.\boldsymbol{T}_{i-2}.\boldsymbol{M} \quad \forall i \in \{2,3,4,\ldots,\}\ ; \quad \boldsymbol{T}_1 = \boldsymbol{H},\ \boldsymbol{T}_0 = \boldsymbol{0} \tag{B.6}$$

Proof. From Eqn. (B.3) we have

$$\begin{aligned}
&\boldsymbol{T}_{i-1} = \sum_{l=0}^{i-1} \boldsymbol{M}^{i-1-l}\boldsymbol{H}\boldsymbol{M}^{l}\ ;\ \boldsymbol{T}_{i-2} = \sum_{l=0}^{i-2} \boldsymbol{M}^{i-2-l}\boldsymbol{H}\boldsymbol{M}^{l} \\
&\implies \boldsymbol{M}.\boldsymbol{T}_{i-1} + \boldsymbol{T}_{i-1}.\boldsymbol{M} - \boldsymbol{M}.\boldsymbol{T}_{i-2}.\boldsymbol{M} \\
&\quad = \sum_{l=0}^{i-1} \boldsymbol{M}^{i-l}\boldsymbol{H}\boldsymbol{M}^{l} + \sum_{l=0}^{i-1} \boldsymbol{M}^{i-1-l}\boldsymbol{H}\boldsymbol{M}^{l+1} - \sum_{l=0}^{i-2} \boldsymbol{M}^{i-1-l}\boldsymbol{H}\boldsymbol{M}^{l+1} \\
&\quad = \sum_{l=0}^{i-1} \boldsymbol{M}^{i-l}\boldsymbol{H}\boldsymbol{M}^{l} + \boldsymbol{H}\boldsymbol{M}^{i} + \cancel{\sum_{l=0}^{i-2} \boldsymbol{M}^{i-1-l}\boldsymbol{H}\boldsymbol{M}^{l+1}} - \cancel{\sum_{l=0}^{i-2} \boldsymbol{M}^{i-1-l}\boldsymbol{H}\boldsymbol{M}^{l+1}} \\
&\quad = \sum_{l=0}^{i} \boldsymbol{M}^{i-l}\boldsymbol{H}\boldsymbol{M}^{l} = \boldsymbol{T}_i
\end{aligned}$$

□

APPENDIX C

Cubic Line Search

The Newton-Raphson scheme offers quadratic convergence when the initial guess is sufficiently close to the actual solution to a root-finding problem. However, for stiff systems the simple Newton-Raphson iteration does not ensure convergence simply because of the sensitivity of the objective function to relatively small changes in the estimate of the minmizer. This is where line search plays a crucial role in improving the initial guess so as to eventually achieve quadratic convergence offered by the Newton-Raphson scheme. The line search and backtracking algorithm outlined below has been adopted from [195].

Let $\boldsymbol{f}(\boldsymbol{x})$ denote the function whose root, $\boldsymbol{x}_0$ we would like to compute. The root-finding problem can then be recast into an optimization problem where we wish to minimize the objective function $g(\boldsymbol{x}) \coloneqq \frac{1}{2}\boldsymbol{f}(\boldsymbol{x}) \cdot \boldsymbol{f}(\boldsymbol{x})$. Now let $\boldsymbol{x}_n$ denote an estimate of the root at the n^{th} iteration, so that the search direction, $\boldsymbol{p}$ corresponding to the

Newton-Raphson iteration is

$$\boldsymbol{p} = -\left(\nabla \boldsymbol{f}\right)^{-1} \cdot \boldsymbol{f}\left(\boldsymbol{x}_n\right)$$
$$\boldsymbol{x}_{n+1} = \boldsymbol{x}_n + \boldsymbol{p} \tag{C.1}$$

where ∇ denotes the square matrix of partial derivatives of $\boldsymbol{f}$ relative to $\boldsymbol{x}$. In the classical Newton-Raphson iteration, if the initial guess is sufficiently close to the actual solution, the update based on Eqn. C.1 suffices to furnish a root. While the search direction $\boldsymbol{p}$ represents a descent direction for $g(\boldsymbol{x})$, taking an entire step along that direction does not necessarily ensure a decrease in the objective function. Rather, a more reasonable update procedure is of the form $\boldsymbol{x}_{n+1} = \boldsymbol{x}_n + \kappa \boldsymbol{p}$; $\kappa \in (0, 1]$ where the value of κ is determined adaptively to ensure that the objective function continues to decrease sufficiently so that subsequent guesses get progressively better. We then require the average rate of decrease of g to be atleast some fraction α of the initial rate of decrease $\nabla g \cdot \boldsymbol{p}$,

$$g\left(\boldsymbol{x}_{n+1}\right) \leq g\left(\boldsymbol{x}_n\right) + \alpha \nabla g \cdot \left(\boldsymbol{x}_{n+1} - \boldsymbol{x}_n\right) \tag{C.2}$$

We set $\alpha = 10^{-4}$ for our purpose. Following this, a procedure is necessary to furnish an estimate of the root(the next guess) keeping in line with sufficient decrease. This is done through a backtracking routine. Define

$$h(\kappa) \equiv g\left(\boldsymbol{x}_n + \kappa \boldsymbol{p}\right) \tag{C.3}$$

so that

$$h'(\kappa) = \nabla g \cdot \boldsymbol{p} \tag{C.4}$$

We start with $h(0)$ and $h'(0)$ available. The first step is the Newton-Raphson step, i.e., $\kappa = 1$, which if it is not acceptable leaves us with $h(1)$ as well. Then modeling $h(\kappa)$ uniquely as a quadratic using the information $h(0)$, $h'(0)$ and $h(1)$ yields $g_2(\kappa)$,

$$g_2\kappa = [h(1) - h(0) - h'(0)]\,\kappa^2 + h'(0)\kappa + h(0) \tag{C.5}$$

for which we are interested in the value of κ minimizing $g_2\kappa$ which is

$$\kappa = -\frac{h'(0)}{2\,[h(1) - h(0) - h'(0)]} \tag{C.6}$$

To prevent κ values from being prohibitively small we set $\kappa_{\min} = 0.1$. For subsequent backtracks, prior information is used to model $h(\kappa)$ as a cubic uniquely,

$$g_3(\kappa) = a\kappa^3 + b\kappa^2 + h'(0)\kappa + h(0) \tag{C.7}$$

where the constants a and b are identified from the additional conditions that $g_3(\kappa_1)$ and $g_3(\kappa_2)$ give the correct values, which would have been previously evaluated. This is the case since κ_1 and κ_2 will have failed the sufficient decrease condition which would have led to further backtracking. Once a and b are computed, the minimum

of the cubic in Eqn. C.7 is attained at

$$\kappa = \frac{-b + \sqrt{b^2 - 3ah'(0)}}{3a} \tag{C.8}$$

additionally enforcing $0.1\kappa_1 \leq \kappa \leq 0.5\kappa_1$.

BIBLIOGRAPHY

BIBLIOGRAPHY

[1] LK Aagesen, JF Adams, JE Allison, WB Andrews, V Araullo-Peters, T Berman, Z Chen, S Daly, S Das, S DeWitt, et al. Prisms: An integrated, open-source framework for accelerating predictive structural materials science. *JOM*, 70(10):2298–2314, 2018.

[2] L Anand and M Kothari. A computational procedure for rate-independent crystal plasticity. *Journal of the Mechanics and Physics of Solids*, 44(4):525–558, 1996.

[3] MA Siddiq Qidwai, Alexis C Lewis, and Andrew B Geltmacher. Using image-based computational modeling to study microstructure–yield correlations in metals. *Acta Materialia*, 57(14):4233–4247, 2009.

[4] Christophe Geuzaine and Jean-François Remacle. Gmsh: A 3-d finite element mesh generator with built-in pre-and post-processing facilities. *International journal for numerical methods in engineering*, 79(11):1309–1331, 2009.

[5] Huihui Yu, Yunchang Xin, Maoyin Wang, and Qing Liu. Hall-petch relationship in mg alloys: A review. *Journal of Materials Science & Technology*, 34(2):248–256, 2018.

[6] Surya R Kalidindi, Curt A Bronkhorst, and Lallit Anand. Crystallographic texture evolution in bulk deformation processing of fcc metals. *Journal of the Mechanics and Physics of Solids*, 40(3):537–569, 1992.

[7] Robert Davis McGinty. *Multiscale representation of polycrystalline inelasticity*. Georgia institute of technology, 2001.

[8] John Allison, Dan Backman, and Leo Christodoulou. Integrated computational materials engineering: a new paradigm for the global materials profession. *Jom*, 58(11):25–27, 2006.

[9] Hiroshi Furuya, Nozomu Kogiso, Saburo Matunaga, and Kei Senda. Applications of magnesium alloys for aerospace structure systems. In *Materials science forum*, volume 350, pages 341–348. Trans Tech Publ, 2000.

[10] Mark Easton, Mark Gibson, Aiden Beer, Matthew Barnett, Chris Davies, Yvonne Durandet, Stuart Blacket, Xiaobo Chen, Nick Birbilis, and Trevor Abbott. The application of magnesium alloys to the lightweighting of automotive structures. In *Sustainable Automotive Technologies 2012*, pages 17–23. Springer, 2012.

[11] Usman Riaz, Ishraq Shabib, and Waseem Haider. The current trends of mg alloys in biomedical applications—a review. *Journal of Biomedical Materials Research Part B: Applied Biomaterials*, 107(6):1970–1996, 2019.

[12] Suveen N Mathaudhu and Eric A Nyberg. Magnesium alloys in us military applications: past, current and future solutions. In *Essential readings in magnesium technology*, pages 71–76. Springer, 2016.

[13] E Aghion and Boris Bronfin. Magnesium alloys development towards the 21st century. In *Materials Science Forum*, volume 350, pages 19–30. Trans Tech Publ, 2000.

[14] RJ Chester and IJ Polmear. The metallurgy of light alloys. *London: Institution of Metallurgists*, page 75, 1983.

[15] YN Wang and JC Huang. Texture analysis in hexagonal materials. *Materials Chemistry and Physics*, 81(1):11–26, 2003.

[16] Mohammadreza Yaghoobi, George Z Voyiadjis, and Veera Sundararaghavan. Crystal plasticity simulation of magnesium and its alloys: A review of recent advances. *Crystals*, 11(4):435, 2021.

[17] Nicole Stanford, Jie Geng, Young Bum Chun, Chris Huw John Davies, Jian Feng Nie, and Matthew Robert Barnett. Effect of plate-shaped particle distributions on the deformation behaviour of magnesium alloy az91 in tension and compression. *Acta materialia*, 60(1):218–228, 2012.

[18] Joseph D Robson, N Stanford, and Matthew Robert Barnett. Effect of precipitate shape on slip and twinning in magnesium alloys. *Acta materialia*, 59(5):1945–1956, 2011.

[19] Jian-Feng Nie. Precipitation and hardening in magnesium alloys. *Metallurgical and Materials Transactions A*, 43(11):3891–3939, 2012.

[20] Xiaolong Ma, Quan Jiao, Laszlo J Kecskes, Jaafar A El-Awady, and Timothy P Weihs. Effect of basal precipitates on extension twinning and pyramidal slip: A micro-mechanical and electron microscopy study of a mg–al binary alloy. *Acta Materialia*, 189:35–46, 2020.

[21] Alok Singh, M Nakamura, M Watanabe, A Kato, and AP Tsai. Quasicrystal strengthened mg–zn–y alloys by extrusion. *Scripta Materialia*, 49(5):417–422, 2003.

[22] BL Wu, YH Zhao, XH Du, YD Zhang, F Wagner, and C Esling. Ductility enhancement of extruded magnesium via yttrium addition. *Materials Science and Engineering: A*, 527(16-17):4334–4340, 2010.

[23] Stefanie Sandlöbes, Zongrui Pei, Martin Friák, L-F Zhu, Fuchi Wang, Stefan Zaefferer, Dierk Raabe, and Jörg Neugebauer. Ductility improvement of mg alloys by solid solution: Ab initio modeling, synthesis and mechanical properties. *Acta Materialia*, 70:92–104, 2014.

[24] Qingda Yang and AK Ghosh. Deformation behavior of ultrafine-grain (ufg) az31b mg alloy at room temperature. *Acta materialia*, 54(19):5159–5170, 2006.

[25] Bo Guan, Yunchang Xin, Xiaoxu Huang, Peidong Wu, and Qing Liu. Quantitative prediction of texture effect on hall–petch slope for magnesium alloys. *Acta Materialia*, 173:142–152, 2019.

[26] W Yuan, SK Panigrahi, J-Q Su, and RS Mishra. Influence of grain size and texture on hall–petch relationship for a magnesium alloy. *Scripta Materialia*, 65(11):994–997, 2011.

[27] Huihui Yu, Changzheng Li, Yunchang Xin, Adrien Chapuis, Xiaoxu Huang, and Qing Liu. The mechanism for the high dependence of the hall-petch slope for twinning/slip on texture in mg alloys. *Acta Materialia*, 128:313–326, 2017.

[28] EO Hall. The deformation and ageing of mild steel: Iii discussion of results. *Proceedings of the Physical Society. Section B*, 64(9):747, 1951.

[29] NJ Petch. The cleavage strength of polycrystals. *Journal of the Iron and Steel Institute*, 174:25–28, 1953.

[30] JD Eshelby, FC Frank, and FRN Nabarro. Xli. the equilibrium of linear arrays of dislocations. *The London, Edinburgh, and Dublin Philosophical Magazine and Journal of Science*, 42(327):351–364, 1951.

[31] RW Armstrong. The influence of polycrystal grain size on several mechanical properties of materials. *Metallurgical and Materials Transactions B*, 1(5):1169–1176, 1970.

[32] SM Razavi, DC Foley, I Karaman, KT Hartwig, O Duygulu, LJ Kecskes, SN Mathaudhu, and VH Hammond. Effect of grain size on prismatic slip in mg–3al–1zn alloy. *Scripta Materialia*, 67(5):439–442, 2012.

[33] YN Wang, CI Chang, CJ Lee, HK Lin, and JC Huang. Texture and weak grain size dependence in friction stir processed mg–al–zn alloy. *Scripta Materialia*, 55(7):637–640, 2006.

[34] Leon L Shaw, Angel L Ortiz, and Juan C Villegas. Hall–petch relationship in a nanotwinned nickel alloy. *Scripta Materialia*, 58(11):951–954, 2008.

[35] Lili Guo, Zhongchun Chen, and Li Gao. Effects of grain size, texture and twinning on mechanical properties and work-hardening behavior of az31 magnesium alloys. *Materials Science and Engineering: A*, 528(29-30):8537–8545, 2011.

[36] LB Tong, MY Zheng, S Kamado, DP Zhang, J Meng, LR Cheng, and HJ Zhang. Reducing the tension–compression yield asymmetry of extruded mg–zn–ca alloy via equal channel angular pressing. *Journal of Magnesium and Alloys*, 3(4):302–308, 2015.

[37] Yi Wang and Hahn Choo. Influence of texture on hall–petch relationships in an mg alloy. *Acta Materialia*, 81:83–97, 2014.

[38] Zachary C Cordero, Braden E Knight, and Christopher A Schuh. Six decades of the hall–petch effect–a survey of grain-size strengthening studies on pure metals. *International Materials Reviews*, 61(8):495–512, 2016.

[39] A Jain, O Duygulu, DW Brown, CN Tomé, and SR Agnew. Grain size effects on the tensile properties and deformation mechanisms of a magnesium alloy, az31b, sheet. *Materials Science and Engineering: A*, 486(1-2):545–555, 2008.

[40] JA Del Valle, Fernando Carreño, and Oscar Antonio Ruano. Influence of texture and grain size on work hardening and ductility in magnesium-based alloys processed by ecap and rolling. *Acta Materialia*, 54(16):4247–4259, 2006.

[41] Yasumasa Chino, Mamoru Mabuchi, Ryuji Kishihara, Hiroyuki Hosokawa, Yasuo Yamada, e Wen Cui, Koji Shimojima, and Hajime Iwasaki. Mechanical properties and press formability at room temperature of az31 mg alloy processed by single roller drive rolling. *Materials Transactions*, 43(10):2554–2560, 2002.

[42] MR Barnett, Zohreh Keshavarz, AG Beer, and Dale Atwell. Influence of grain size on the compressive deformation of wrought mg–3al–1zn. *Acta materialia*, 52(17):5093–5103, 2004.

[43] DKJH Kim, JH Kim, M-G Lee, YS Lee, and S-H Kang. Experimental investigation into effect of annealing treatment on springback of magnesium alloy sheets. *Materials Research Innovations*, 15(sup1):s183–s186, 2011.

[44] R Hill and KS Havner. Perspectives in the mechanics of elastoplastic crystals. *Journal of the Mechanics and Physics of Solids*, 30(1-2):5–22, 1982.

[45] D Peirce, RJ Asaro, and A Needleman. An analysis of nonuniform and localized deformation in ductile single crystals. *Acta metallurgica*, 30(6):1087–1119, 1982.

[46] Robert J Asaro and JR0375 Rice. Strain localization in ductile single crystals. *Journal of the Mechanics and Physics of Solids*, 25(5):309–338, 1977.

[47] R Hill and JR0254 Rice. Constitutive analysis of elastic-plastic crystals at arbitrary strain. *Journal of the Mechanics and Physics of Solids*, 20(6):401–413, 1972.

[48] Rodney Hill. Generalized constitutive relations for incremental deformation of metal crystals by multislip. *Journal of the Mechanics and Physics of Solids*, 14(2):95–102, 1966.

[49] Geoffrey Ingram Taylor. Plastic strain in metals. *J. Inst. Metals*, 62:307–324, 1938.

[50] X Wu, G Proust, M Knezevic, and SR Kalidindi. Elastic–plastic property closures for hexagonal close-packed polycrystalline metals using first-order bounding theories. *Acta Materialia*, 55(8):2729–2737, 2007.

[51] Tony Fast, Marko Knezevic, and Surya R Kalidindi. Application of microstructure sensitive design to structural components produced from hexagonal polycrystalline metals. *Computational Materials Science*, 43(2):374–383, 2008.

[52] Paul Van Houtte. Simulation of the rolling and shear texture of brass by the taylor theory adapted for mechanical twinning. *Acta Metallurgica*, 26(4):591–604, 1978.

[53] V Sundararaghavan and N Zabaras. On the synergy between texture classification and deformation process sequence selection for the control of texture-dependent properties. *Acta Materialia*, 53(4):1015 – 1027, 2005.

[54] Veera Sundararaghavan and Nicholas Zabaras. A multi-length scale sensitivity analysis for the control of texture-dependent properties in deformation processing. *International Journal of Plasticity*, 24(9):1581 – 1605, 2008.

[55] Julie Lévesque, Mohsen Mohammadi, Raja K Mishra, and Kaan Inal. An extended taylor model to simulate localized deformation phenomena in magnesium alloys. *International Journal of Plasticity*, 78:203–222, 2016.

[56] Ricardo A Lebensohn and CN Tomé. A self-consistent anisotropic approach for the simulation of plastic deformation and texture development of polycrystals: application to zirconium alloys. *Acta metallurgica et materialia*, 41(9):2611–2624, 1993.

[57] RA Lebensohn, CN Tomé, and P Ponte Castaneda. Self-consistent modelling of the mechanical behaviour of viscoplastic polycrystals incorporating intragranular field fluctuations. *Philosophical Magazine*, 87(28):4287–4322, 2007.

[58] Miroslav Zecevic, Ricardo A Lebensohn, Michael Rogers, Jacob Moore, Vincent Chiravalle, Evan Lieberman, Daniel Dunning, Galen Shipman, Marko Knezevic, and Nathaniel Morgan. Viscoplastic self-consistent formulation as generalized material model for solid mechanics applications. *Applications in Engineering Science*, 6:100040, 2021.

[59] AJ Beaudoin Jr, H Mecking, and UF Kocks. Development of localized orientation gradients in fcc polycrystals. *Philosophical Magazine A*, 73(6):1503–1517, 1996.

[60] R Becker and S Panchanadeeswaran. Effects of grain interactions on deformation and local texture in polycrystals. *Acta metallurgica et materialia*, 43(7):2701–2719, 1995.

[61] Curt A Bronkhorst, SR Kalidindi, and Lallit Anand. Polycrystalline plasticity and the evolution of crystallographic texture in fcc metals. *Philosophical Transactions of the Royal Society of London. Series A: Physical and Engineering Sciences*, 341(1662):443–477, 1992.

[62] DP Mika and PR Dawson. Polycrystal plasticity modeling of intracrystalline boundary textures. *Acta Materialia*, 47(4):1355–1369, 1999.

[63] Veera Sundararaghavan and Nicholas Zabaras. Design of microstructure-sensitive properties in elasto-viscoplastic polycrystals using multi-scale homogenization. *International Journal of Plasticity*, 22(10):1799–1824, 2006.

[64] Karel Matouš and Antoinette M Maniatty. Finite element formulation for modelling large deformations in elasto-viscoplastic polycrystals. *International Journal for Numerical Methods in Engineering*, 60(14):2313–2333, 2004.

[65] Gorti B Sarma, Balasubramaniam Radhakrishnan, and Paul R Dawson. Mesoscale modeling of microstructure and texture evolution during deformation processing of metals. *Advanced Engineering Materials*, 4(7):509–514, 2002.

[66] Anand Krishna Kanjarla, Paul Van Houtte, and Laurent Delannay. Assessment of plastic heterogeneity in grain interaction models using crystal plasticity finite element method. *International Journal of Plasticity*, 26(8):1220–1233, 2010.

[67] Surya R Kalidindi. Incorporation of deformation twinning in crystal plasticity models. *Journal of the Mechanics and Physics of Solids*, 46(2):267–290, 1998.

[68] A Staroselsky and L Anand. Inelastic deformation of polycrystalline face centered cubic materials by slip and twinning. *Journal of the Mechanics and Physics of Solids*, 46(4):671–696, 1998.

[69] A Staroselsky and L Anand. A constitutive model for hcp materials deforming by slip and twinning: application to magnesium alloy az31b. *International journal of Plasticity*, 19(10):1843–1864, 2003.

[70] Hamidreza Abdolvand, Mark R Daymond, and Charles Mareau. Incorporation of twinning into a crystal plasticity finite element model: Evolution of lattice strains and texture in zircaloy-2. *International Journal of Plasticity*, 27(11):1721–1738, 2011.

[71] Ana Fernández, María Teresa Pérez Prado, Yujie Wei, and Antoine Jérusalem. Continuum modeling of the response of a mg alloy az31 rolled sheet during uniaxial deformation. *International Journal of Plasticity*, 27(11):1739–1757, 2011.

[72] Jing Zhang and Shailendra P Joshi. Phenomenological crystal plasticity modeling and detailed micromechanical investigations of pure magnesium. *Journal of the Mechanics and Physics of Solids*, 60(5):945–972, 2012.

[73] Yao Liu and Yujie Wei. A polycrystal based numerical investigation on the temperature dependence of slip resistance and texture evolution in magnesium alloy az31b. *International Journal of Plasticity*, 55:80–93, 2014.

[74] Ricardo A Lebensohn, Anand K Kanjarla, and Philip Eisenlohr. An elasto-viscoplastic formulation based on fast fourier transforms for the prediction of micromechanical fields in polycrystalline materials. *International Journal of Plasticity*, 32:59–69, 2012.

[75] Philip Eisenlohr, Martin Diehl, Ricardo A Lebensohn, and Franz Roters. A spectral method solution to crystal elasto-viscoplasticity at finite strains. *International Journal of Plasticity*, 46:37–53, 2013.

[76] Reeju Pokharel, Jonathan Lind, Anand K Kanjarla, Ricardo A Lebensohn, Shiu Fai Li, Peter Kenesei, Robert M Suter, and Anthony D Rollett. Polycrystal plasticity: comparison between grain-scale observations of deformation and simulations. *Annu. Rev. Condens. Matter Phys.*, 5(1):317–346, 2014.

[77] Aaditya Lakshmanan, Jiangyi Luo, Iman Javaheri, and Veera Sundararaghavan. Three-dimensional crystal plasticity simulations using peridynamics theory and experimental comparison. *International Journal of Plasticity*, 142:102991, 2021.

[78] Jiangyi Luo. *Peridynamic Modeling of Crystal Plasticity with an Adaptive Dynamic Relaxation Solver*. PhD thesis, University of Michigan, Ann Arbor, 2019.

[79] S. Sun and V. Sundararaghavan. A peridynamic implementation of crystal plasticity. *International Journal of Solids and Structures*, 51(19):3350 – 3360, 2014.

[80] CN Tomé, Ricardo A Lebensohn, and UF Kocks. A model for texture development dominated by deformation twinning: application to zirconium alloys. *Acta metallurgica et materialia*, 39(11):2667–2680, 1991.

[81] IJ Beyerlein and CN Tomé. A probabilistic twin nucleation model for hcp polycrystalline metals. *Proceedings of the Royal Society A: Mathematical, Physical and Engineering Sciences*, 466(2121):2517–2544, 2010.

[82] Chuanlai Liu, Pratheek Shanthraj, Martin Diehl, Franz Roters, S Dong, Jie Dong, Wenjiang Ding, and Dierk Raabe. An integrated crystal plasticity–phase field model for spatially resolved twin nucleation, propagation, and growth in hexagonal materials. *International Journal of Plasticity*, 106:203–227, 2018.

[83] Stephen R Niezgoda, Anand K Kanjarla, Irene J Beyerlein, and Carlos N Tomé. Stochastic modeling of twin nucleation in polycrystals: an application in hexagonal close-packed metals. *International journal of plasticity*, 56:119–138, 2014.

[84] Chaitanya Paramatmuni and Anand K Kanjarla. A crystal plasticity fft based study of deformation twinning, anisotropy and micromechanics in hcp materials: Application to az31 alloy. *International Journal of Plasticity*, 113:269–290, 2019.

[85] Chaitanya Paramatmuni and Fionn PE Dunne. Effect of twin crystallographic orientation on deformation and growth in mg alloy az31. *International Journal of Plasticity*, 135:102775, 2020.

[86] Chaitanya Paramatmuni, Zebang Zheng, W Mark Rainforth, and Fionn PE Dunne. Twin nucleation and variant selection in mg alloys: An integrated crystal plasticity modelling and experimental approach. *International Journal of Plasticity*, 135:102778, 2020.

[87] Chaitanya Paramatmuni, Yi Guo, Philip J Withers, and Fionn PE Dunne. A three-dimensional mechanistic study of the drivers of classical twin nucleation and variant selection in mg alloys: a mesoscale modelling and experimental study. *International Journal of Plasticity*, page 103027, 2021.

[88] M Arul Kumar, AK Kanjarla, SR Niezgoda, RA Lebensohn, and CN Tomé. Numerical study of the stress state of a deformation twin in magnesium. *Acta Materialia*, 84:349–358, 2015.

[89] Anand K Kanjarla, Irene J Beyerlein, Ricardo A Lebensohn, and Carlos Tomé. On the role of local grain interactions on twin nucleation and texture evolution in hexagonal materials. In *Materials Science Forum*, volume 702, pages 265–268. Trans Tech Publ, 2012.

[90] R Kondo, Y Tadano, and Kazuyuki Shizawa. A phase-field model of twinning and detwinning coupled with dislocation-based crystal plasticity for hcp metals. *Computational materials science*, 95:672–683, 2014.

[91] G Proust, CN Tomé, and GC Kaschner. Modeling texture, twinning and hardening evolution during deformation of hexagonal materials. *Acta Materialia*, 55(6):2137–2148, 2007.

[92] C Guillemer, Michel Clavel, and Georges Cailletaud. Cyclic behavior of extruded magnesium: Experimental, microstructural and numerical approach. *International Journal of Plasticity*, 27(12):2068–2084, 2011.

[93] H Wang, PD Wu, CN Tomé, and J Wang. A constitutive model of twinning and detwinning for hexagonal close packed polycrystals. *Materials Science and Engineering: A*, 555:93–98, 2012.

[94] Mohammadreza Yaghoobi, John E Allison, and Veera Sundararaghavan. Multiscale modeling of twinning and detwinning behavior of hcp polycrystals. *International Journal of Plasticity*, 127:102653, 2020.

[95] Mohammadreza Yaghoobi, Krzysztof S Stopka, Aaditya Lakshmanan, Veera Sundararaghavan, John E Allison, and David L McDowell. Prisms-fatigue computational framework for fatigue analysis in polycrystalline metals and alloys. *npj Computational Materials*, 7(1):1–12, 2021.

[96] Mohammadreza Yaghoobi, Zhe Chen, Veera Sundararaghavan, Samantha Daly, and John E Allison. Crystal plasticity finite element modeling of extension twinning in we43 mg alloys: Calibration and validation. *Integrating Materials and Manufacturing Innovation*, 10(3):488–507, 2021.

[97] Amit Acharya, JL Bassani, and A Beaudoin. Geometrically necessary dislocations, hardening, and a simple gradient theory of crystal plasticity. *Scripta Materialia*, 48(2):167–172, 2003.

[98] H Gao, Y Huang, WD Nix, and JW1688037 Hutchinson. Mechanism-based strain gradient plasticity—i. theory. *Journal of the Mechanics and Physics of Solids*, 47(6):1239–1263, 1999.

[99] Peter Gudmundson. A unified treatment of strain gradient plasticity. *Journal of the Mechanics and Physics of Solids*, 52(6):1379–1406, 2004.

[100] NA Fleck, GM Muller, Mike F Ashby, and John W Hutchinson. Strain gradient plasticity: theory and experiment. *Acta Metallurgica et materialia*, 42(2):475–487, 1994.

[101] Sangmin Lee and Veera Sundararaghavan. Calibration of nanocrystal grain boundary model based on polycrystal plasticity using molecular dynamics simulations. *International Journal for Multiscale Computational Engineering*, 8(5):509–522, 2010.

[102] Shardul Panwar and Veera Sundararaghavan. Dislocation theory-based cohesive model for microstructurally short fatigue crack growth. *Materials Science and Engineering: A*, 708:395–404, 2017.

[103] S Panwar, JF Adams, JE Allison, JW Jones, and V Sundararaghavan. A grain boundary interaction model for microstructurally short fatigue cracks. *International Journal of Fatigue*, 113:401–406, 2018.

[104] A Jain and SR Agnew. Modeling the temperature dependent effect of twinning on the behavior of magnesium alloy az31b sheet. *Materials Science and Engineering: A*, 462(1-2):29–36, 2007.

[105] Babak Raeisinia, Sean R Agnew, and Ainul Akhtar. Incorporation of solid solution alloying effects into polycrystal modeling of mg alloys. *Metallurgical and Materials Transactions A*, 42(5):1418–1430, 2011.

[106] M Arul Kumar, Irene Jane Beyerlein, and Carlos N Tome. Grain size constraints on twin expansion in hexagonal close packed crystals. *Journal of Applied Physics*, 120(15):155105, 2016.

[107] M Arul Kumar and Irene J Beyerlein. Influence of plastic properties on the grain size effect on twinning in ti and mg. *Materials Science and Engineering: A*, 771:138644, 2020.

[108] IJ Beyerlein, RJ McCabe, and CN Tomé. Effect of microstructure on the nucleation of deformation twins in polycrystalline high-purity magnesium: A multi-scale modeling study. *Journal of the Mechanics and Physics of Solids*, 59(5):988–1003, 2011.

[109] Babak Ravaji and Shailendra P Joshi. A crystal plasticity investigation of grain size-texture interaction in magnesium alloys. *Acta Materialia*, 208:116743, 2021.

[110] Y Guo, J Schwiedrzik, J Michler, and X Maeder. On the nucleation and growth of {112 2} twin in commercial purity titanium: In situ investigation of the local stress field and dislocation density distribution. *Acta Materialia*, 120:292–301, 2016.

[111] MH Yoo. Slip, twinning, and fracture in hexagonal close-packed metals. *Metallurgical transactions A*, 12(3):409–418, 1981.

[112] Lisa Sugiura. Comparison of degradation caused by dislocation motion in compound semiconductor light-emitting devices. *Applied physics letters*, 70(10):1317–1319, 1997.

[113] Angus J Wilkinson, David J Dingley, and Graham Meaden. Strain mapping using electron backscatter diffraction. In *Electron Backscatter Diffraction in Materials Science*, pages 231–249. Springer, 2009.

[114] KZ Troost, P Van der Sluis, and DJ Gravesteijn. Microscale elastic-strain determination by backscatter kikuchi diffraction in the scanning electron microscope. *Applied Physics Letters*, 62(10):1110–1112, 1993.

[115] Angus J Wilkinson. Measurement of elastic strains and small lattice rotations using electron back scatter diffraction. *Ultramicroscopy*, 62(4):237–247, 1996.

[116] Angus J Wilkinson, Graham Meaden, and David J Dingley. High resolution mapping of strains and rotations using electron backscatter diffraction. *Materials Science and Technology*, 22(11):1271–1278, 2006.

[117] Angus J Wilkinson, Graham Meaden, and David J Dingley. High-resolution elastic strain measurement from electron backscatter diffraction patterns: new levels of sensitivity. *Ultramicroscopy*, 106(4-5):307–313, 2006.

[118] LK Aagesen, JF Adams, JE Allison, WB Andrews, V Araullo-Peters, T Berman, Z Chen, S Daly, S Das, S DeWitt, et al. Prisms: An integrated, open-source framework for accelerating predictive structural materials science. *JOM*, 70(10):2298–2314, 2018.

[119] Mohammadreza Yaghoobi, Sriram Ganesan, Srihari Sundar, Aaditya Lakshmanan, Shiva Rudraraju, John E Allison, and Veera Sundararaghavan. Prismsplasticity: An open-source crystal plasticity finite element software. *Computational Materials Science*, 169:109078, 2019.

[120] Ekkehart Kröner. Allgemeine kontinuumstheorie der versetzungen und eigenspannungen. *Archive for Rational Mechanics and Analysis*, 4(1):273–334, 1959.

[121] Erastus H Lee. Elastic-plastic deformation at finite strains. *Journal of Applied Mechanics*, 1969.

[122] Robert J Asaro and Alan Needleman. Overview no. 42 texture development and strain hardening in rate dependent polycrystals. *Acta metallurgica*, 33(6):923–953, 1985.

[123] N Ohno and J-D Wang. Kinematic hardening rules with critical state of dynamic recovery, part i: formulation and basic features for ratchetting behavior. *International journal of plasticity*, 9(3):375–390, 1993.

[124] DL McDowell. Stress state dependence of cyclic ratchetting behavior of two rail steels. *International Journal of Plasticity*, 11(4):397–421, 1995.

[125] John Wyrill Christian and Subhash Mahajan. Deformation twinning. *Progress in materials science*, 39(1-2):1–157, 1995.

[126] Michael A Groeber and Michael A Jackson. Dream. 3d: a digital representation environment for the analysis of microstructure in 3d. *Integrating materials and manufacturing innovation*, 3(1):56–72, 2014.

[127] Romain Quey, PR Dawson, and Fabrice Barbe. Large-scale 3d random polycrystals for the finite element method: Generation, meshing and remeshing. *Computer Methods in Applied Mechanics and Engineering*, 200(17-20):1729–1745, 2011.

[128] F Bachmann, Ralf Hielscher, and Helmut Schaeben. Texture analysis with mtex–free and open source software toolbox. In *Solid State Phenomena*, volume 160, pages 63–68. Trans Tech Publ, 2010.

[129] Florian Bachmann, Ralf Hielscher, and Helmut Schaeben. Grain detection from 2d and 3d ebsd data—specification of the mtex algorithm. *Ultramicroscopy*, 111(12):1720–1733, 2011.

[130] Brian Puchala, Glenn Tarcea, Emmanuelle A Marquis, Margaret Hedstrom, HV Jagadish, and John E Allison. The materials commons: a collaboration platform and information repository for the global materials community. *Jom*, 68(8):2035–2044, 2016.

[131] Sriram Ganesan. *Microstructural response of magnesium alloys: 3D crystal plasticity and experimental validation*. PhD thesis, University of Michigan, Ann Arbor, 2017.

[132] Mohsen Taheri Andani, Aaditya Lakshmanan, Veera Sundararaghavan, John Allison, and Amit Misra. Quantitative study of the effect of grain boundary parameters on the slip system level hall-petch slope for basal slip system in mg-4al. *Acta Materialia*, 200:148–161, 2020.

[133] Mohsen Taheri Andani, Aaditya Lakshmanan, Mohammadreza Karamooz-Ravari, Veera Sundararaghavan, John Allison, and Amit Misra. A quantitative study of stress fields ahead of a slip band blocked by a grain boundary in unalloyed magnesium. *Scientific reports*, 10(1):1–8, 2020.

[134] John Price Hirth, Jens Lothe, and T Mura. Theory of dislocations. *Journal of Applied Mechanics*, 50(2):476, 1983.

[135] GJ Weng. A micromechanical theory of grain-size dependence in metal plasticity. *Journal of the Mechanics and Physics of Solids*, 31(3):193–203, 1983.

[136] RW Armstrong, I Codd, RM Douthwaite, and NJ Petch. The plastic deformation of polycrystalline aggregates. *The Philosophical Magazine: A Journal of Theoretical Experimental and Applied Physics*, 7(73):45–58, 1962.

[137] A Akhtar and EJPM Teghtsoonian. Substitutional solution hardening of magnesium single crystals. *Philosophical Magazine*, 25(4):897–916, 1972.

[138] E Bayerschen, AT McBride, BD Reddy, and T Böhlke. Review on slip transmission criteria in experiments and crystal plasticity models. *Journal of materials science*, 51(5):2243–2258, 2016.

[139] Z Shen, RH Wagoner, and WAT Clark. Dislocation pile-up and grain boundary interactions in 304 stainless steel. *Scripta metallurgica*, 20(6):921–926, 1986.

[140] Z Shen, RH Wagoner, and WAT Clark. Dislocation and grain boundary interactions in metals. *Acta metallurgica*, 36(12):3231–3242, 1988.

[141] TC Lee, IM Robertson, and HK Birnbaum. Tem in situ deformation study of the interaction of lattice dislocations with grain boundaries in metals. *Philosophical Magazine A*, 62(1):131–153, 1990.

[142] H Lim, MG Lee, JH Kim, BL Adams, and RH Wagoner. Simulation of polycrystal deformation with grain and grain boundary effects. *International Journal of Plasticity*, 27(9):1328–1354, 2011.

[143] Jörg Luster and MA Morris. Compatibility of deformation in two-phase ti-al alloys: Dependence on microstructure and orientation relationships. *Metallurgical and Materials Transactions A*, 26(7):1745–1756, 1995.

[144] Mohsen Taheri Andani, Aaditya Lakshmanan, Veera Sundararaghavan, John Allison, and Amit Misra. Estimation of micro-hall-petch coefficients for prismatic slip system in mg-4al as a function of grain boundary parameters. *Acta Materialia*, page 117613, 2021.

[145] Bruce Alexander Bilby, Alan Howard Cottrell, and KH Swinden. The spread of plastic yield from a notch. *Proceedings of the Royal Society of London. Series A. Mathematical and Physical Sciences*, 272(1350):304–314, 1963.

[146] Shuji Taira, Keisuke Tanaka, and Yoshikazu Nakai. A model of crack-tip slip band blocked by grain boundary. *Mechanics Research Communications*, 5(6):375–381, 1978.

[147] Sham-Tsong Shiue and Sanboh Lee. The effect of grain size on fracture: Dislocation-free zone in the front of the finite crack tip. *Journal of applied physics*, 70(6):2947–2953, 1991.

[148] Nikoloz Ivanovich Muskhelishvili and Jens Rainer Maria Radok. *Singular integral equations: boundary problems of function theory and their application to mathematical physics*. Courier Corporation, 2008.

[149] Chaoyue Zhao, Xianhua Chen, Jingfeng Wang, Teng Tu, Yan Dai, Kwang Seon Shin, and Fusheng Pan. Strain hardening behavior in mg–al alloys at room temperature. *Advanced Engineering Materials*, 21(3):1801062, 2019.

[150] TR Long and Charles S Smith. Single-crystal elastic constants of magnesium and magnesium alloys. *Acta Metallurgica*, 5(4):200–207, 1957.

[151] Leon J Slutsky and CW Garland. Elastic constants of magnesium from 4.2 k to 300 k. *Physical Review*, 107(4):972, 1957.

[152] E Nieto-Valeiras, S Haouala, and J LLorca. On the effect of slip transfer at grain boundaries on the strength of fcc polycrystals. *European Journal of Mechanics-A/Solids*, 91:104427, 2022.

[153] Erich Scheil and Almuth Lange-Weise. *Statistische Gefügeuntersuchungen*. Verlag Stahleisen, 1935.

[154] HA Schwartz. The metallographic determination of the size distribution of temper carbon nodules. *Metals Alloys*, 5:139, 1934.

[155] SA Saltykov. Calculation of the distribution curves for the size of dispersed grains. *Plant Laboratory*, 15(11):1317–1319, 1949.

[156] Iman Javaheri and Veera Sundararaghavan. Polycrystalline microstructure reconstruction using markov random fields and histogram matching. *Computer-Aided Design*, 120:102806, 2020.

[157] Marco A Lopez-Sanchez. Grainsizetools: a python script for grain size analysis and paleopiezometry based on grain size. *Journal of Open Source Software*, 3(30):863, 2018.

[158] Shang Sun and Veera Sundararaghavan. A probabilistic crystal plasticity model for modeling grain shape effects based on slip geometry. *Acta Materialia*, 60(13-14):5233–5244, 2012.

[159] Siddhartha Srivastava and Veeraraghavan Sundararaghavan. An integer programming approach for mesh generation for polycrystals using the ebsd map. In *AIAA Scitech 2019 Forum*, page 0966, 2019.

[160] Siddhartha Srivastava and Veera Sundararaghavan. Graph coloring approach to mesh generation in multiphase media with smooth boundaries. *AIAA Journal*, 58(1):198–205, 2020.

[161] Gregory S Rohrer, David M Saylor, Bassem El-Dasher, Brent L Adams, Anthony D Rollett, and Paul Wynblatt. The distribution of internal interfaces in polycrystals. *Z. Metallkd*, 95(4):197–214, 2004.

[162] Gregory S Rohrer. The distribution of grain boundary planes in polycrystals. *Jom*, 59(9):38–42, 2007.

[163] EJ Lieberman, AD Rollett, RA Lebensohn, and EM Kober. Calculation of grain boundary normals directly from 3d microstructure images. *Modelling and Simulation in Materials Science and Engineering*, 23(3):035005, 2015.

[164] A Seeger. Mechanical twinning of crystals by mv klassen-neklyudova. *Acta Crystallographica*, 20(2):323–323, 1966.

[165] Bruce Alexander Bilby and AG Crocker. The theory of the crystallography of deformation twinning. *Proceedings of the Royal Society of London. Series A. Mathematical and physical sciences*, 288(1413):240–255, 1965.

[166] Arnol'd Markovich Kosevich and VS Boĭko. Dislocation theory of the elastic twinning of crystals. *Soviet Physics Uspekhi*, 14(3):286, 1971.

[167] SV Kamat, JP Hirth, and P Müllner. The effect of stress on the shape of a blocked deformation twin. *Philosophical Magazine A*, 73(3):669–680, 1996.

[168] TE Mitchell and JP Hirth. The shape, configuration and stress field of twins and martensite plates. *Acta metallurgica et materialia*, 39(7):1711–1717, 1991.

[169] JT Lloyd. A dislocation-based model for twin growth within and across grains. *Proceedings of the Royal Society A: Mathematical, Physical and Engineering Sciences*, 474(2210):20170709, 2018.

[170] Josh Kacher, Julian E Sabisch, and Andrew M Minor. Statistical analysis of twin/grain boundary interactions in pure rhenium. *Acta Materialia*, 173:44–51, 2019.

[171] M Arul Kumar, Irene Jane Beyerlein, Rodney James McCabe, and Carlos N Tome. Grain neighbour effects on twin transmission in hexagonal close-packed materials. *Nature communications*, 7(1):1–9, 2016.

[172] M Arul Kumar, IJ Beyerlein, RA Lebensohn, and CN Tomé. Modeling the effect of neighboring grains on twin growth in hcp polycrystals. *Modelling and Simulation in Materials Science and Engineering*, 25(6):064007, 2017.

[173] Paolo Cermelli and Morton E Gurtin. On the characterization of geometrically necessary dislocations in finite plasticity. *Journal of the Mechanics and Physics of Solids*, 49(7):1539–1568, 2001.

[174] A Arsenlis and DM Parks. Crystallographic aspects of geometrically-necessary and statistically-stored dislocation density. *Acta materialia*, 47(5):1597–1611, 1999.

[175] N Bertin, CN Tomé, IJ Beyerlein, MR Barnett, and L Capolungo. On the strength of dislocation interactions and their effect on latent hardening in pure magnesium. *International Journal of Plasticity*, 62:72–92, 2014.

[176] P Franciosi and A Zaoui. Multislip in fcc crystals a theoretical approach compared with experimental data. *Acta Metallurgica*, 30(8):1627–1637, 1982.

[177] CJ Bayley, WAM Brekelmans, and MGD Geers. A comparison of dislocation induced back stress formulations in strain gradient crystal plasticity. *International Journal of Solids and Structures*, 43(24):7268–7286, 2006.

[178] Sriram Ganesan, Mohammadreza Yaghoobi, Alan Githens, Zhe Chen, Samantha Daly, John E Allison, and Veera Sundararaghavan. The effects of heat treatment on the response of we43 mg alloy: crystal plasticity finite element simulation and sem-dic experiment. *International Journal of Plasticity*, 137:102917, 2021.

[179] A Githens, S Ganesan, Z Chen, J Allison, V Sundararaghavan, and S Daly. Characterizing microscale deformation mechanisms and macroscopic tensile properties of a high strength magnesium rare-earth alloy: A combined experimental and crystal plasticity approach. *Acta Materialia*, 186:77–94, 2020.

[180] D Greeley, M Yaghoobi, D Pagan, V Sundararaghavan, and J Allison. Using synchrotron radiation to improve understanding of deformation of polycrystalline metals by measuring, modelling and publishing 4d information. *IOP Conference Series: Materials Science and Engineering*, 580(1):012017, 2019.

[181] Sriram Ganesan, Iman Javaheri, and Veera Sundararaghavan. Constrained voronoi models for interpreting surface microstructural measurements. *Mechanics of Materials*, 159:103892, 2021.

[182] Veera Sundararaghavan. Reconstruction of three-dimensional anisotropic microstructures from two-dimensional micrographs imaged on orthogonal planes. *Integrating Materials and Manufacturing Innovation*, 3(1):19, Jun 2014.

[183] A Kumar, L Nguyen, M DeGraef, and V Sundararaghavan. A markov random field approach for microstructure synthesis. *Modelling and Simulation in Materials Science and Engineering*, 24(3):035015, 2016.

[184] Pinar Acar and Veera Sundararaghavan. A markov random field approach for modeling spatio-temporal evolution of microstructures. *Modelling and Simulation in Materials Science and Engineering*, 24(7):075005, 2016.

[185] Anthony Wayne Thompson and WA Backofen. The effect of grain size on fatigue. *Acta metallurgica*, 19(7):597–606, 1971.

[186] Christian Heinrich and Veera Sundararaghavan. A method to predict fatigue crack initiation in metals using dislocation dynamics. *Corrosion Reviews*, 35(4-5):325–341, 2017.

[187] Aaditya Lakshmanan, Mohammadreza Yaghoobi, Krzysztof S Stopka, and Veera Sundararaghavan. Crystal plasticity finite element modeling of grain size and morphology effects on yield strength and extreme value fatigue response. *Submitted*, 2021.

[188] Ruoqian Liu, Abhishek Kumar, Zhengzhang Chen, Ankit Agrawal, Veera Sundararaghavan, and Alok Choudhary. A predictive machine learning approach for microstructure optimization and materials design. *Scientific reports*, 5(11551):1 – 12, 2015.

[189] Pinar Acar and Veera Sundararaghavan. Utilization of a linear solver for multiscale design and optimization of microstructures. *AIAA Journal*, 54(5):1751 – 1759, 2016.

[190] Pinar Acar, Siddhartha Srivastava, and Veera Sundararaghavan. Stochastic design optimization of microstructures with utilization of a linear solver. *AIAA Journal*, 55(9):3161–3168, 2017.

[191] Lallit Anand. Constitutive equations for hot-working of metals. *International Journal of Plasticity*, 1(3):213–231, 1985.

[192] M Itskov. The derivative with respect to a tensor: some theoretical aspects and applications. *ZAMM-Journal of Applied Mathematics and Mechanics/Zeitschrift für Angewandte Mathematik und Mechanik: Applied Mathematics and Mechanics*, 82(8):535–544, 2002.

[193] EA de Souza Neto. The exact derivative of the exponential of an unsymmetric tensor. *Computer Methods in Applied Mechanics and Engineering*, 190(18-19):2377–2383, 2001.

[194] Nicolas Boumal, Bamdev Mishra, P.-A. Absil, and Rodolphe Sepulchre. Manopt, a matlab toolbox for optimization on manifolds. *Journal of Machine Learning Research*, 15:1455–1459, 2014.

[195] William H Press, Saul A Teukolsky, William T Vetterling, and Brian P Flannery. Numerical recipes in c, 1988.